

TEL-AVIV UNIVERSITY
THE IBY AND ALDAR FLEISCHMAN FACULTY OF ENGINEERING

MULTI-BEAM CYCLOTRON-RESONANCE MASER ARRAY

By

Li Lei

THESIS SUBMITTED FOR THE DEGREE OF “DOCTOR OF PHILOSOPHY”
SUBMITTED TO THE SENATE OF TEL-AVIV UNIVERSITY

February 2002

TEL-AVIV UNIVERSITY
THE IBY AND ALDAR FLEISCHMAN FACULTY OF ENGINEERING

MULTI-BEAM CYCLOTRON-RESONANCE MASER ARRAY

By

Li Lei

THESIS SUBMITTED FOR THE DEGREE OF “DOCTOR OF PHILOSOPHY”
SUBMITTED TO THE SENATE OF TEL-AVIV UNIVERSITY

This Research Work was Carried Out at Tel-Aviv University
in The Faculty Of Engineering

Under The Supervision of Prof. Eli Jerby

February 2002

*This thesis is dedicated to my parents,
Lei Mao-Fan and Yin Shou-Lan*

ACKNOWLEDGMENTS

I would like to express my sincere gratitude to my advisor Prof. Eli Jerby for his help, guidance, encouragement and support, sharing with me his insights, knowledge and experience throughout this work.

Particular thanks to Dr. A. Fisher and Dr. D. Hinshelwood from the Naval Research Laboratory for their help on the cathodes issue.

A helpful and pleasant association with Mr. M. Korol, Mr. A. Shahadi, Mr. A. Kesar, Mr. M. Bensal and Mr. Y. Reshef at Tel-Aviv University over the years is also gratefully acknowledged.

Contents

Abstract-----	VII
List of Abbreviations-----	IX
Chapter 1. Introduction	1
1.1. Cyclotron Resonance Masers-----	1
1.2. The Concept of the Multi-beam CRM-array-----	12
1.3. Electron Emitters-----	18
1.4. Thesis Outline-----	24
Chapter 2. 2D CRM-Array Experiment	25
2.1. Experimental Design and Setup-----	25
2.1.1. Electron Beams-----	29
2.1.2. Magnetic Fields-----	32
2.1.3. Pulsed Power Devices-----	34
2.1.4. The Periodic Waveguide-----	36
2.1.5. Vacuum System Considerations-----	40
2.1.6. RF Diagnostics-----	40
2.2. Experimental Operation-----	42
2.3. Experimental Results-----	44
2.4. Analysis and Discussions-----	55
2.5. Conclusions-----	58
Chapter 3. The Carbon-Fiber CRM-Array Experiment	59
3.1. Experimental Design and Setup-----	59
3.1.1. Mechanical Design-----	61
3.1.2. Multi-beam Carbon-Fiber Cathode Arrays-----	64
3.1.2.1. Experimental Configuration-----	64
3.1.2.2. Cathode Fabrications-----	66
3.1.2.3. Electron Trajectories-----	67

3.1.2.4. Power Supplies -----	69
3.1.2.5. Electrical Performance-----	72
3.1.3. Magnetic Fields-----	79
3.1.4. The Periodic Waveguide-----	81
3.2. Experimental Operation-----	84
3.3. Experimental Results-----	85
3.4. Discussions-----	92
Chapter 4. Conclusions	94
4.1. Experimental Results-----	94
4.2. Suggestions for Future Work-----	95
Appendix A. Computer Programs and Simulations Documentation	96
A1. The EGUN Code Simulation for the 2D CRM-Array Experiment-----	96
A2. The Magnetic Fields Calculation for the 2D CRM-Array Experiment---	99
A3. The EGUN Code Simulation for the Carbon-Fiber CRM-array Experiment-----	101
A4. The Magnetic Field Calculation for the Carbon-Fiber CRM-array Experiment-----	105
Appendix B. Circuits of the Pulsed Power Devices	108
B1. Circuit of the Gun-Solenoid Pulsers-----	108
B2. Circuit of the Kicker Pulsers-----	109
B3. Circuit of the Multi-Channel Gun Pulsers-----	110
Appendix C. The Modified Marx Generator	111
C1. Model 615 MR Pulsers-----	111
C2. The Modified Model 615 Pulsers-----	112
References	113

Abstract

The cyclotron-resonance-maser array (CRM-array) proposed by Eli Jerby is a novel device in which separate electron beams perform, simultaneously, a cyclotron interaction with a single Bloch wave in an artificial lattice. It consists of CRM elements coupled together under a common magnetic field. The CRM-array has the capability to generate high-power microwave with relatively low-voltage electron beams. The low-voltage operation reduces the system overhead and leads to a relatively compact device. The CRM-array may radiate directly to free-space as an *active* phased-array antenna. Furthermore, the phase of each element output, and therefore the antenna far-field radiation pattern, can be varied by the electron-beam voltages.

This thesis presents experimental studies of the multi-beam CRM-arrays. In the present study, our effort focuses mainly on the establishment of the experimental fundamental frame of the multi-beam CRM-arrays. In addition, a secondary objective of the research was to explore a multi-beam CRM device with cold cathode arrays and to develop an efficient, reliable and cost-effective multi-beam electron source for vacuum electronic devices. This thesis describes the first successful operation of a two-beam CRM-array experiment. The experimental results verify the feasibility of the CRM-array concept and promote the efforts toward the realization of large CRM-arrays.

A 2D CRM array was operated with one and two electron beams (~ 10 keV / 0.1 A each). Microwave output signals are observed in frequencies around 7 GHz in an axial magnetic field of ~ 3 kG. Spectral measurements of the CRM outputs reveal frequency sweeps along the CRM pulses. These are associated with electron energy variations, in accordance with the theoretical CRM tuning condition. The synchronism of the cyclotron-resonance interaction with a backward spatial harmonic is confirmed.

This thesis presents also a first demonstration of a multi-beam CRM scheme with cold-cathode arrays. Based on commercial carbon fibers, a multi-beam cold-cathode array

demonstrates $\sim 400 \mu\text{s}$ pulses of $\sim 0.1 \text{ A}$ in each channel with two accelerating stages. By using this gun, the device operates at low voltages $\sim 5 \text{ kV}$ with $\sim 0.4 \text{ ms}$ pulse duration. Clear bursts of RF oscillations were observed around 5 GHz in the experiment. The CRM tuning results indicate clearly interactions with backward waves. The experimental results show that it is possible to use cold-cathode arrays instead of thermionic-cathode arrays in future multi-beam CRM devices.

List of abbreviations

2D	-	Two Dimensions
3D	-	Three Dimensions
B.P.F	-	Bandpass Filter
BWO	-	Backward Wave Oscillator
CARM	-	Cyclotron Auto-Resonance Maser
CsI	-	Cesium Iodide
CRM	-	Cyclotron Resonance Maser
EEE	-	Explosive Electron Emission
FEL	-	Free Electron Laser
Eq.	-	Equation
H.P.F	-	High Pass Filter
HPM	-	High Power Microwave
IF	-	Intermediate Frequencies
LO	-	Local Frequencies
MBK	-	Multiple-Beam Klystron
OBK	-	One-Beam Klystron
PC	-	Personal Computer
PWC	-	Periodic Waveguide Cyclotron Resonance Maser
RF	-	Radio Frequencies
SCR	-	Silicon Controlled Rectifier
SF6	-	Sulfur Hexafluoride
TWT	-	Travelling Wave Tube

Chapter 1

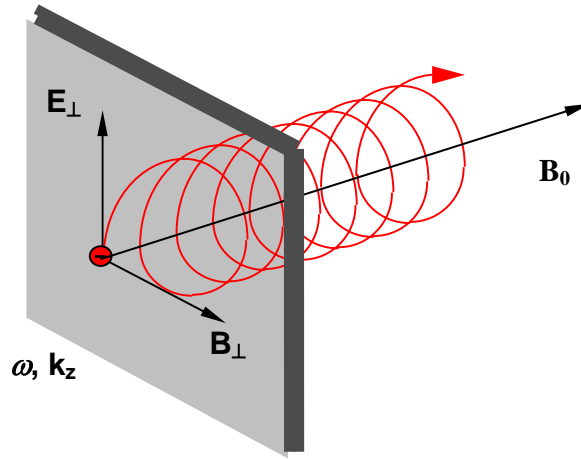
Introduction

Driving by the emerged new technologies and the potential applications, the innovative high-power microwaves sources have been developed rapidly in recent years. This chapter describes the motivation for the present work on multi-beam cyclotron resonance maser arrays, and provides a brief review of relative fields. An outline of the thesis is presented in Section 1.4.

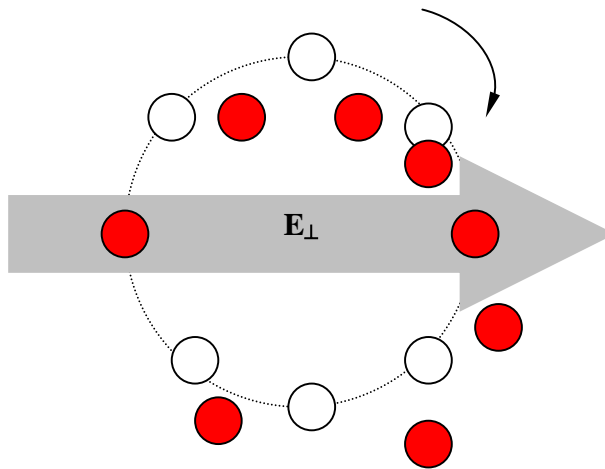
1.1. Cyclotron Resonance Masers

The cyclotron resonance masers (CRMs) [1] are the high power microwave sources, which are based on the induced cyclotron instability of a transiting electron beam. A simplified CRM scheme is shown in Fig. 1.1a. The electron beam is guided by a uniform axial magnetic field B_0 . Initially, the electrons undergo a cyclotron motion, and they are uniformly arranged in rotational phase on a circle (see Fig. 1.1b). Their Larmor radius is $r_{0L}=v_{0\perp}/\omega_c$, where $v_{0\perp}$ is the electron initial perpendicular velocity, and $\omega_c = eB_0/\gamma_0 m_0$ is the cyclotron frequency. Here $\gamma_0=(1-v_0^2/c^2)^{-1/2}$ is the relativistic factor and m_0 is the rest mass of the electron. After the interaction with the electromagnetic (em) field, some of the electrons are decelerated in the electric field, rotate faster, and hence accumulate phase lead while others are accelerated, rotate slower and accumulate phase lag. Then, a phase bunching occurs and the electrons radiate coherently. As the electrons gain or lose energy from the transverse electric field, the change in the relativistic factor γ_0 produces a corresponding change in the cyclotron frequency. Simultaneously, another phase bunching process occurs due to the Weibel mechanism that is the result of the axial Lorentz force. The two processes are always operating against each other. The cyclotron resonance satisfies the condition:

$$\omega = n\omega_c + k_z v_z \quad (1.1)$$



(a)



(b)

Fig. 1.1. The CRM interaction, (a) a schematic diagram, and (b) the process of the phase bunching (the white dots represent the electrons' position at the time, t , and the red dots represent the electrons' position at the time, $t+\Delta t$).

where ω and k_z are the *em* wave frequency and its wavenumber, respectively, ω_c and v_z are the electron cyclotron frequency and axial velocity, respectively, and n is the cyclotron harmonic order.

In fast-wave devices, the phase velocity is higher than the speed of light in vacuum, $v_{ph} > c$, and the basic mechanism of radiation is the electron bunching under the influence of the transverse electric field component. The dominant effect in the fast-wave devices is the relativistic azimuthal bunching caused by the $v_{\perp} \cdot E_{\perp}$ product, where v_{\perp} is the electron transverse velocity, E_{\perp} is the transverse electric component. In the slow-wave devices, the phase velocity is slower than the speed of light in vacuum, $v_{ph} < c$. A basic mechanism of radiation is the Weibel instability, in which the dominant effect is axial bunching caused by the axial $v_{\perp} \times B_{\perp}$ Lorentz force, where B_{\perp} is the transverse magnetic component [2].

The early work on CRMs date from the late 1950s. In 1958, the Australian physicist Twiss [3] first proposed a radiation mechanism involving electron gyrating in an external magnetic field. Then in 1959, Schneider [4] and Gaponov [5] each calculated the stimulated emission of relativistic monoenergetic electrons in a uniform magnetic field using quantum mechanical and classical approaches, respectively. In Schneider's approach, the free electron in the magnetic field can be indicated as a harmonic oscillator with quantized energy levels

$$w_n = mc^2 \left[1 + 2 \left(n + \frac{1}{2} \right) h \omega_c / mc^2 \right]^{1/2} - mc^2 + p^2 / 2m \quad (1.2)$$

neglecting spin, where ω_c is the rest electron gyrofrequency, p is the unquantized momentum along the magnetic field, and h is the Planck constant. Between states $n+1$ and n , transitions will occur at frequency $\omega_n = (1 - nh\omega_c / mc^2) \omega_c$ for $nh\omega_c \ll mc^2$ [6]. In Gaponov's approach, the coherent radiation is considered by the phases bunching mechanism. The mechanism was experimentally verified in the mid-60's, both in US [1] and USSR [7]. These works have generated considerable experimental and theoretical progress over the past four decades.

CRMs have been developed and studied mainly in single electron-beam schemes [8]. Fast-wave devices such as gyrotrons, cyclotron autoresonance masers (CARMs), and slow-wave devices such as dielectric-loaded CRMs have been studied intensively. Dispersion diagrams for gyrotrons, CARMs and dielectric-loaded CRMs are illustrated in Fig. 1.2. The uncoupled waveguide mode in Fig. 1.2a, b is represented by

$$\omega^2 = \omega_{c0}^2 + k_z^2 c^2 \quad (1.3)$$

where ω_{c0} is the cutoff frequency of the operating mode. The cyclotron wave in the electron beam obeys Eq.1.1.

Both gyrotrons and CARMs operate through a fast cyclotron wave interaction. For gyrotrons, the interaction takes place near the electron cyclotron frequency ω_c (Fig. 1.2a) where the CARMs interaction takes places with a phase velocity closed to the speed of light, as shown in Fig. 1.2b. In Fig. 1.2c, the dispersion function of the uncoupled waveguide mode is determined by the geometry of the waveguide, its dielectric properties, the frequency ω , and the wavenumber k . The Weibel interaction takes place slightly below the speed of light line and the synchronism occurs over a wide bandwidth.

Various CRMs are based on the normal Doppler effect. The resonance occurs when the operating frequency ω is larger than the Doppler term $k_z v_z$, which means that the phase velocity, $v_{ph} = \omega/k_z$, is larger than the electron axial velocity v_z . This corresponds to positive cyclotron harmonics ($n > 0$, see Eq. 1.1). The radiating electrons lose both orbital and axial momentum components. The anomalous Doppler effect occurs when the operating frequency ω is smaller than the Doppler term $k_z v_z$, i.e. $v_{ph} < v_z$, and consequently the CRM interaction is possible only with a negative cyclotron harmonic, $n \leq -1$. The radiating electrons lose their axial momentum and gain the orbital momentum [9–13].

Gyrotrons are the most popular CRM devices. They produce electromagnetic radiation in millimeter and submillimeter wavelengths. A typical configuration of the gyrotron is shown in Fig. 1.3.

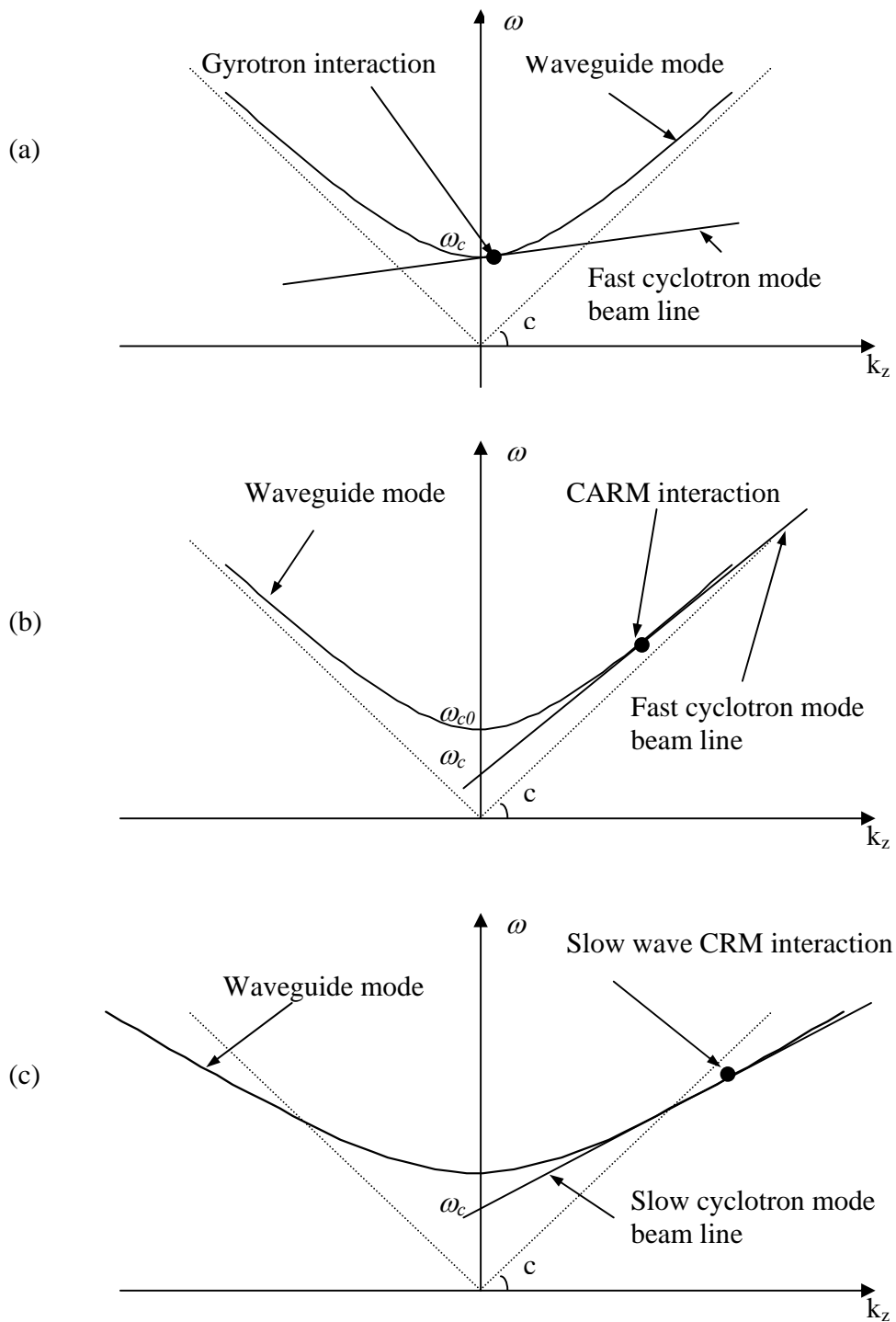


Fig. 1.2. Dispersion diagrams for (a) gyrotrons, (b) CARMs, and (c) slow-wave CRMs.

A gyrotron system usually consists of several distinct elements: a magnetron injection gun, an interaction region, a collector region and a strong externally applied magnetic field [14]. The electron beam is emitted from the electron gun, propagates along the interaction region, interacts with the *em* wave, and is deposited finally in the collector.

In the gyrotron device, the transverse velocity of electrons in a helical beam via relativistic instability generates the high power RF. The change of the electron cyclotron frequency due to the relativistic electron mass variation causes phase bunching in the electron beam and, consequently, electromagnetic cyclotron instabilities [15].

Scientists at Gorky State University (former USSR) developed the gyrotron concept into a practical radiation source during the 60's and 70's. In 1975, they developed a 22 kW CW oscillator that produced 2mm radiation with 22% efficiency [15]. In the 70's there were also major advances in the United States at the Naval Research Laboratory (NRL) as well as at MIT, Yale University, Varian and Hughes.

Gyro-devices, like linear-beam devices, have many variants. A full description of these devices is outside the scope of this work, but a list of the major types and schematic drawings of most important conventional linear-beam devices and their equivalent gyro-devices are presented in Table 1.1. For more detail see, for example Ref. [16].

Existing or potential applications of gyro-devices include plasma heating and current drive for nuclear fusions, RF acceleration in high-energy linear colliders, enhanced radar systems, and processing of material [17]. In past several decades, common experimental features of gyro-devices are focused on high average-power gyrotrons and high peak-power pulsed gyrotrons.

High average-power sources of 100-500 GHz radiations are necessary for electron cyclotron heating of fusion plasmas. The configurations of electron cyclotron masers with open quasi-optical resonators, such as the quasi-optical gyrotrons, show considerable promise for operation in this wavelength regime with high power RF.

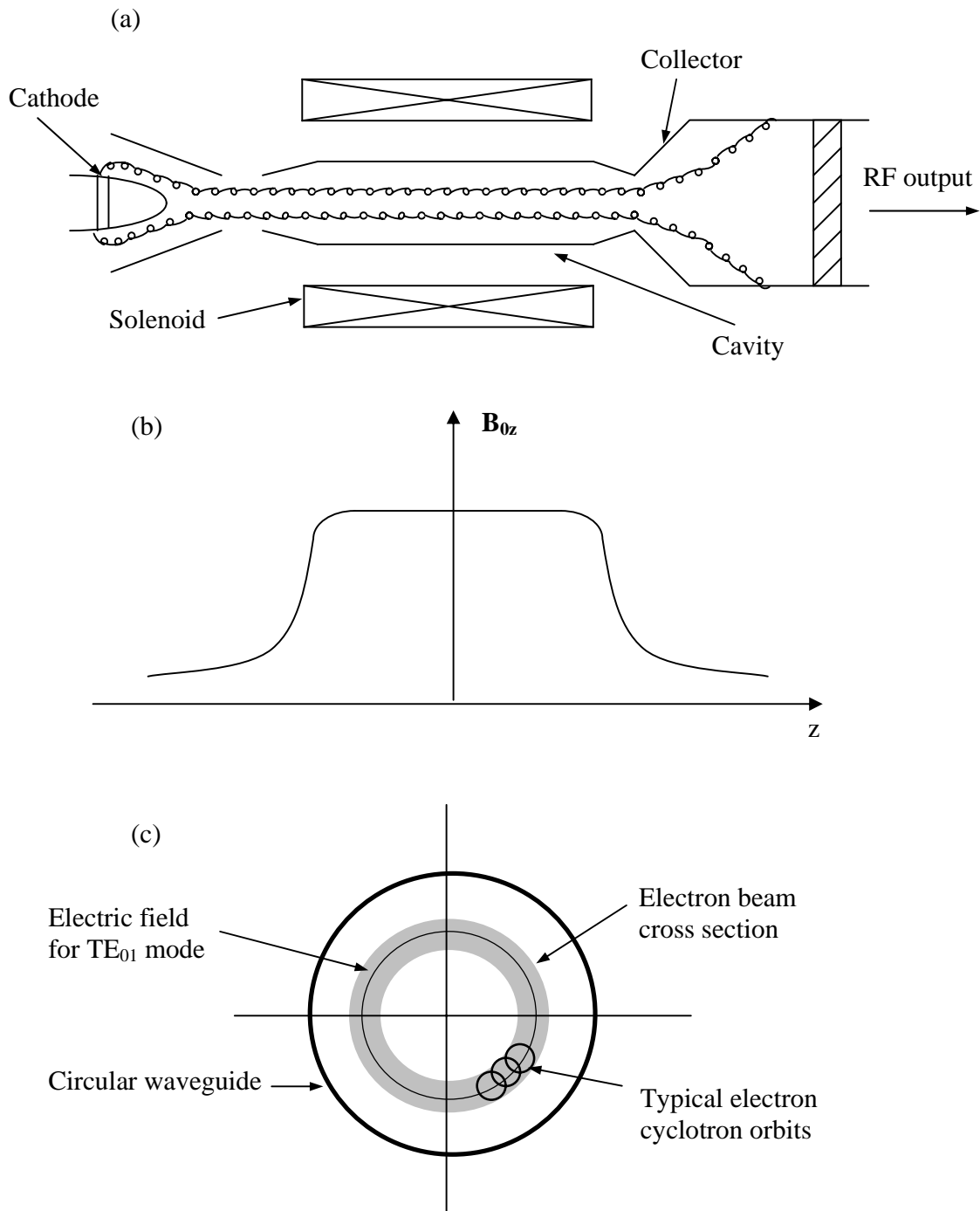


Fig. 1.3. Schematic diagrams of a gyrotron (a), the magnetic field profile (b) and the beam-cavity cross section in the interaction region for a circular TE_{01} operating mode (c) [Ref. 14].

In these configurations, the resonator mirrors are far from the beam-wave interaction region, which will allow a large volume for the interaction and low-ohmic heating densities on the mirrors. In addition, there is an effective control of transverse modes in the resonator, and separated electron-beam collection and RF output simplifies the development of depressed collectors. Table 1.2 presents a summary of the recent status of high frequency gyrotron oscillators for electron cyclotron resonance heating and current drive in nuclear fusion [18].

Using a pulse-line accelerator, an early 1 GW super-radiant oscillator experiment was reported by Granatstein *et al.* at 8 GHz [19]. Since the late 1970's, a number of significant experimental results were reported for relativistic gyrotrons in USSR. These experiments have yielded tens of megawatts peak power at centimeter and millimeter wavelengths regime. Recently, the whispering-gallery gyrotrons have produced several hundred megawatts peak power of microwaves near 35 GHz in the Naval Research Laboratory (NRL) [20].

According to theoretical studies, gyrotrons may also have a high efficiency at high harmonics of the gyrofrequency. Thus interaction at high cyclotron harmonics becomes especially advantageous when large magnetic fields should be avoided [21]. At Fukui University, Japan and University of Sydney, Australia, the gyrotron have been operated successfully in single mode at the second and third harmonic of the electron cyclotron frequency [22-28]. The medium power and submillimeter gyrotron has achieved frequency tunability in a wide range, from 38 GHz to 850 GHz.

Since the CARM was first suggested by Petelin [29] in 1974, several CARM experiments have been conducted at the Institute of Applied Physics in USSR [30-33], and at MIT [34, 35]. Recently, a CARM experiment with 26% high-efficiency at 7.9 mm wavelength was reported by Bratman *et al.* [36, 37]. Unlike the gyrotron, the CARM uses a large Doppler up-shift of the cyclotron frequency in order to reach high output frequencies [38, 39], and operates with $v_{ph} \sim c$.

Table 1.1. Schematics of linear beam devices and corresponding gyro-devices [15].

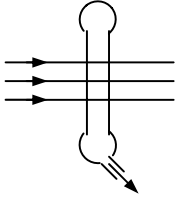
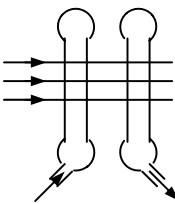
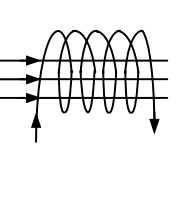
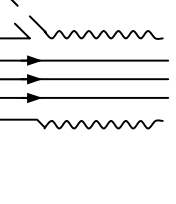
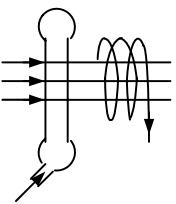
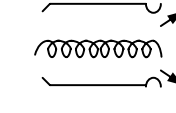
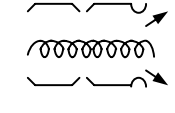
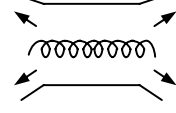
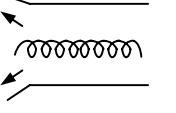
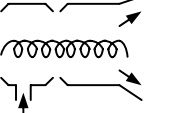
Linear beam devices					
	Monotron	Klystron	TWT	BWO	Twystron
Gyro-devices					
	Gyro-Monotron	Gyro-Klystron	Gyro-TWT	Gyro-BWO	Gyro-Twystron

Table 1.2. Present development status of high frequency gyrotron oscillators [18].

Institution/State	Frequency (GHz)	Power (MW)	Period (s)	Efficiency (%)
CPI/US	110	0.68/0.53/0.35	0.5/2/10	31/30/27
JAERI+Toshiba/Japan	110	0.35	5	30
GYCOM/Russia	110	0.70/0.32	2/5	37/30
Euratom Team/Europe	118	0.5/0.45	1/5	28/25
GYCOM/Russia	140	1/0.65	1/2	>40
GYCOM/Russia	140	0.8	1	50
GYCOM/Russia	160	0.5	0.7	30
JAERI+Toshiba/Japan	170	0.52/0.23	0.6/2.2	32

The CARM interaction is based on the same instability mechanism as that of the gyrotron, but it is operated much above cutoff frequency. The large Doppler frequency upshift permits a considerably reduced magnetic field B_0 . Therefore the CARM can provide millimeter and submillimeter radiation in the first electron-cyclotron harmonic using currently available magnet technology. In contrast to the gyrotron, which requires an electron beam with a large momentum pitch angle (typically $\alpha=v_{\perp}/v_z>1$), the CARM has an electron beam with low to moderate pitch angle ($\alpha<0.7$). The efficiency of CARMs is extremely sensitive to spread in the axial velocity of the beam.

Slow-wave CRMs have been studied in various schemes [40-45]. The dominant bunching effect in the slow-wave CRM stems from the Weibel mechanism. In contrast to the cyclotron maser instability, this instability is nonrelativistic in nature. The typical advantages of the slow-wave CRM are a wider frequency bandwidth and lower operating electron-beam energy. However, the slow-wave CRM is more sensitive than the conventional CRM to the electron-beam energy spread.

The periodic-waveguide cyclotron resonance maser (PWC) [46-49] is a device in which the electrons undergo a cyclotron interaction with traveling wave in a periodic waveguide. Periodicity in the waveguide structure may act as an artificial dielectric loading for the CRM interaction. It combines the properties of the fast-wave and the slow-wave CRM interactions. The experiments and theory on the PWC interaction show that it may be an attractive way to create high-power tunable compact sources of microwave radiation.

A comprehensive review on gyrotrons and CRMs state-of-art experiments is presented in [50]. A summary is given by a family tree shown in Fig. 1.4.

Several theoretical models have been introduced to describe the CRM dynamics. A single-particle theory applicable to the gyrotron configuration was given by Gaponov *et al.* in 1967 [7]. Later, Ott and Manheimer applied kinetic theory to investigate the instabilities of an intense relativistic electron beam [51]. The linear theory provides a

unified description of CRM dynamics. This theory was further extended to the nonlinear range by Sprangle and co-workers [52, 53]. In 1980, Chu *et al.* applied kinetic theory to TE modes in cylindrical waveguides [54]. This method was extended later by Lau [55] and Fliflet [56] to TE and TM waveguide modes. The present status of the theory of cyclotron masers with relativistic electron beams is reviewed in [57].

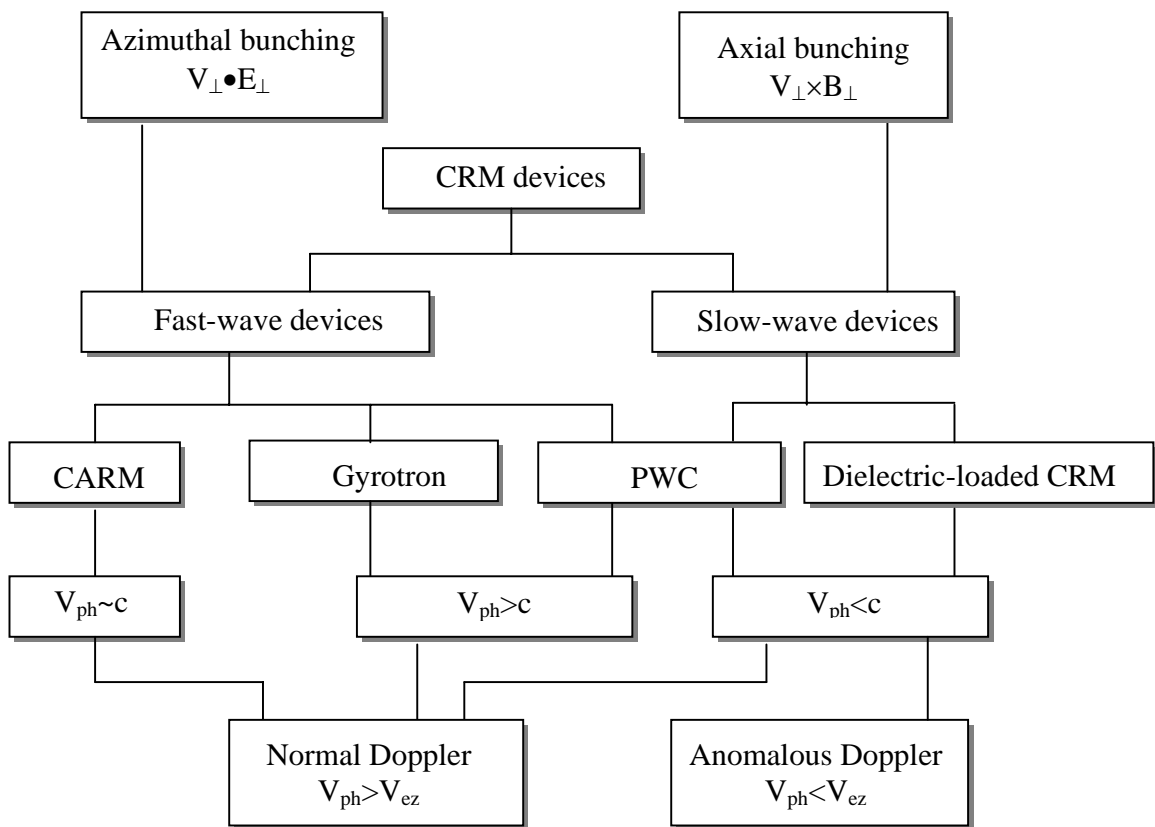


Fig. 1.4. CRM effects and devices.

1.2. The Concept of the Multi-beam CRM-array

CRM devices have a number of potential scientific, industrial and military applications. In particular, they are expected to be widely used as major sources of HPMS in future applications, such as material processing, nuclear reactors, radars, accelerators, and others. CRM's and gyrotrons have been developed so far as *single* electron-beam tubes. In order to obtain high output power, the sole electron-beam should possess sufficiently large kinetic energy and current. Consequently, a major part of the *overhead* in a typical CRM system is devoted to peripheral accessories needed to maintain the powerful electron-beam itself, both in acceleration and collector sections. In fact, most of the total length of a typical gyro-device is devoted to the consequent overhead (including the high-voltage electron gun and electron-optics, the tube shielding, a long collector, and the output window). Those contribute to weight and high cost. Therefore, the search for novel high-power microwave sources, which have low costs and compact sizes, is an attractive topic in this field.

The concept of multi-beam CRM-arrays was proposed by Jerby *et al.* [58-60] as a compact version of the single-beam CRM schemes. The idea is based on employing the transverse dimension to reduce the requirements of high voltage supplies and cooling systems. In the CRM-array, separate electron beams perform, simultaneously, a cyclotron interaction with a single Bloch wave in an artificial lattice. The CRM-array has the capability to generate high-power microwaves with relatively low operating voltages.

A theoretical analysis of the CRM-array [61, 62] predicts a considerable gain in a single mode. In this physical model, Maxwell's equations and Vlasov equation are used to analyze the mechanism of the multi-beam CRM in the linear region. The multi-beam CRM-array gain-dispersion relation in Laplace s plane is given by the following matrix equation [61]

$$\tilde{A} \begin{pmatrix} \hat{\ } \\ s \end{pmatrix} = \left[s \begin{pmatrix} \hat{\ } \\ s \underline{\underline{U}} - \underline{\underline{\Theta}}_k \end{pmatrix}^2 - \frac{1}{2} \underline{\underline{Q}}_k \begin{pmatrix} \hat{\ } \\ s \end{pmatrix} \underline{\underline{C}}_k \begin{pmatrix} \hat{\ } \\ s \end{pmatrix} \underline{\underline{\Theta}}_{pk}^2 \right]^{-1} \begin{pmatrix} \hat{\ } \\ s \underline{\underline{U}} - \underline{\underline{\Theta}}_k \end{pmatrix}^2 A_0 \quad (1.4)$$

where the subscript k denotes the harmonic order, $\hat{s} = jsL$ (L is the interaction length) is the normalized Laplace wavenumber, and $\underline{\underline{U}}$ is a unit matrix, respectively. The space-charge matrix $\hat{\underline{\underline{\Theta}}}_{pk}$ represents the effect of the electron current density on the CRM coupling. The power-flow-matrix $\underline{\underline{C}}_k(\hat{s})$ describes the distribution of the *em* wave power among the different modes and their spatial harmonics. The diagonal tuning matrix is $\hat{\underline{\underline{\Theta}}}_k = \left| \hat{\underline{\underline{\Theta}}}_{nk} \right|$, where $\hat{\underline{\underline{\Theta}}}_{nk} = \left(\omega - \omega_c - \beta_{nk} \bar{V}_{0z} \right) \frac{L}{\bar{V}_{0z}}$. The subscript n denotes the mode order. $\underline{\underline{Q}}_k(\hat{s})$ is the diagonal coupling matrix and is defined as

$$\underline{\underline{Q}}_k(\hat{s}) = \bar{\beta}_{ez} \left(\hat{s} \underline{\underline{U}} - \hat{\underline{\underline{\Theta}}}_k \right) \left(\hat{\underline{\underline{Z}}}_k - \bar{\beta}_{ez} \underline{\underline{U}} \right) + \frac{1}{2} \bar{\beta}_{e\perp}^2 \left(\hat{k}_0 \hat{\underline{\underline{Z}}}_k - \hat{s} \underline{\underline{U}} - \hat{\underline{\underline{\beta}}}_k \right) \quad (1.5)$$

where $\hat{k}_0 = kL$ is the normalized wavenumber, $\hat{\underline{\underline{\beta}}}_k$ and $\hat{\underline{\underline{Z}}}_k$ are diagonal matrices of the harmonic wavenumber and impedance, respectively, and $\bar{\beta}_{ez}$ and $\bar{\beta}_{e\perp}$ are the electron average normalized axial and perpendicular velocity components, respectively.

This linear analysis shows the possible mode selectivity and spectral purity of the 2D CRM-array. These stem from the spatial filtering in the periodic structure. In addition, the CRM-array may have unique features of an *active* phased array antenna [63]. The immediate integration proposed, of a microwave generator combined with an antenna, may simplify the overall radiative system in many applications.

Other types of microwave generators with more than one electron-beam have been proposed and studied by other workers [64-76]. These include the multiple-beam klystron (MBK), the multi-beam stagger-tuned gyrokystron, and the double-stream cyclotron maser. Most of them are in the stage of theoretical study except MBK. Several experimental schemes are under construction.

The concept of the MBK appeared in France in the 40's [64], and this kind of MBKs has really exploited in USSR. In recent years, MBKs are under consideration in other countries such as US and China. They have shown that the use of multiple-beam designs provides a powerful means for improving the parameters of microwave tubes. The MBKs provide low operating voltages, high power, low noise, and the possibility of wider operating bandwidth by the increase in total perveance. Many models of MBKs are produced in Russia and most of them for radar and communication applications. However, only a small number of them are widely known and few details were appeared in open publications [65]. According to Russian's work, as the beam number grows, the decreases of the characteristic impedance of the resonator are slower than the increases of the overall conductance of the multiple-beam due to the smaller contribution of the side capacitance. Therefore, for a MBK and an OBK (one beam klystron), in the case of equality of beam powers, beam perveances, and normalized radii of the channels, the MBK bandwidth is 2-2.5 times more than that of the OBK [66]. Two 6 cavity, 36 beams MBKs produce a total RF output peak power of 500-1000 kW with 60A beam current and a 28-34 kV beam voltage at the State Research and Production Corporation "ISTOK" in Russia [67]. The MBKs at 0.425, 0.85, 1.3, and 2.8GHz are also under development at Thomson Tubes Electroniques [68, 69]. The 1.3 GHz prototype operates with seven 133 A beams and a 115 kV beam voltage. It produces a total RF output peak power of 10 MW with 65% efficiency. Meanwhile, researchers in the Institute of Electronics, Chinese Academy of Sciences (IECAS) focus on S-band and C-band MBKs [70]. In US, under the MURI program, several progresses are carried out at Stanford Linear Accelerator Center and University of California, Davis. In a W-band micro-fabricated modular klystrons scheme, the semiconductor's deep-etch lithography technique is used. A klystron array is fabricated on single substrate. Several such modules can be stacked together to form a klystron "brick" and operated in parallel in order to produce high power RF by relatively low voltage. The "brick" can be driven by a single output, or by individual, spatially combined radiators [71].

Replacing the solid electron beams by hollow electron beams, a multi-beam gyroklystron was proposed by Nusinovich *et al.* A theoretical model of multi-beam

stagger-tuned gyroklystrons was developed. Two-stage, two-, three- and four-beam gyroklystrons operating in a small-signal regime were considered in detail. The analysis shows that when a number of beamlets is greater than or equal to four, it is preferable to stagger tune eigenfrequencies of individual input cavities around the eigenfrequency of the common output cavity. The simulation results demonstrate that the gain-bandwidth product in multi-beam gyroklystrons can be increased due to the stagger tuning much more strongly than in their single-beam counterparts [72].

The double-stream cyclotron maser was proposed by Bekefi at MIT [73]. In this scheme, two well-intermingled electron beams of different axial velocities are spun up and allowed to gyrate in a uniform axial magnetic field. The spun-up beams interact in a cylindrical waveguide. Bekefi's formulae show that the resonant frequency of the cyclotron double-stream interaction is proportional to the cyclotron frequency and is inversely proportional to the difference in the axial velocities of the beams. He predicts that the double-stream cyclotron maser can operate at high frequencies without the need of either high-beam voltage or high magnetic field. Later, a linear instability analysis of this maser was developed by Bekefi and his co-workers and the result of computer simulations shows that the cyclotron two-stream instability is primarily electrostatic [74]. A two-stream relativistic klystron amplifier and a high-power X-band relativistic two-stream amplifier were proposed in a similar idea [75, 76]. The operating principle of these schemes is also based on the unstable interaction of the *fast* cyclotron space-charge wave on one electron beam and the *slow* cyclotron space-charge wave on other electron beam.

The CRM-array was proposed by Jerby as an extension of the periodic-waveguide CRM scheme shown in Fig. 1.5a. In this device, referred here as a 1D CRM-array, the waveguide consists of metal posts in two columns, where the electron-beam flows in between them. Amplifier [46] and oscillator experiments [47] were conducted at X-band frequencies (8-12 GHz) with electron-beams of ~10 keV. The 1D-CRM oscillator yielded a coherent output of 0.4 kW power at >25% efficiency. Theoretical studies of 1D-CRM interactions with slow and fast waves are presented in [48]. A direct scale-up of this 1D scheme to high power levels might have required a system overhead comparable to that of

similar single-beam gyrotrons. The preferred alternative was to increase the device *dimensionality*.

Conceptual schemes of 2D and 3D CRM-arrays are illustrated in Figs. 1.5b and 1.5c, respectively. The CRM-array consists of many 1D CRM channels; each operates with a low-voltage, low-perveance electron beam. The different channels may be strongly coupled together through the waveguide lattice. Synergistic effects between these channels may increase the output power further. In order to compensate for any transverse non-uniformity in the magnetic field profile, each electron beam can be tuned to a slightly different accelerating voltage.

The ultimate 3D CRM-array may consist of tens, and even hundreds of electron beams. Advanced cathode arrays, made of carbon fibers, silicon tips, or ferroelectric ceramics, could be applicable in this device. The radiation output can be emitted from the exit plane of the CRM-array, directly to free-space. In more sophisticated schemes, the CRM-array may have features of an active phased-array antenna [63]. Focusing, steering, and splitting of the radiation lobe could be manipulated by varying the voltage profile across the cathode array.

The major advantages expected for the CRM-array concept are:

- (a) Reduced power-supply size and weight.
- (b) Reduced X-ray radiation level due to the low-voltage operation.
- (c) Miniaturization due to the integrated magnet.
- (d) Reduced space-charge effects due to the separated low-current electron beams.
- (e) Spectral purity and mode selectivity determined by the lattice dispersion.
- (f) Direct radiation to free-space.
- (g) Direct energy radiation as a phased-array antenna, incorporated in the multi-beam CRM-array itself.

The comparison of the single-beam high-power microwave source and the multi-beam CRM-array is summarized in Fig. 1.6.

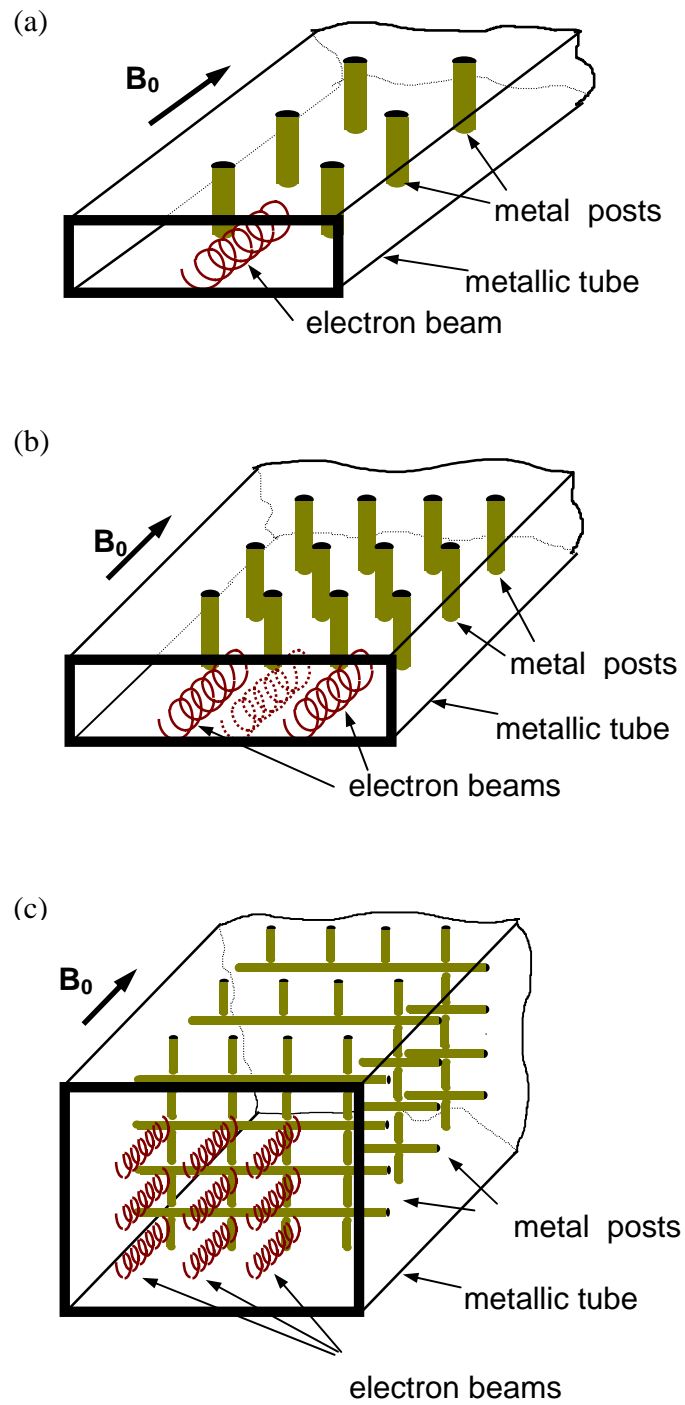


Fig. 1.5. The evolution of the CRM-array concept: 1D, 2D, and 3D CRM-array schemes (a, b and c, respectively).

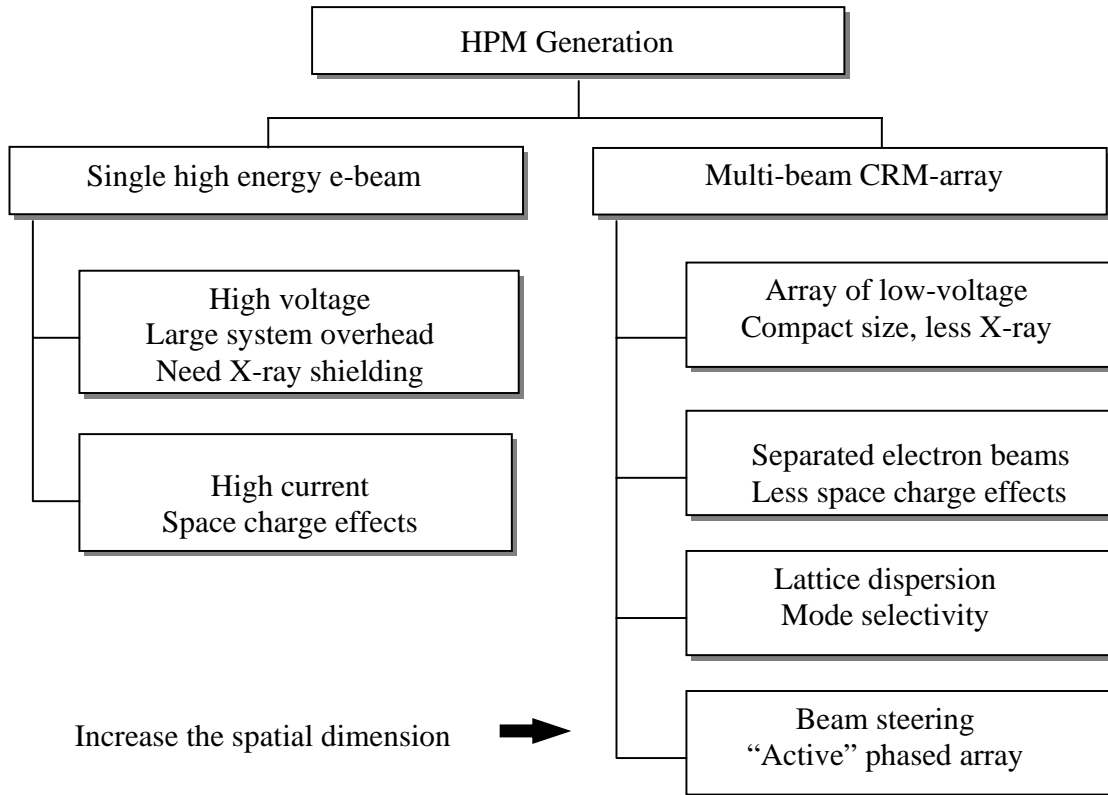


Fig. 1.6. Single-beam vs. multi-beam HPM generation.

1.3. Electron Emitters

There are several kinds of cathodes used in high power microwave devices. The most common cathodes are thermionic cathodes. Cold cathodes are also used. In this work we utilize both thermionic cathodes and cold cathodes.

Thermionic Cathodes

Thermionic cathodes are based on thermionic emission mechanisms. Thermionic emission results from the heating of the cathode to provide the electrons with a sufficient kinetic energy to overcome the potential barrier (work function) at the surface and escape

into vacuum. The current density J is given by the Richardson-Dushman equation as follows [77]:

$$J = A_0 T^2 \exp\left(-\frac{e\phi}{kT}\right) \quad \text{A/cm}^2 \quad (1.6)$$

where k is the Boltzmann constant, ϕ is the work function, T is the absolute temperature in degrees Kelvin ($^{\circ}\text{K}$), and $A_0 = 1.20 \times 10^6 \text{ A/cm}^2 \text{ } ^{\circ}\text{K}^2$.

However, in the case of space charge limitation, the current density J is given by the Langmuir-Child equation [78, 79]

$$J = 2.3 \times 10^{-6} G V^{3/2} \quad \text{A/cm}^2 \quad (1.7)$$

where V is the acceleration voltage in volts, and G is a quantity, given in cm^{-2} , which depends on the geometric configuration of the electrodes. In the simplest case of parallel-sided electrodes, $G = 1/d^2$, d is the cathode-anode distance. From Eq. 1.6, it is clear that in order to obtain a strong emission, the work function ϕ must be low and the temperature T must be high. Because Barium has a low work function (1.8 eV) and a moderate melting temperature (850°C), Barium impregnated tungsten cathodes have been widely studied since their introduction in the early 50's. The Philips B-type cathode developed by Levi [80, 81] in 1953 is still the most widely used cathode in the microwave tube industry. An improved version of the familiar impregnated cathode is the M-cathode [82], which employs a coating of an alloy of platinum group metals on the emissive surface to lower the work function of the activated cathode. Then this emitter may be operated at lower temperatures than the standard dispenser cathode for the same current density and has significantly longer operating lifetime. More recently, new types of cathodes have been investigated, for instance, a variety of versions of the impregnated dispenser cathode is distinguished by the composition of the impregnation or by the substrate type [83].

Cold Cathodes

The current density of conventional thermionic cathodes is limited to the order of 10 A/cm^2 [84]. For ultra high power microwave generation, a larger current density is required. In addition, direct modulation of the emitted beam can improve the efficiency

and reduce the size of the microwave source. Thus various cold cathodes have been developed over the years to meet those desires.

Cold cathodes do not rely on the heating of a material to emit electrons over the potential barrier. One of the most common types of cold cathodes is the field emitter, which is based on field emission. Field emission is the process whereby electrons tunnel through a barrier in the presence of a high electric field. Fowler and Nordheim developed a model describing the emission of electrons from a metal-vacuum interface in the presence of an electric field normal to the surface [85]. Their theory predicted that the current density of the field emission can be expressed as

$$J = \frac{C}{\phi t^2(y)} E^2 \exp\left(-\frac{B\phi^{\frac{3}{2}}v(y)}{E}\right) \quad \text{A/cm}^2 \quad (1.8)$$

where E is the applied electric field, ϕ is the work function, C and B are constants, $y = \sqrt{e^3 E/\phi^2}$, and $v(y)$ and $t(y)$ are tabulated functions which arise due the inclusion of image charge effects.

Dyke and Dolan have recognized the advantages of field emission as a high-brightness electron source in the 50's. They discovered that to ensure stable emission and long life on tungsten field emitters, the ultra-high vacuum is required [86]. Later, the group at Stanford Research Institute (SRI), lead by Spindt, has developed the gated field emitter arrays (FEAs) successfully using micro-fabrication technology [87]. The Spindt-type FEAs become one of the most common structures for field emission cathodes. The "Spindt cathode" is illustrated in Fig. 1.6. In the Spindt structure, the electrons are generated from very sharp molybdenum tips and an electron gate electrode is used to low the necessary operating voltage in order to produce a large electric field at the tips. Despite the variety of techniques and material, this kind of FEAs has been developed successfully as commercial flat panel displays, field emission displays (FEDs). Since FEDs have almost 180 degrees viewing angle, excellent color reproduction, flatness and low power consumption, it looks very promising.

There are many other types of cold cathodes, such as photocathodes, ferroelectric ceramic cathodes and explosive electron emission cathodes. We will describe more in detail the latter one in the following sections since this work has used carbon-fiber cathodes. For more details on other cathodes see, for example, the review article by Nation *et al.* [88].

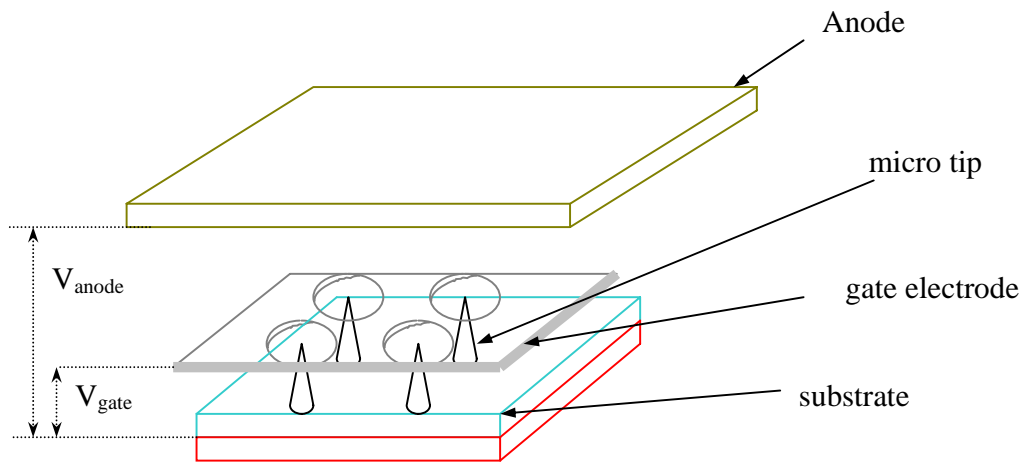


Fig. 1.6. Schematic of Spindt-type field emitter array.

Compared with field emitters, when the electric field is high enough, ohmic heating of the discrete electron emission sites will explode the cathode to vaporize and subsequent plasma formation by electron neutral collisions. There is also plasma formation on the anode, and diode gap closure occurs as the two plasma fronts expand. This process is known as explosive electron emission [88].

In USSR, Mesyats' group has made since the mid 1960's an extensive research on the processes of plasma formation and intense electron beams involved microscopic point emitters at high current densities emission. According their report, the work behavior of the explosive single emitter has four stages [89, 90]. Initially, followed a rapid rise in current a field emission current is observed after some delay by an explosive destruction

of the emitter. Simultaneous with the beginning of the current rise, a cathode flare appears on the cathode. Then, the current rises slowly, which is attributed to a decrease in the impedance due to plasma expansion. Later, an anode flare appears and the diode impedance collapses, simultaneous with a rapid current increase. The breakdown time, τ_δ , is related to the plateau current, j , by $j^2 \tau_\delta = \text{constant}$. Here j strongly depends on the electric field, so does τ_δ . If the explosion is initiated by field-emission current, the Fowler-Nordheim equation gives a good agreement with these single emitter experiments.

Focused on broad area cathodes, Parker and coworkers at the Air Force Weapons Laboratory studied in the 70's the electrical behavior of graphite cathodes. They considered that the observed diode perveance can be explained in terms of the expansion of the plasma cathode formed by the merger of many cathode flares [91]. The exact mechanism for broad area cathodes is not yet known; none of the theories so far proposed can explain all of the experimental results. However, the pre-breakdown and breakdown currents in a broad area cathode are observed to occur at electric fields about 10-1000 times lower than those in a single needle emitter [92]. The effect of gap closure may limit the performance of devices operating with cold-cathodes, since it limits the duration of the electron-beam pulse, and precludes operation at desired repetition rates [93]. Impedance collapse characterized by the speed of the gap closure is roughly constant over a wide range of conditions at values of about 10^6 cm/s. Because of the gap closure, most of the cathodes used limit the pulsed duration to about 100's ns. In order to prevent the breakdown, most studies in the cold cathodes use short pulse. It is useful, therefore, to develop new kinds of cold cathodes or processes, which the pulse lengths can be extended.

Recently, the researchers at NEC Corporation in Japan have demonstrated a miniaturized traveling waveguide tube (TWT) results of 27.5 W at 10.5 GHz, 19.5 dB gain, and a bandwidth wider than 3 GHz using a lateral-resistor-stabilized Spindt-type FEAs [94]. Another TWT design by NEC, using a new arc-resistant vertical current limiter Spindt-type FEAs resulted an 8 W output power, 22 dB gain at 11.5 GHz and was stably operated for 5000 hours [95, 96]. The arc-resistant FEA appears to dramatically

enhance the lifetime of the FEA cathodes in the vacuum environment and re-energize the efforts of researchers to develop high-power vacuum electronic devices based on cold cathodes.

Carbon fibers are known for a long time as field emission sources [97-99]. In these early works, carbon fibers have been studied as pure field emitters, having been used singly and in clusters to provide DC emission without plasma formation. The experimental results have a good agreement with the Fowler-Nordheim equation. The emission characteristics and stability of these cathodes are, to a large degree, determined by the type of the carbon fiber microstructure, by the features of the manufacturing process, and by the initial treatment of the emitters.

Further developments of carbon-fiber emitters with plasma formation in western countries were reported in the 80's by Prohaska and Fisher. Using carbon yarn, emission starts at 5-15kV/cm and 10-30kV/cm, current densities up to 10A/cm² have been obtained over 100 cm² [100]. Researchers in New Mexico demonstrated that cloth fiber (75% rayon, 25% silk) cathodes might have superior properties as cold cathode emitters [101]. However for the broad area carbon-fiber emitters, the experimental results do not agree with the Fowler-Nordheim equation. Even with extremely careful diode design, the available pulse duration for any of the carbon felt, velvet, and high-grade graphite cathodes is usually limited by gap closure. The gap closure velocity depends most critically on the electrical field strength at the cathode surface, the cathode emissive material, and magnetic field [102]. Most recently, experiments on carbon-fiber emitters have tested the effect of CsI (Cesium Iodide) coated carbon-fiber cathodes [103, 104]. They have found that carbon-fiber cathodes coated with CsI did reduce the speed of the gap closure. In our laboratory, the single beam carbon-fiber cathode was demonstrated for 1.2 ms current pulses [105], and was operated for a CRM experiment [106].

The carbon-fiber cathode is rarely used in microwave-tube experiments [107]. Since carbon has a high sublimation temperature (4×10^3 °K), it has a long lifetime at current densities of $>10^3$ A/cm² [103]. In addition, such kind of material can easily be configured

to provide multi electron beams in arbitrarily large diameter configurations. Therefore, in this study we use carbon-fiber cathodes to explore the operation of multi-beam cold-cathode arrays for the CRM devices.

1.4. Thesis Outline

The thesis describes the experimental studies of the multi-beam CRM-arrays. At present, our studies focus mainly on the establishment of the experimental fundamental frame of the multi-beam CRM-array. A secondary objective is to explore multi-beam CRM devices based on the cold-cathode arrays, carbon-fiber cathode arrays, and to develop an efficient, reliable and cost-effective multi electron-beam source.

In this thesis, Chapter 2 presents the first successful operation of a two-beam CRM-array. The spectral measurements were carried out with one and two-electron beam CRM devices. The chapter includes a detail description of the experimental setup, experimental operation, experimental results, and an analysis of the possible mechanism for the resonant microwave radiation observed. The first carbon-fiber CRM-array experiment is presented in Chapter 3. The multi-beam CRM scheme with cold-cathode arrays is demonstrated. This experiment illustrates the use of carbon-fiber emitters as electron sources in multi-beam CRM devices. Meanwhile, the study of the multi-beam carbon-fiber cathode array is described intensively in this chapter. The conclusions of this thesis are summarized in Chapter 4.

Chapter 2

2D CRM-Array Experiment

This chapter presents the first experimental study of a 2D CRM-array. The CRM-array operates with one or two electron beams. The next section describes the experimental design and setup. The operation of the experiment is described in Section 2.2. The highlights of the experimental results in each case are presented in Section 2.3. Both, fast- and slow-wave CRM interactions are observed in the experiment. The spectral measurements show clearly the CRM interaction with backward spatial harmonics. The experimental results are analyzed and compared to the theory in Section 2.4. The conclusions are presented in Section 2.5.

2.1. Experimental Design and Setup

A photograph of the experimental setup of the 2D CRM-array is shown in Fig. 2.1. The oscillator tube consists of a planar multi-beam electron gun, a 2D periodic waveguide, a collector, a solenoid, and a kicker coil, which imparts initial transverse velocity to the electrons. The total length of the system is about one meter.

A block diagram of the experimental setup is shown in Fig. 2.2. The CRM device is immersed in a uniform axial magnetic field (2-4 kG) and activated by pulsed power supplies. The electron beams are emitted from dispenser thermionic cathodes (Spectra-Mat, STD200, 5 mm diameter), spun up by the small kicker coil, and propagate in cyclotron motions along the periodic waveguide channels. The waveguide consists of a metal-post array with 4x24 elements and is terminated by half-period reflecting sections in both ends. The first row of metal posts acts as an anode. A waveguide taper at the end is used as a mode converter and also as a collector for the electron beams. In another scheme (not presented here) the collector is divided to each electron beam. The beam currents are measured by means of 10 Ω resistors. A small portion of the RF power is sampled by a 20 dB cross-coupler, and by three sampling probes mounted inside the

waveguide. The output coupled RF signal is attenuated and divided into two arms. In one arm, the signal is detected by a high-sensitivity crystal detector and recorded by a digital oscilloscope (Tektronix TDS 540). In the other arm, the signal is fed into a mixer (HP 5364A) and mixed with a local-oscillator wave generated by a synthesizer (HP 83752A). The heterodyne signal is analyzed by a frequency and time-interval analyzer (HP 5372A), which enables intra-pulse frequency variation measurements. The parameters of the 2D CRM-array experiment are listed in Table 2.1. The more detail design is given in the following sections.

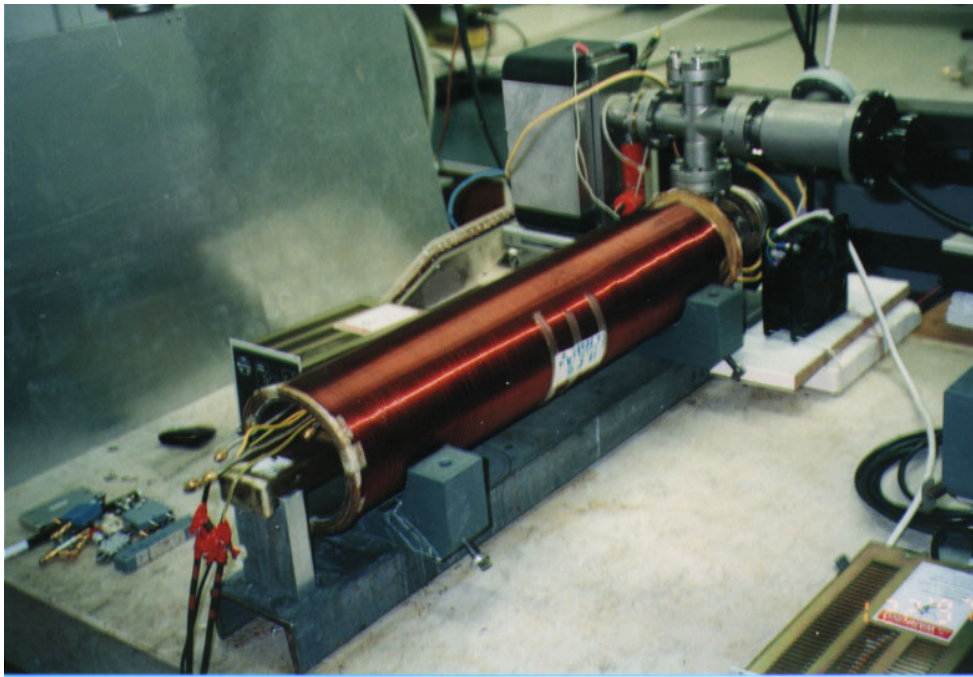


Fig. 2.1. Photograph of the experimental setup.

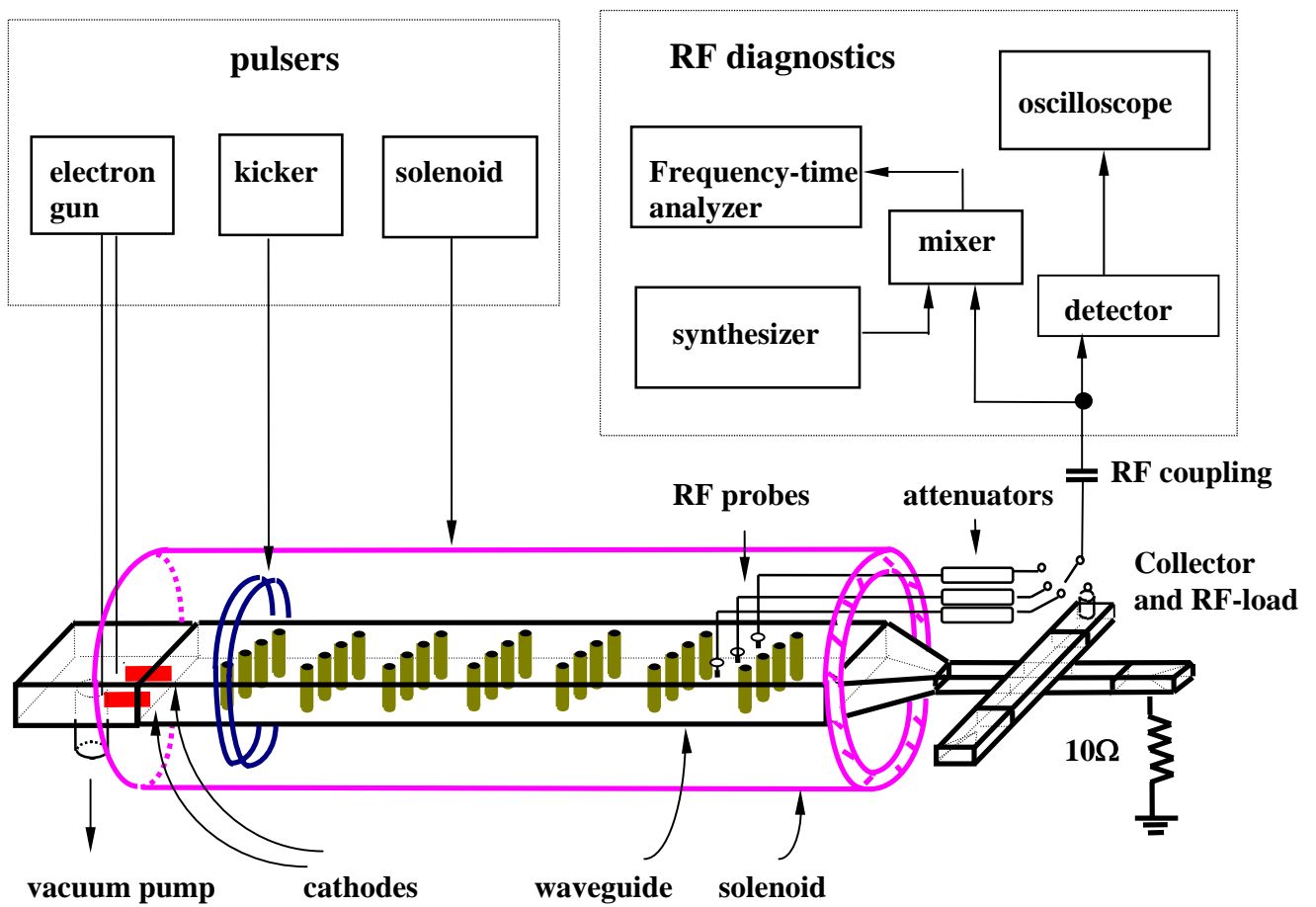


Fig. 2.2. Schematic of the 2D CRM-array experimental setup.

Table 2.1. 2D CRM-array Experimental parameters.

Electron beams:

energy	4.0 - 10.5 keV
beam current	~ 0.1 A
pulse duration	0.2 ms
beams	1 or 2

Magnetic fields:

solenoid	2.5 - 3.9 kG
kicker	~ 0.7 kA turns

Periodic waveguide:

rectangular tube	$48 \times 22 \text{ mm}^2$
length	48 cm
post diameter	1.5 mm
array size	4×24
periodicity	20 mm

2.1.1. Electron Beams

A planar electron gun was used in this experiment. A sketch of the electron gun is shown in Fig. 2.3. In the two-beam CRM experiment, the two side cathodes shown in red color in Fig. 2.3 were used to generate electron beams; whereas, in the one-beam CRM experiments, all of them were used separately to generate an electron beam in individual experiment. The gap between anode and cathode is 6 mm. A 2 mm thick stainless steel was used to fabricate the anode. The anode has three 6 mm diameter holes in order to apply the multi-beam operation. The distance between two adjacent cathodes is 9.5 mm. The cathodes are STD200 dispenser thermionic cathodes (5 mm diameter) made by Spectra-Mat Ltd. In a later experiment, for the vacuum consideration, we removed this anode and used the first row of metal posts in the periodic waveguide as an anode. For a new cathode, the optimal filament voltage is approximately 8V and the heating power is around 40 W.

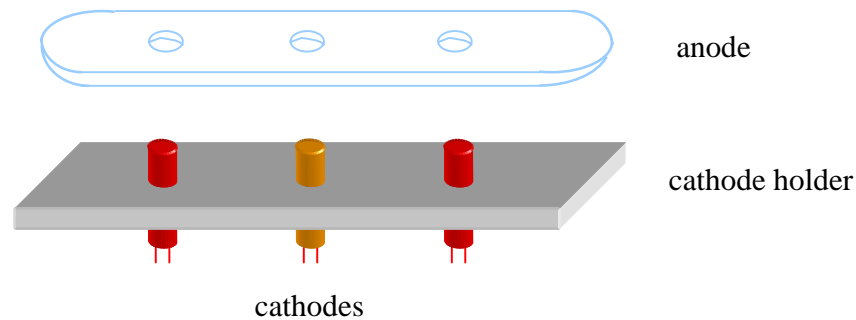


Fig. 2.3. Sketch of the electron gun used in the 2D CRM-array experiment.

The electron gun design was performed with the EGUN code [108] with a few assumptions. This code is designed to compute trajectories of charged particles in a 2D symmetry of electrostatic and magnetostatic fields, including the effects of space charges and self-magnetic fields. Starting options include Child's Law conditions on cathodes of various shapes, as well as user specified initial conditions. In the 2D CRM-array experiment, we assumed: (1) each beam has a perfect local symmetry around its own axis, (2) each beam has the same electron flow, (3) the gap between cathode and anode is smaller than the distance between two holes in the anode.

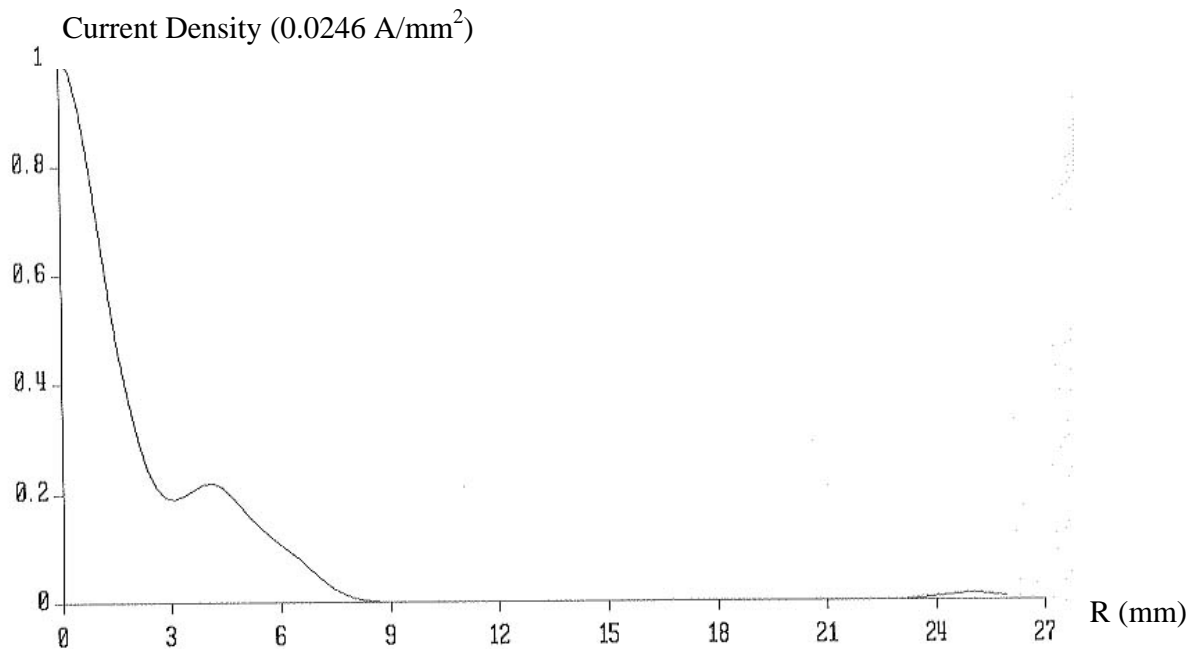
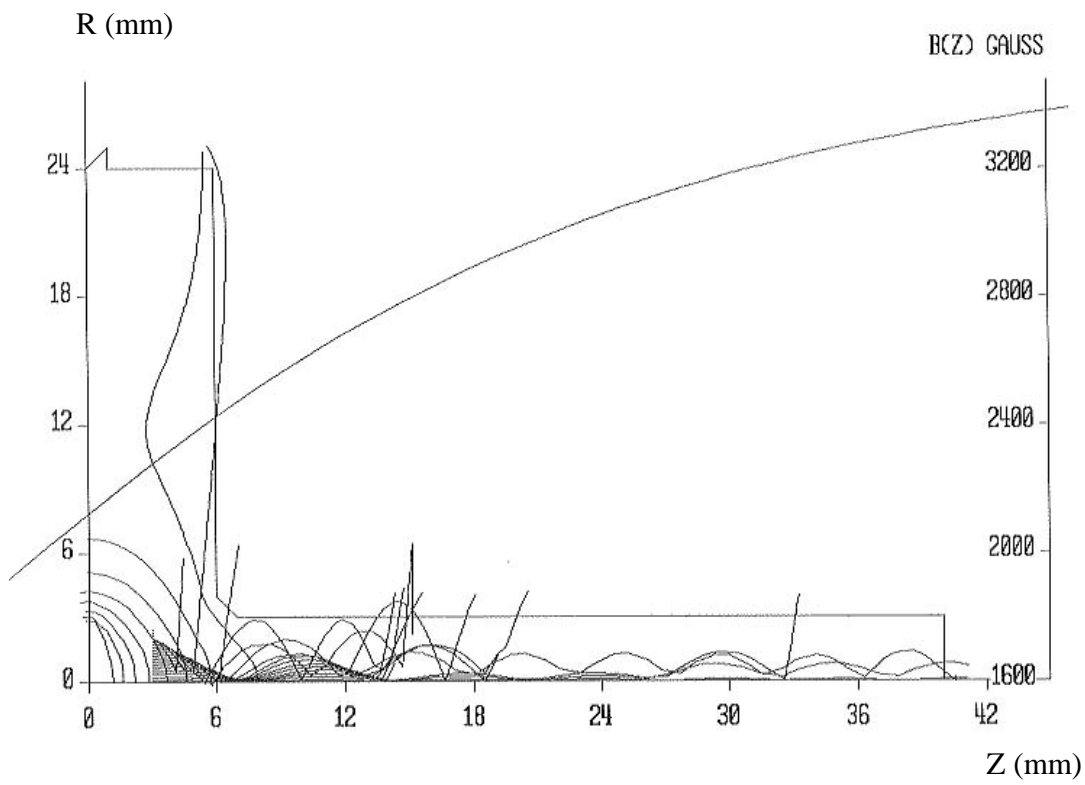


Fig. 2.4. The EGUN code output for a 5mm cathode and 6mm gap with a tapered magnetic field: (a) the beam trajectory [radius (R) vs. axial length (Z)], (b) electron density vs. radius (R).

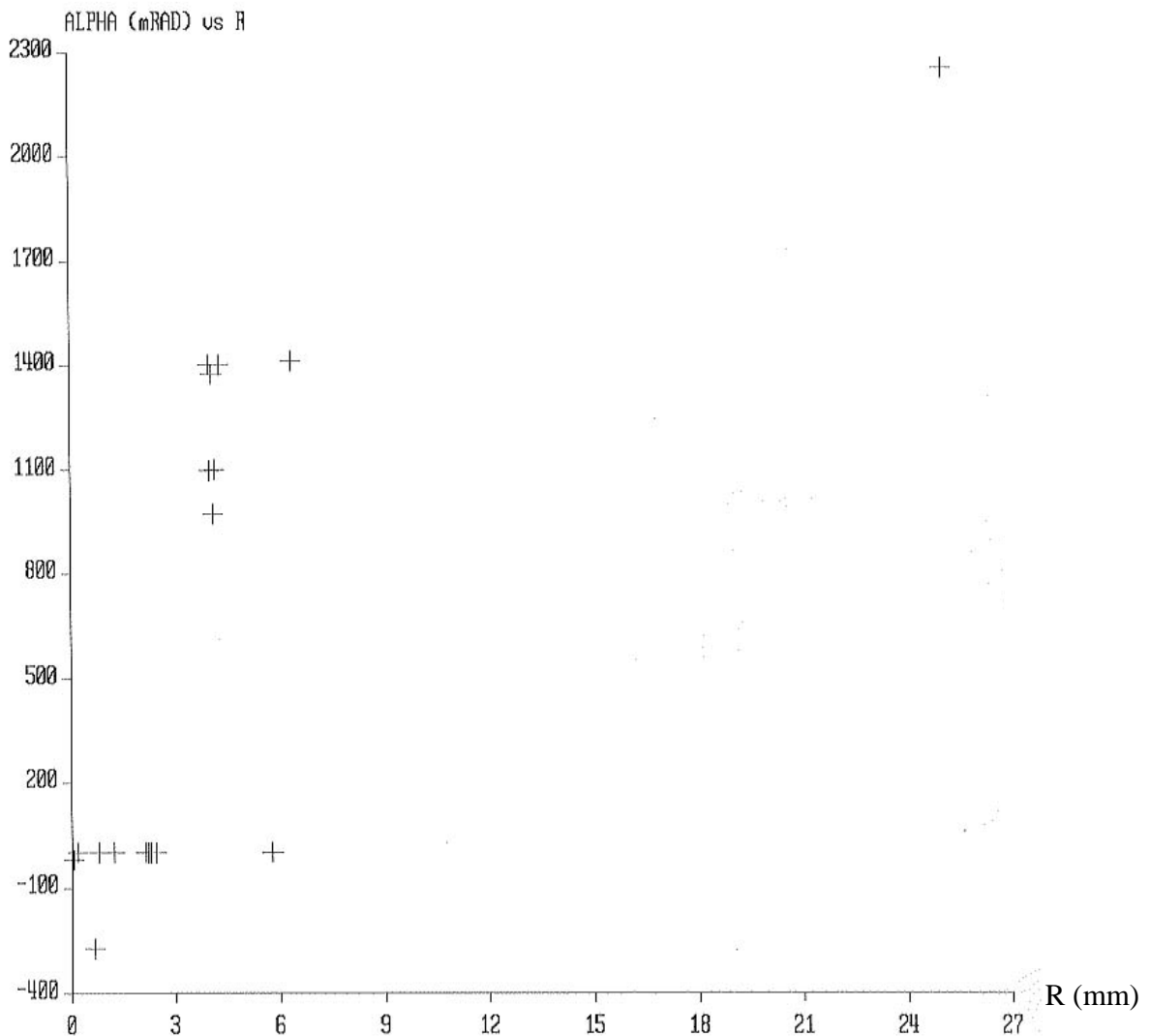


Fig. 2.4. (Cont.) The EGUN code output for a 5mm cathode and 6mm gap with a tapered magnetic field: (c) the angle of the electron motion measured from the z axis.

Thus we simulated the center electron flow and simplified the boundary. The code output for a 5 mm cathode with 6 mm gap is shown in Fig. 2.4. Fig. 2.4a shows electron gun geometry and beam trajectory. It includes two regions: a cathode-anode region and a beam tunnel. Figs. 2.4 b, c presents electron density versus radius, and the angle of the electron motion measured from the z-axis.

2.1.2. Magnetic Fields

In this experiment, we used a solenoid to provide an axial magnetic field for cyclotron motions. It was made out of a 2 mm diameter copper wire with 15 turns/cm. Similarly, a kicker was made out of a 1 mm diameter copper wire with 52 turns/cm. The cross section view of a round, finite, air core solenoid is shown in Fig. 2.5.

The magnetic field at any point on the axis of a finite solenoid is approximated [109] by

$$B_z(z) = \frac{\mu_0 N I_k}{2(r_2 - r_1)l} \left\{ \left(z + \frac{l}{2} \right) \ln \frac{r_2 + \sqrt{r_2^2 + \left(z + \frac{l}{2} \right)^2}}{r_1 + \sqrt{r_1^2 + \left(z + \frac{l}{2} \right)^2}} - \left(z - \frac{l}{2} \right) \ln \frac{r_2 + \sqrt{r_2^2 + \left(z - \frac{l}{2} \right)^2}}{r_1 + \sqrt{r_1^2 + \left(z - \frac{l}{2} \right)^2}} \right\} \quad (2.1)$$

where B_z is the magnetic field, in Tesla, μ_0 is the permeability constant (1.26×10^{-6} H/m, for coils measured in meters). I_k is the current in Amperes. l , r_1 , r_2 , and N are the solenoid length, inner and outer radii, and the number of turns, respectively, The experimental parameters are shown in Table 2.2. In Fig. 2.6, the solid curve shows the magnetic field of the solenoid and the dashed curve shows the magnetic field of the kicker. The star sign indicates the front-end position of the cathodes.

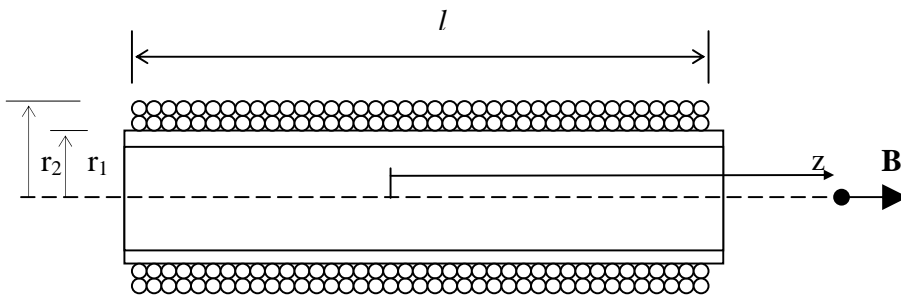


Fig. 2.5. Solenoid in cross section.

Table 2.2. The parameters of the solenoid and the kicker.

Parameter	Solenoid	Kicker
Turns	900	120
Current [A]	100-200	20-140
Inner radius r_1 [cm]	5.15	5.5
Outer radius r_2 [cm]	6.3	6.5
Length l [cm]	60	2.3

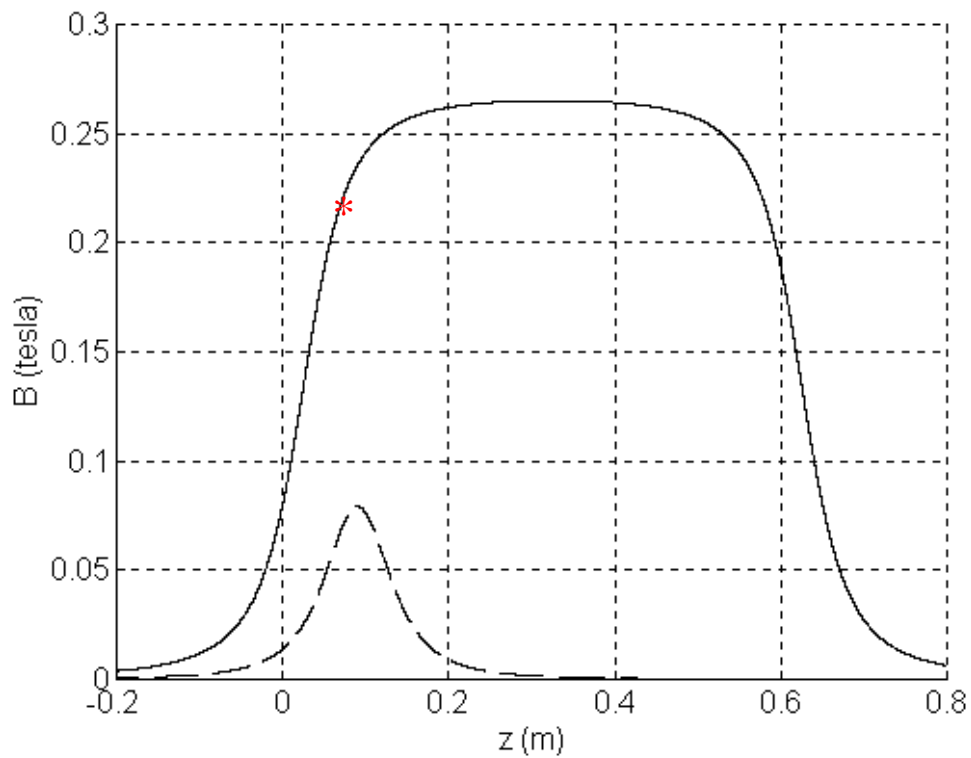


Fig. 2.6. The magnetic fields of solenoid (solid curve) and kicker (dashed curve). The star sign represents the start point of the electron beam.

2.1.3. Pulsed Power Devices

Three high-voltage pulsers were designed and built in order to run the CRM experiment. The three incorporate pulsers are used for the electron gun, solenoid, and kicker. Their electric circuits are shown in Appendices B1 and B2. An overview of the pulsers is shown in Fig. 2.7. Each of the pulsers consists of a low-voltage capacitor bank (C), an SCR control circuit which is used as a gate, a diode D_c which prevents a reverse recharging of the capacitor, and a transformer (car ignition coil). Fig. 2.8 shows schematically a principle configuration of a high voltage electron gun pulser [110]. In this scheme an electron gun serves as a load. The high-voltage secondary winding of the transformer is connected directly to the electron gun. The pulse length, the voltage, the maximum currents, and the load's parameters determine the parameters of each pulser. Fig. 2.9 shows schematically a principle configuration of a high voltage solenoid pulser. Here high voltage comes out from charged capacitors directly. The homemade solenoid pulser generates a 650 V, 40 ms pulse that corresponds to a peak magnetic field of 3 kG. The electron gun pulse reaches 12 kV and its pulse width is around 0.4 ms. The kicker coil can produce 7 kG maximum magnetic field on axis. All three pulsers are triggered with an adjustable delay between them. The kicker and electron gun pulsers are triggered near the peak of the solenoid pulse as shown in the timing diagram in Fig. 2.10. The solenoid pulse has 40 ms duration. Comparing to the 0.4 ms duration of the electron gun pulse, the CRM operates in a closely constant magnetic field. The electron gun voltage is measured by a high voltage probe (Tektronix P6015A). The currents of the solenoid and the kicker are measured with a series 0.05 Ω resistors.



Fig. 2.7. Overview of the homemade pulsers.

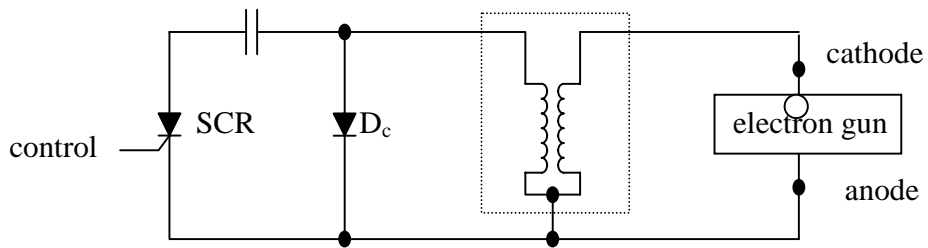


Fig. 2.8. Schematic of the electron gun pulser.

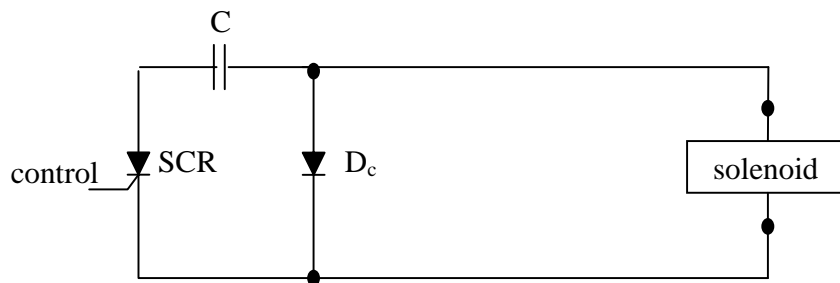


Fig. 2.9. Schematic of the solenoid pulser.

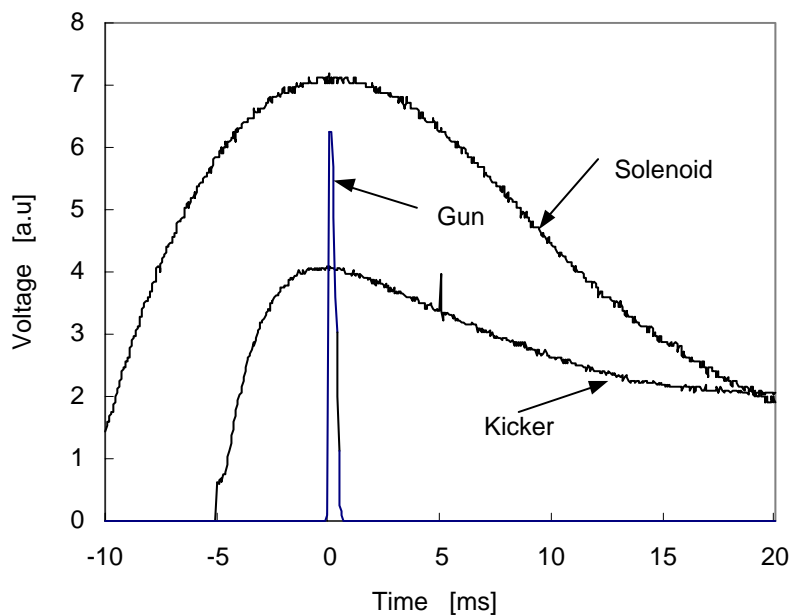


Fig. 2.10. A timing diagram of the solenoid, kicker and electron gun pulsers.

2.1.4. The Periodic Waveguide

The periodic waveguide used in this experiment is illustrated in Fig. 2.11. The main part is a 60 cm long WR 187 waveguide welded with a 4×24 metal-post array. It is terminated by half-period reflecting sections in both ends. The first row of metal posts acts as an anode.

It is well known that any periodic slow wave structure of N periods, when shorted appropriately at both ends, will exhibit (N+1) discrete resonant frequencies with phase shifts per period equally spaced between 0 and π . Generally speaking, these specific resonant modes can be determined experimentally and then used to fit a curve to give the complete dispersion function. Using the method described in Refs. [111, 112], the minima in the reflection trace present the resonance frequencies of the finite periodic waveguide, and satisfy the resonance condition

$$\phi_s = \beta_s L = s\pi, \quad s=1,2 \dots 24 \quad (2.2)$$

where ϕ_s is the phase shift, β_s is the discrete wavenumber, and L is the waveguide length. The dispersion curve is constructed by the measured frequencies of the reflection minima and the discrete wavenumbers.

The cavity resonances were measured with the reflection coefficient of the slow wave structure over the appropriate frequency range. The measured results at the first and second passbands are presented in Fig. 2.12 and Fig. 2.13, respectively. The curves show the measured resonant absorption peaks corresponding to 23 axial modes of the cavity. This was achieved by a scalar network analyzer (HP 8757A). The testing system setup is shown in Fig. 2.14. The waveguide dispersion (without electron beams) is shown as a Brillouin diagram in Fig. 2.15, as results from measurements of the waveguide reflection and transmission coefficients. The dots indicate the measurement points of the 2D periodic-waveguide. The dashed curve indicates the fundamental mode of the rectangular tube.

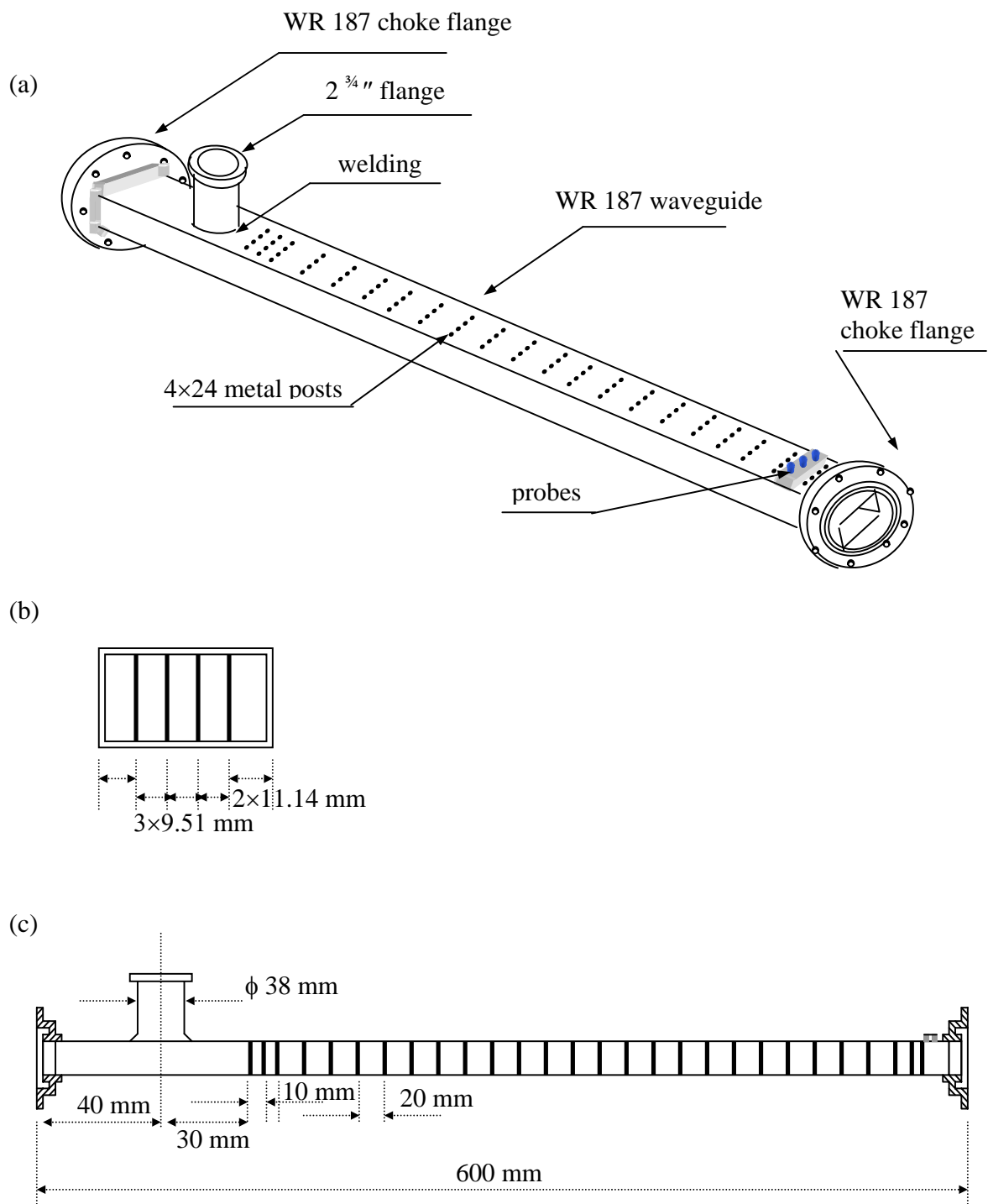


Fig. 2.11. The periodic waveguide construction, (a) an overview, (b) a cross section view, and (c) a side view.

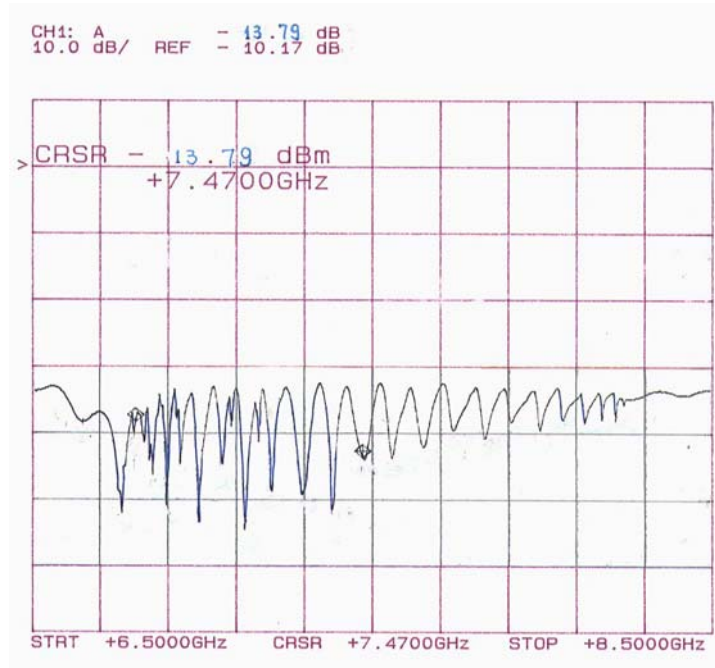


Fig. 2.12. The measured reflection curve at the first passband.

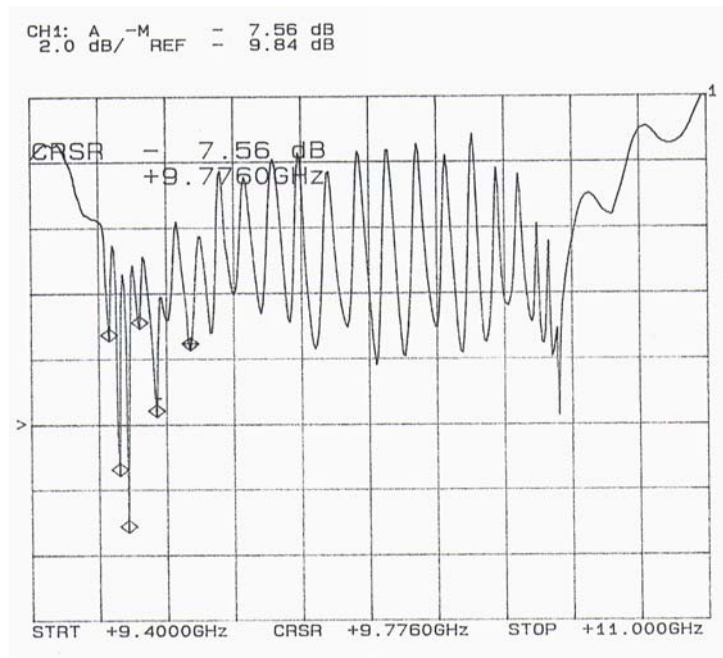


Fig. 2.13. The measured reflection curve at the second passband.

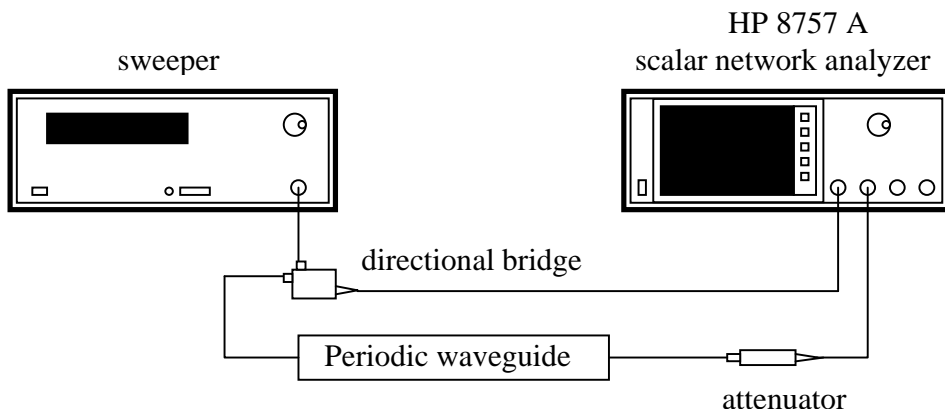


Fig. 2.14. A block diagram of the testing system used for the measurement of the dispersion relation.

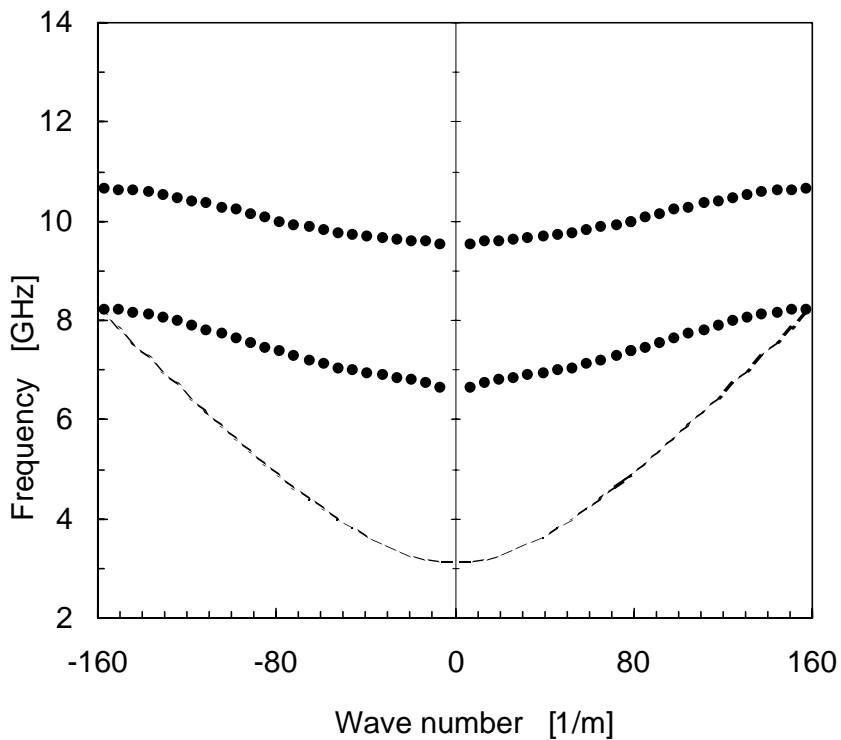


Fig. 2.15. The measured Brillouin-diagram of the 2D periodic-waveguide (the dots indicate measurement points). The dashed curve indicates the fundamental mode of the rectangular tube.

2.1.5. Vacuum System Considerations

In general, metals, ceramics, and some plastics, such as Teflon are satisfactory in systems having ultimate vacuums down to 5×10^{-7} Torr. In this experiment, the main vacuum chamber is the periodic waveguide shown in Fig. 2.11. It connects with pump system through a 2 ³/₄" flange. The parts of feedthroughs and window are connected by O-ring type connectors. Generally, the tube is pumped down to a pressure less than 10^{-6} Torr by a Varian 20/1 triode pump (model 911-5030). A Varian Turbo-V250 pump (model 969-9008) is used for rough pumping. Most of the time, the system will need to be baked to 100 °C (since we have O-ring, this temperature can not be too higher).

2.1.6. RF Diagnostics

The details of the experimental diagnostic setup are shown in Fig. 2.16. The RF diagnostics can be classified into two aspects, power measurement and frequency diagnostic. For power measurements, a Schottky barrier diode is used to rectify and detect the envelope of a RF pulse, generating a nonlinear DC output in the instantaneous electric field. Then this DC output is recorded by a digital oscilloscope (Tektronix TDS 540). A key factor to protect the detectors is the accurate attenuation of RF signals. Two methods of the frequency diagnostic are used, one based on the measurement by bandpass filters and the other based on the measurement by a frequency and time-interval analyzer (HP 5372A). A waveguide (WR 187) which has a cutoff frequency of 3.28 GHz is used. Afterward, two filters are used for a coarse survey of the frequency. Their bandpass are 5.68-7.45 GHz and 8.13-10.00 GHz, respectively. According to the coarse measurement of the frequency, a local signal (LO) from a synthesizer (HP 83752A) is selected. The LO signal is mixed with the RF output signal. Then the heterodyne IF signal is sent to the frequency and time-interval analyzer (HP 5372A) for the accurate frequency measurement. A power limiter is used to protect the frequency and time-interval analyzer. All data are recorded and processed on-line with the aid of a PC. The communications are through GPIB interface cables and a HP VEE 3.0 software is used to collect data.

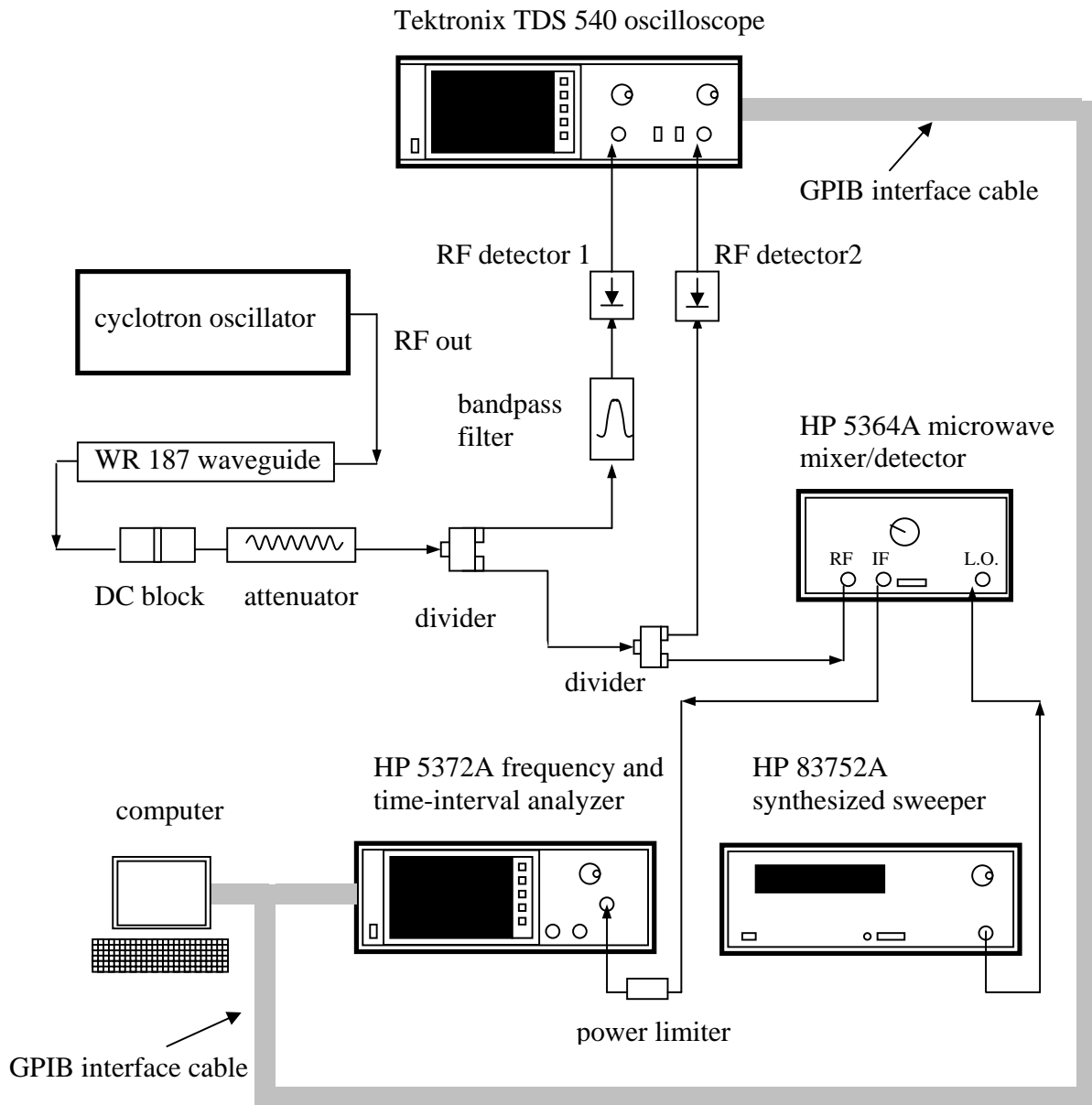


Fig. 2.16. The experimental diagnostic setup. It includes power measurement and frequency diagnostic.

2.2. Experimental Operation

Each experiment began with a warm-up period, typically a few hours, to activate the cathodes. Initially, the filaments were operated at a potential, of ~ 6 V. Then the potential was gradually increased to ~ 8 V in order to obtain the desired currents. For used cathodes, this potential has to be increased to 11 V. In the two-beam CRM experiment, we used two individual AC power supplies to heat the cathodes separately in order to get a uniform current in each beam. The AC supplies must isolate the electron gun voltage from the ground potential. The electron gun was adjusted to provide a 0.2 ms pulse at the desired current level (0.1-0.5 A). Typical voltage pulse of the electron gun and the beam current trace are illustrated in Fig. 2.17. The beam current was measured by a 10Ω resistor placed between collector and ground. In the experiment, the periodic waveguide is connected to a ground potential, and the collector has to be isolated from the ground.

The adjustment of the solenoid position, the calibrations of the diagnostic system, and cold measurements were conducted prior to each experiment. The desired uniform axial magnetic field was obtained by adjusting the solenoid position properly (the current trace in the collector should be clear), and by adjusting the peak level of the current pulse in the solenoid. Any directional change of the electron beams requires the re-alignment of the solenoid.

The experiment was initiated by the main pulser, solenoid pulser; sequentially following by the kicker current pulser, the electron gun voltage pulser, and the data acquisition system. Except the RF signal diagnostic, the results to be recorded include the collector current, the solenoid current pulse, the kicker current pulse, and the electron-gun voltage pulse during the experiment. When we seek the RF signal, we scanned the axial magnetic field in the design region, accompanied by a scan of the kicker current. The electron energy distribution was determined with the timing relationship between the electron gun pulse, axial magnetic field and kicker current. Attenuators were used at each experiment in order to protect the detectors.

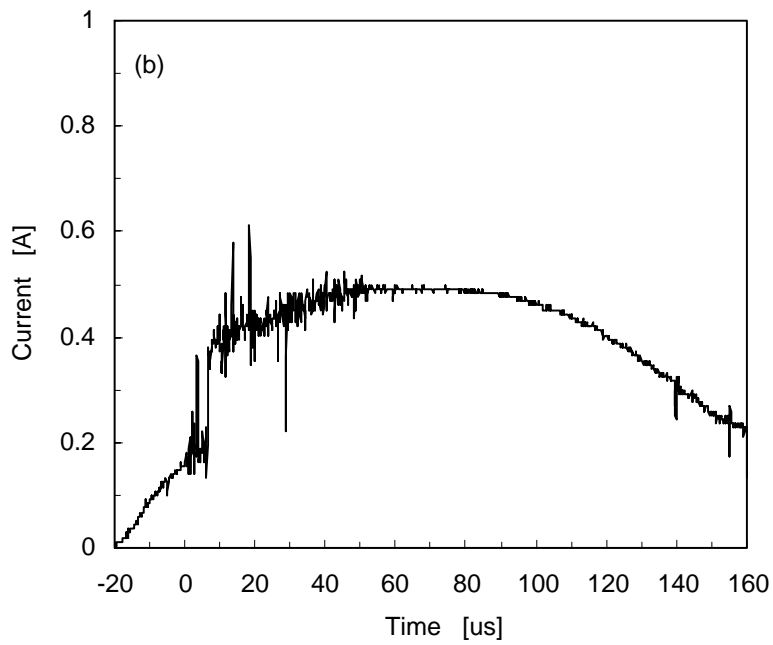
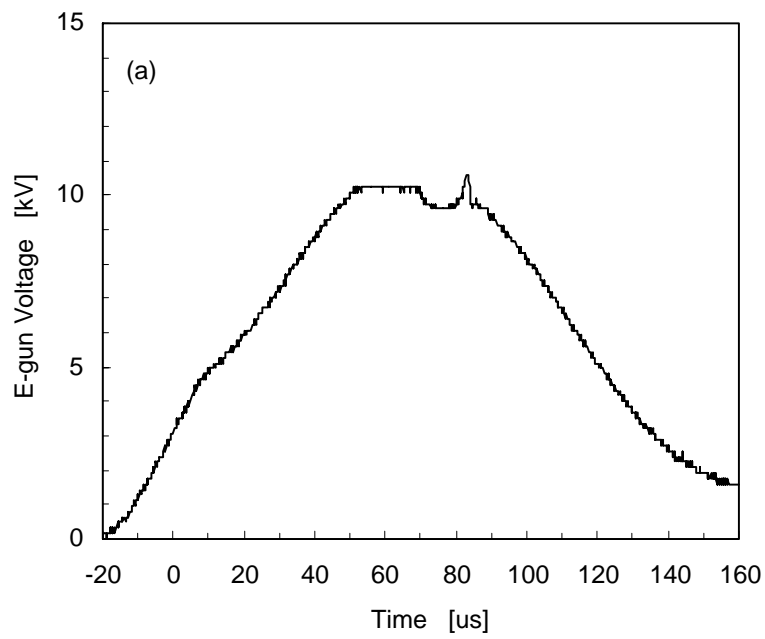


Fig. 2.17. An electron gun voltage trace (a) and a single beam current trace (b).

2.3. Experimental Results

The 2D CRM-array experiment has been operated with one and two electron beams, as illustrated in Fig. 1.5b by dashed and solid curves, respectively. A single electron-beam in the center channel yielded the results shown in Figs. 2.18 and 2.19. The detector output trace is presented in Fig. 2.18a, together with the electron-beam energy trace. The frequency characteristic of the RF output signal is shown in Fig. 2.18b as measured during the pulse (the dots present the points of the measurement). The axial magnetic field in this run is 2.9 kG, which corresponds to a cyclotron frequency of 8.0 GHz. The current measured in the collector is ~ 0.1 A. The average radiation frequency is 7.5 GHz, hence the device operates with a backward wave. This effect is clearly observed in Figs. 2.18a,b by the curvatures of the voltage and frequency traces (note that in a backward wave interaction, the frequency decreases as the electron energy increases). A slightly higher electron energy results in a *rabbit-ears* shape of the detector output, as shown in Fig. 2.19. The optimal resonance in this tuning condition is satisfied below the maximum voltage.

Single-beam measurements have been made in a wide range of axial magnetic fields and electron gun voltages. Oscillations were observed in different frequencies as shown in Figs. 2.20a-d. In all cases, the RF frequency tends to decrease as the electron energy increases. For axial magnetic fields in the range 2.6-2.9 kG (Figs. 2.20a-c), the corresponding wave frequency varies within 6.87-7.52 GHz, respectively, in the first passband of the periodic waveguide. For an axial magnetic field of 3.7 kG, interactions were observed in the second passband (9.75 GHz), as shown in Fig. 2.20d. In the second passband, the coupling is much smaller since the interaction occurs mostly with the second transverse mode, which has a null in the center. The emission in this case may result from the finite width of the electron beam, or from its slightly off-axis propagation.

The CRM-array was operated also with a single electron-beam in the side channel. A typical result for a 2.7 kG magnetic field is presented in Fig. 2.21. The extracted power of the RF sample by the various couplers in all the single beam measurements was in the range of 5-25 W. This power level is sufficient for spectral measurements.

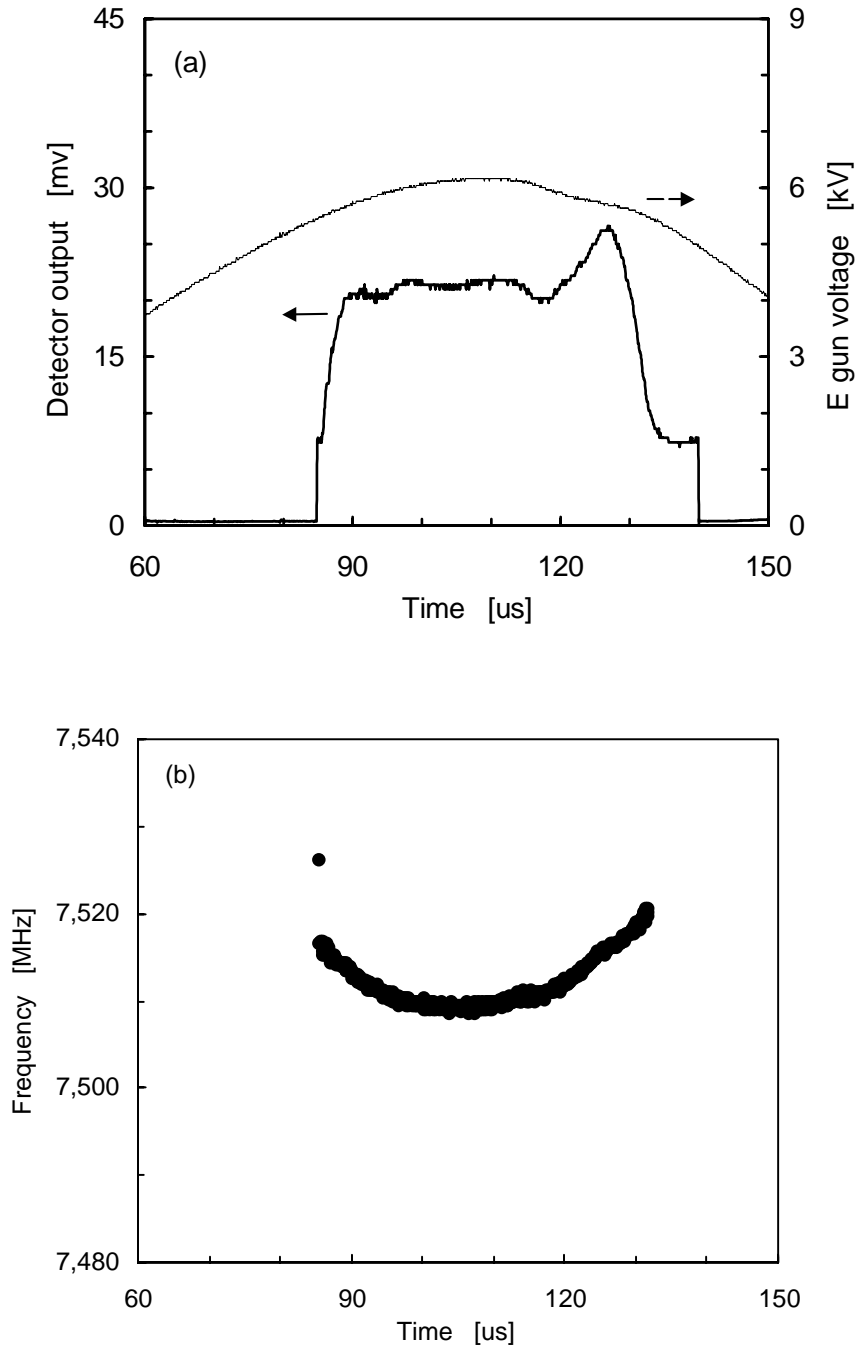


Fig. 2.18. Experimental results of the one-beam CRM oscillator at 2.9 kG: (a) the electron gun voltage (upper curve) and the detector RF output (lower curve), (b) the frequency variation during the pulse.

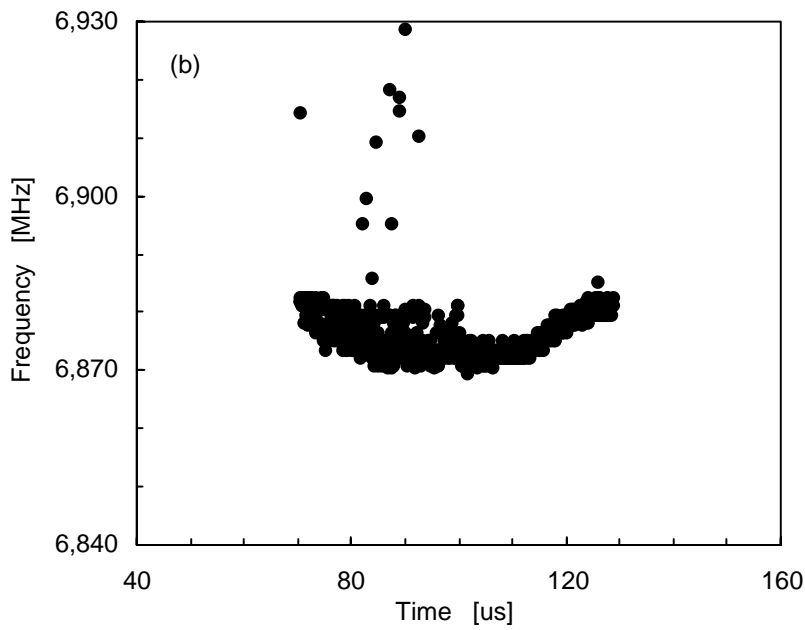
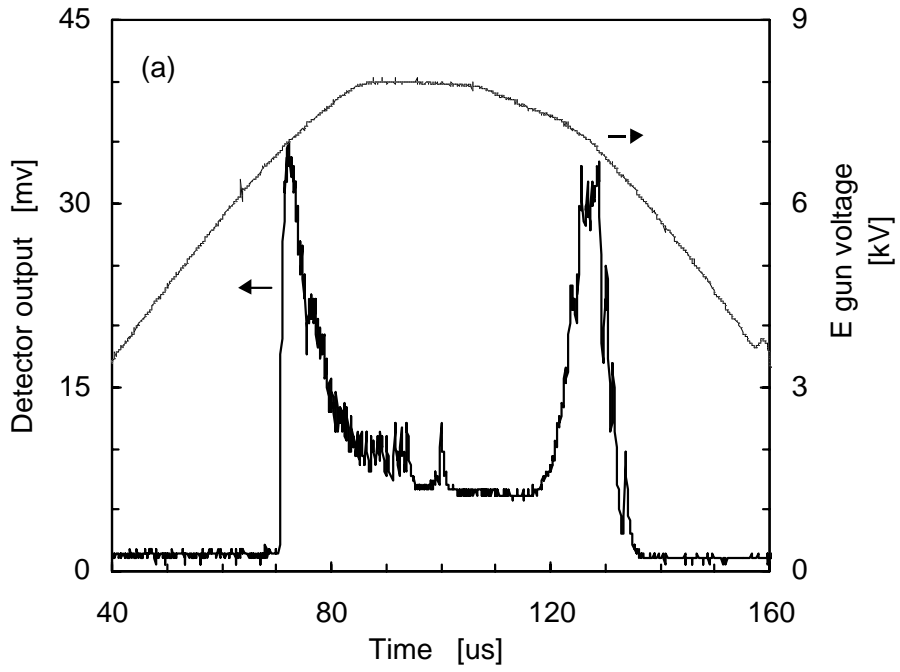


Fig. 2.19. An off-tuned operation at 2.7 kG: (a) the electron gun voltage (upper curve) and the detector RF output (lower curve), (b) the frequency variation during the pulse.

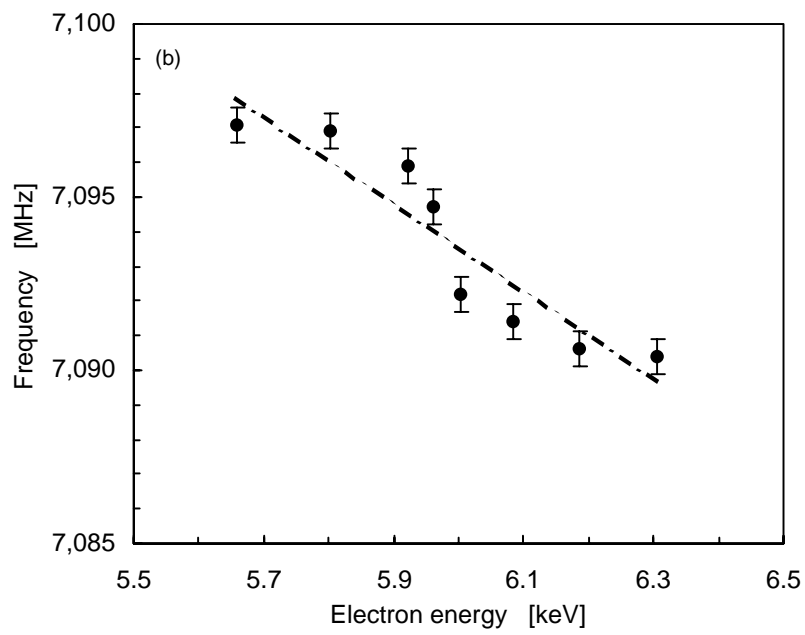
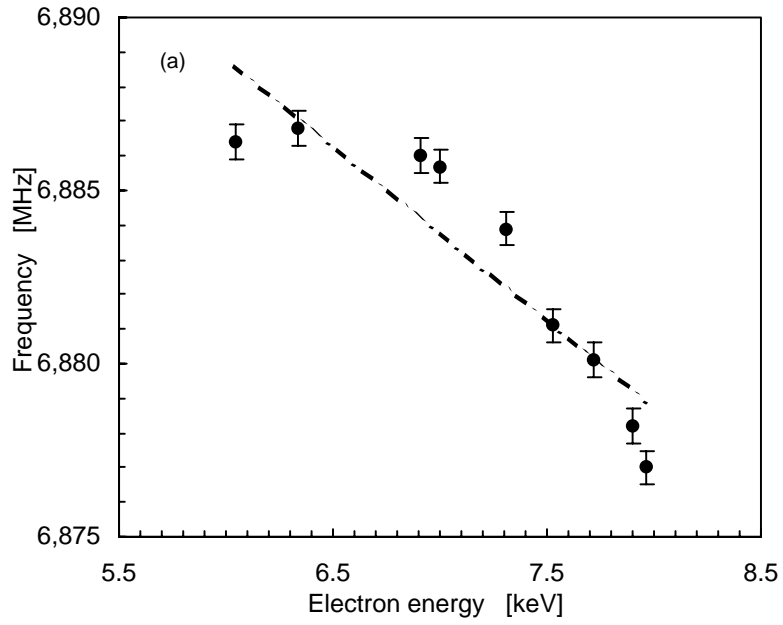


Fig. 2.20. Tuning characteristics of a one-beam CRM, at (a) 2.6 kG, (b) 2.7 kG.

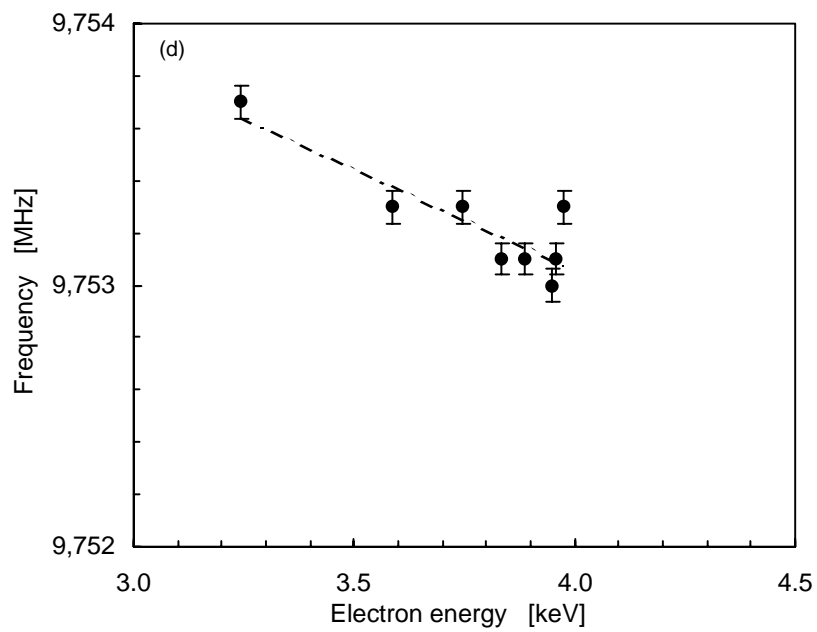
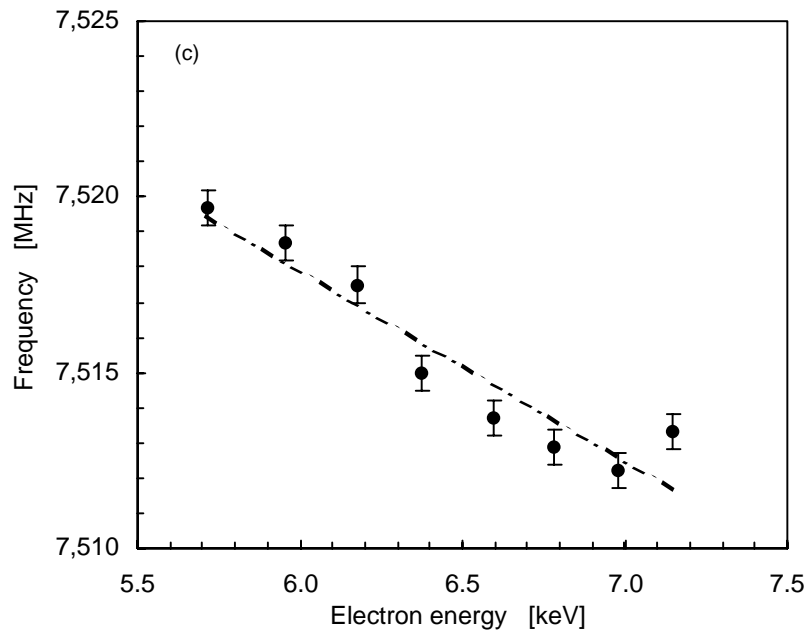


Fig. 2.20. (Cont.) Tuning characteristics of a one-beam CRM, at (c) 2.9 kG, (d) 3.7 kG.

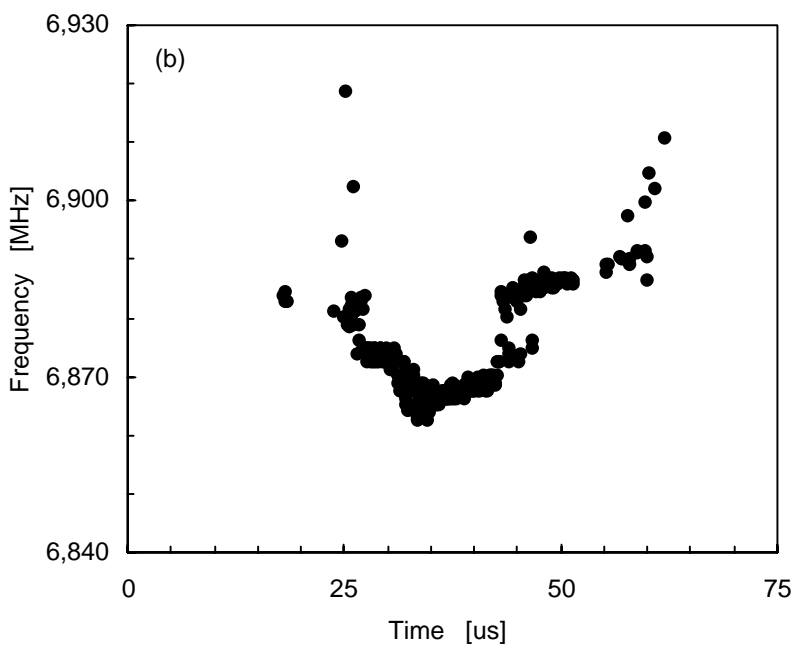
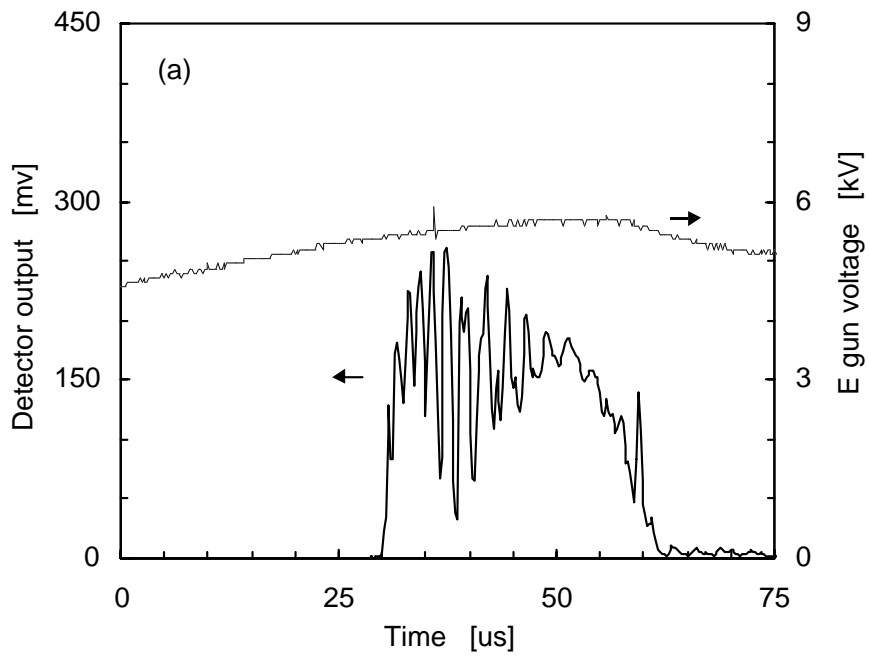


Fig. 2.21. A 2D CRM-array operation with a single beam in an off-axis side channel at 2.7 kG: (a) the electron gun voltage (upper curve) and the detector RF output (lower curve), (b) the frequency variation during the pulse.

The 2D CRM-array was operated with two electron beams as shown in Fig. 1.5b. Typical curves of the detector output and the electron gun voltage pulse are shown in Fig. 2.22a. A frequency variation of the RF output signal is shown in Fig. 2.22b. The axial magnetic field in this run is 2.7 kG, which corresponds to a cyclotron frequency of 7.56 GHz. The average radiation frequency is 6.9 GHz, hence the device operates again in the backward-wave regime. In a CRM operation with an electron-energy slightly higher than the optimal value, the synchronism condition takes place in the leading and trailing edges of the voltage pulse, as shown in Fig. 2.23.

By increasing the axial magnetic field, the two-beam CRM oscillates also at 3.8 kG. Figs. 2.24a,b show the electron gun voltage, the detector output and the intra-pulse frequency variation in this case. The corresponding cyclotron frequency is 10.64 GHz and the radiation frequency is 6.7 GHz. This result was obtained without a kicker field. Comparing to the one-beam CRM experiments, in the two-beam CRM experiment, the cathodes have off-axis positions. Then the transverse magnetic field exists for both cathodes. The transverse velocity of the electrons for the CRM interaction in this case may result from the nature kicking of the solenoid magnetic field.

A series of measurements were made in different electron gun voltages in axial magnetic fields of 2.7 kG and 3.8 kG (7.56 GHz and 10.64 GHz cyclotron frequencies, respectively). For 2.7 kG, the corresponding wave frequency is around 6.9 GHz, and the sampled output power by the probe is ~20 W. For an axial magnetic field of 3.8 kG, the interaction occurs around 6.7 GHz without a kicker, and the sampled output power is ~6 W. Maps of RF-frequency vs. electron-energy accumulated in many runs are shown in Figs. 2.25a and b for 2.7 kG and 3.8 kG, respectively (note that each dot presents average values of the corresponding run). The electron energy acceptance for 2.7 kG is much larger than for 3.8 kG, presumably because of the smaller Doppler shift.

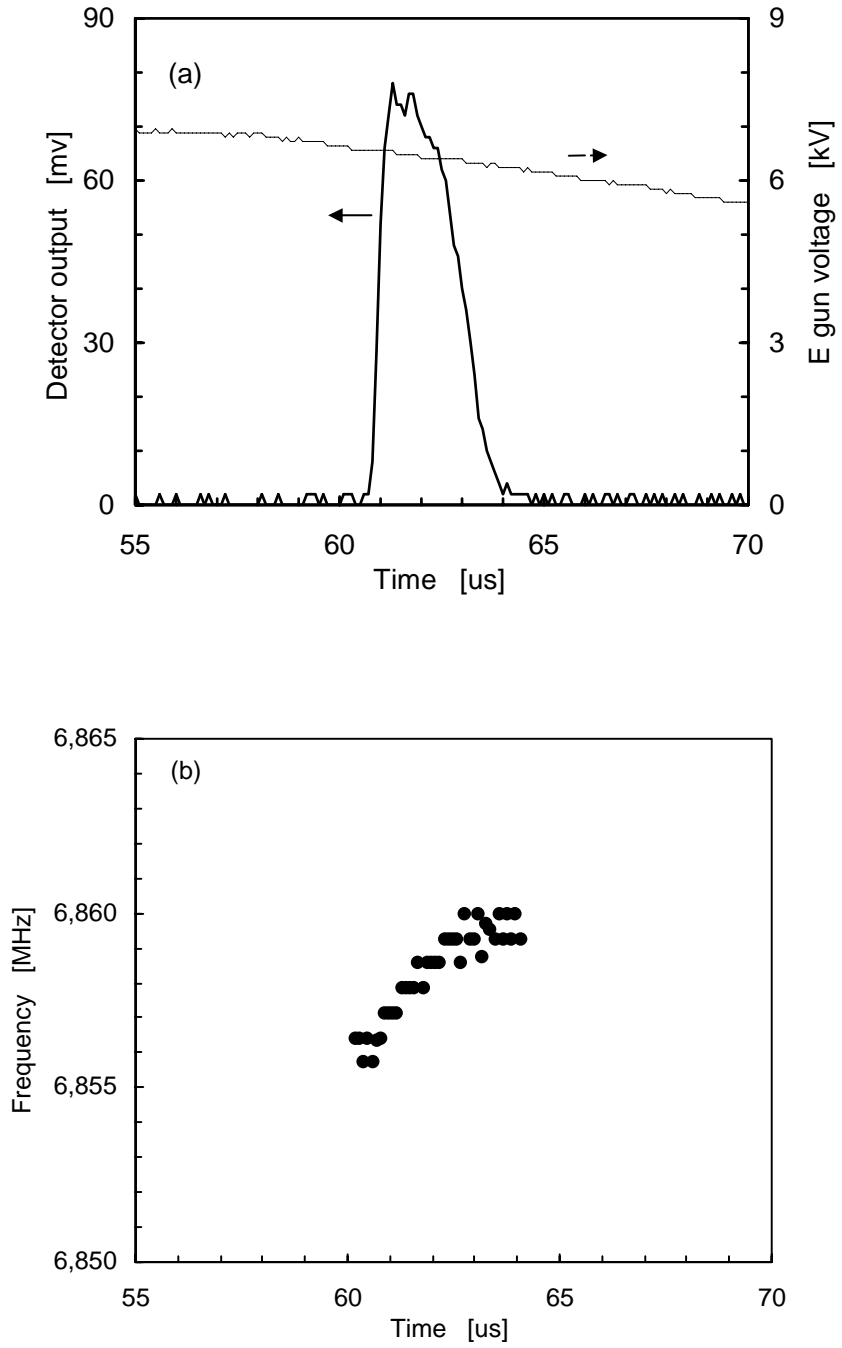


Fig. 2.22. A two-beam CRM oscillator output at 2.7 kG: (a) the detector output (sharp curve) and the electron gun voltage (flat curve), (b) the frequency variation during the pulse.

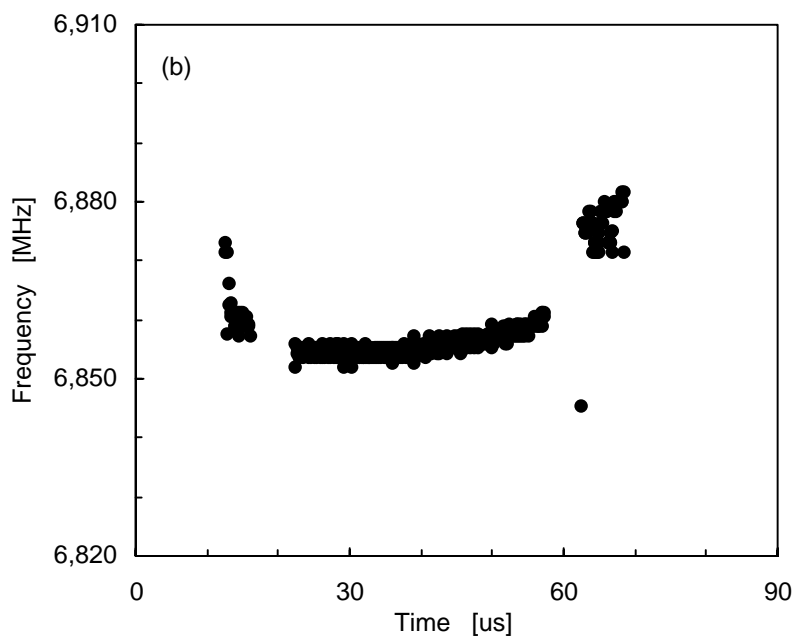
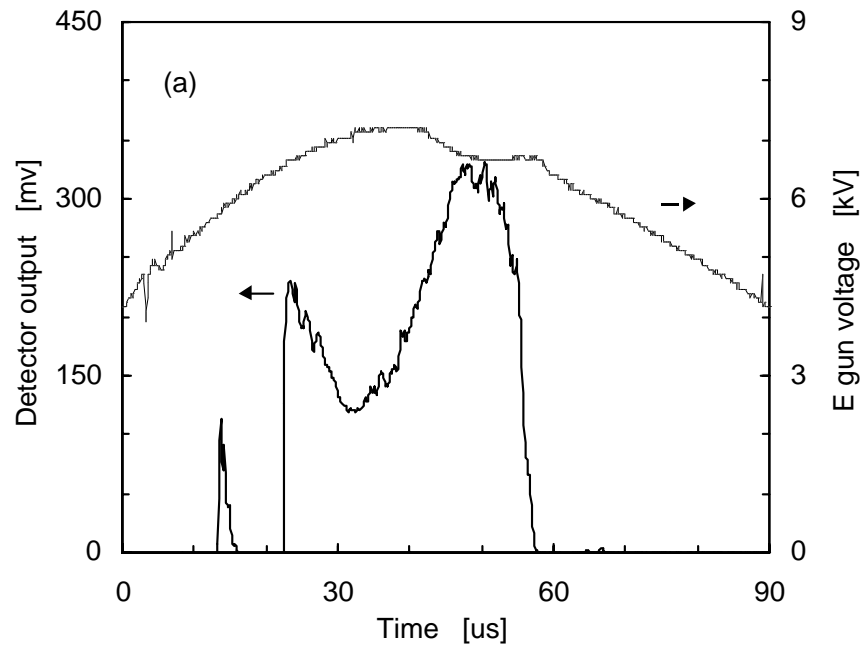


Fig. 2.23. An off-tuned operation of two-beam CRM oscillator: (a) the electron gun voltage (upper curve) and the detector output (lower curve), (b) the frequency variation during the pulse.

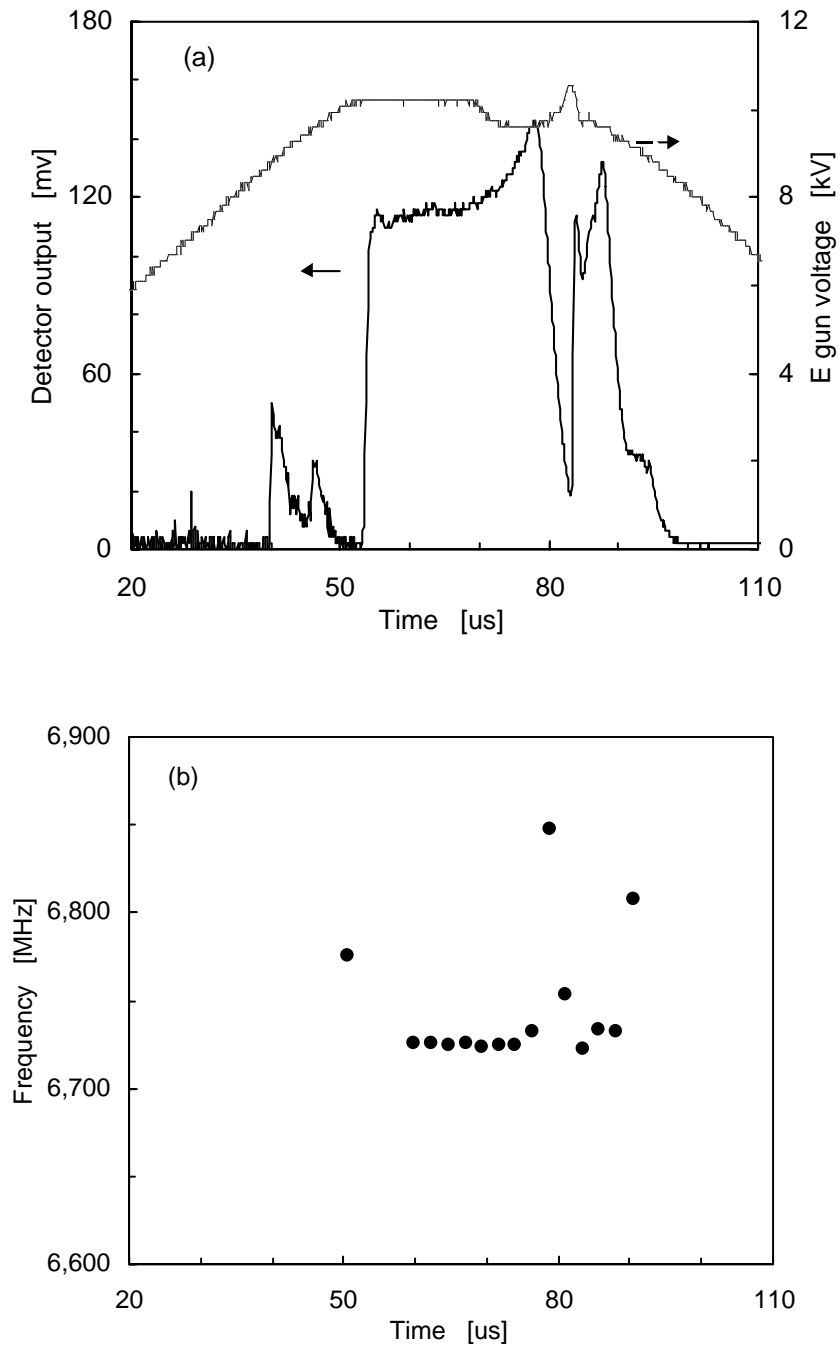


Fig. 2.24. A two-beam CRM operation at high magnetic field, 3.8 kG: (a) the electron gun voltage (upper curve) and the detected RF output (lower curve), (b) the frequency variation.

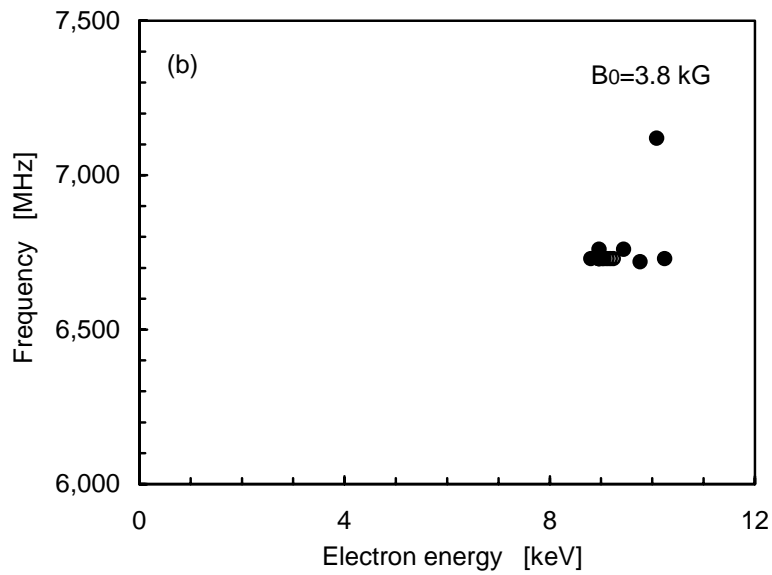
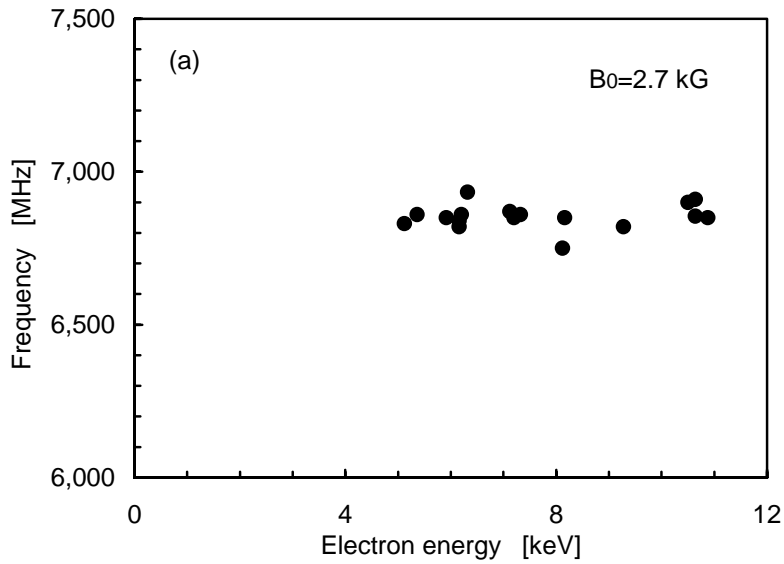


Fig. 2.25. Maps of frequency vs. electron-energy accumulated in many runs around (a) 2.7 kG and (b) 3.8 kG magnetic fields (each dot represents the average of a single run).

2.4. Analysis and Discussions

For the one-beam 2D CRM-array experiment, the agreement between the experimental results (Figs. 2.20a-d) and the theoretical tuning relation (Eq. 1.1 and Fig. 2.15) can be evaluated by a mismatch parameter proposed as follows

$$\Delta = \left[\frac{\beta_0(\omega)v_0}{\omega_c - \omega} \right]^2 - 1. \quad (2.3)$$

This parameter is computed using the measured experimental data (i.e., the wavenumber $\beta_0(\omega)$, the total electron velocity v_0 , and the cyclotron frequency ω_c are computed by the instantaneous *em* frequency, electron gun voltage and solenoid current, respectively). Eq. 1.1 and Eq. 2.3 teach that $\Delta \cong (v_{\perp}/v_z)^2$, where v_{\perp} is the initial electron transverse velocity. Hence, the expected value for Δ is in the order of one due to the actual v_{\perp} induced by the kicker (note that v_{\perp} is not measured in this experiment). Fig. 2.26 shows the results of Δ computed by Eq. 2.3 for the experimental runs presented in Figs. 2.20a-d, respectively. Negative values of Δ in Fig. 2.26 can be attributed to the error range of the solenoid field measurement ($\sim 2\%$), and to the high sensitivity of Eq. 2.3 to the cyclotron frequency (note that $\omega_c \sim \omega$). Nevertheless, a result of $-0.7 < \Delta < 1.9$ indicates a reasonable agreement between experiment and theory.

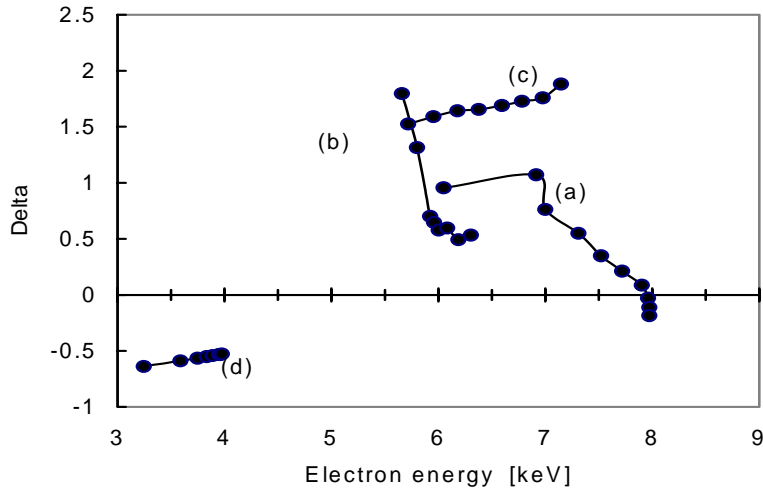


Fig. 2.26. The mismatch parameter Δ (Eq. 2.3). The curves denoted a-d correspond to the results in Figs. 2.20a-d, respectively.

The theoretical tuning condition of the CRM interaction (Eq. 1.1) and the Brillouin dispersion diagram of Fig. 2.15 are applied to analyze possible mechanisms for the resonant microwave radiation observed in the one- and two-beam 2D CRM-array experiments. The CRM tuning conditions observed in the one-beam 2D CRM-array experiment are illustrated in Fig. 2.27. The Brillouin diagram based on measurements shows the periodic-waveguide dispersion in the first and second passbands. The electron-beam lines are computed by Eq. 1.1 according to the experimental parameters for $B_0 = 2.7$ kG and 3.8 kG. The intersection points between the electron-beam lines and the waveguide dispersion curves indicate the *em* resonance frequencies. The results for the backward-wave interaction agree with the experimental results.

The synchronism conditions observed in the two-beam 2D CRM-array experiment are illustrated in Fig. 2.28. Again, the Brillouin diagram (based on measurements) shows the periodic-waveguide dispersion. The electron-beam lines are computed by Eq. 1.1 for 2.7 kG and 3.8 kG, and for electron energies of 6.5 keV and 10.2 keV, respectively. The intersection points between the electron-beam lines and the waveguide dispersion curves indicate the CRM resonance frequencies. One intersection point (at 2.7 kG) is in the fast-wave region, whereas the other (at 3.8 kG) is in the slow-wave region. Both interactions occur with backward waves. In the first 2D CRM experiment with the two electron beams, the CRM tuning results indicate clearly interactions with backward waves, and with fast and slow spatial harmonics of the periodic structure. The two-beam CRM interactions occur near the cutoff frequency of the first passband. The tuning condition for the fundamental harmonic interaction leads to a wide electron energy acceptance, as observed in this experiment (note the ~ 6 keV spread in Fig. 2.25a).

These experiments provide some information on the multi-beam CRM spectral character. However, the multi-beam CRMs, which consisted of multi-beam electron guns, resonator systems, focusing magnets and collectors, are highly sophisticated systems due to the non-uniformity of the RF distribution in the cavity and the transverse contribution of the focusing magnetic field. One of the most difficult tasks is to develop an electron gun, which produces the multi-beam streams.

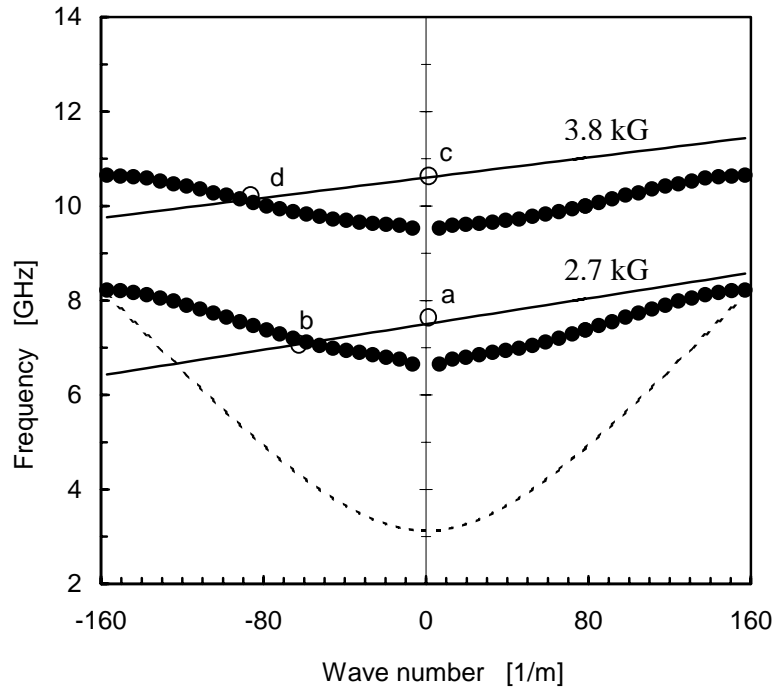


Fig. 2.27. The one-beam CRM tuning diagram. The upper two curves show the periodic-waveguide dispersion in the first and second passbands. The lines present the electron-beam lines as the results from Eq. 1.1. The dashed curve indicates the fundamental mode of the rectangular tube.

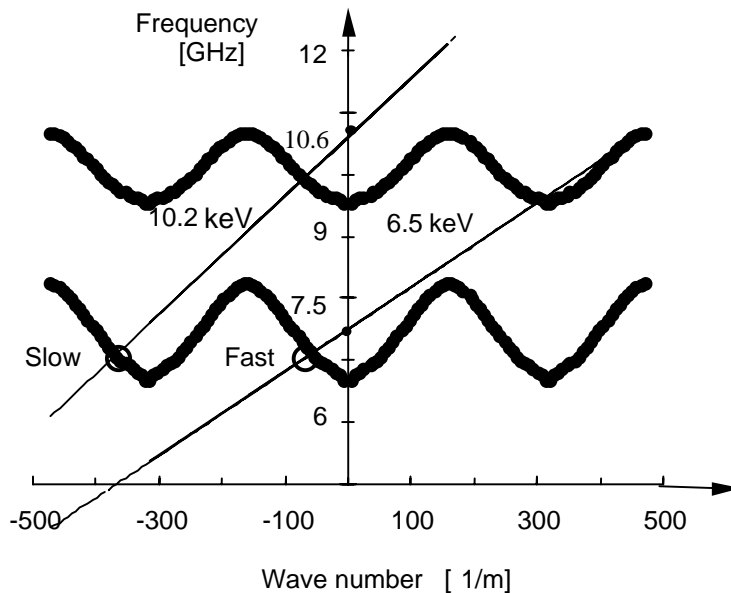


Fig. 2.28. A tuning-diagram presentation of Eq. 1.1 with the waveguide dispersion (Fig. 2.15), for the results of the two-beam CRM-array. The electron-beam lines, for 6.5 keV / 2.7 kG and 10.2 keV / 3.8 kG, show CRM interactions with fast and slow backward waves, respectively.

At present, we use the 2D simulation code, EGUN, commonly used in vacuum electronics, to design the multi-beam electron gun. However, these simulations do not obtain complete convergent results in the real systems, which lack 2D symmetry structures. The structure in the multi-beam electron gun is not the optimal focusing electrode, which arranges the uniform distribution of the current density in the multi-beam device. Some improvement in the design of the multi-beam electron gun is necessary in the future since it will affect average power. To achieve this goal, it is necessary to use advanced 3D modeling codes to design the components in multi-beam CRM devices.

2.5. Conclusions

The spectral measurements show clearly the CRM interaction with backward spatial harmonics. Both, fast- and slow-wave CRM interactions are observed in the two-beam CRM experiment. The results of the two-beam CRM experiment show the feasibility of splitting the electron current to separate beams in the array. The same approach leads to the construction of advanced CRM-array experiments in our laboratory (2D and 3D arrays of five (carbon-fiber) and nine (thermionic) cathodes, respectively). The next challenge is probably to improve the RF output power of the multi-beam CRM devices. The complexity of the multi-beam design requires the development of advanced software and equipment, such as power supplies. However, those problems can be remedied. Specially, when 3D modeling codes become mature, they certainly will accelerate the development of the devices that lack 2D symmetry and alleviate the design difficulties for multi-beam CRMs. The optimism in multi-beam CRMs is based on current developments on 3D modeling codes and the spectral measurements in this work.

Further studies proposed for the development of the multi-beam CRM-array concept [60] include (a) a radiation power extraction and efficiency measurements, (b) an investigation of coupling effects between several electron beams in a 2D array, (c) development of large 3D CRM-arrays, (d) studies of direct radiation from CRM arrays, and (e) active phased-array antenna features and radiation steering.

Chapter 3

The Carbon-Fiber CRM-Array Experiment

This chapter presents the first experimental study of a carbon-fiber CRM-array. The CRM-array is operated here with the multi-beam cold-cathode array, made of a carbon-fiber cathode array. According to our knowledge this is the first exploration of the multi-beam cold-cathode array and its application in vacuum electronics.

The next section, Section 3.1, describes the experimental design and setup of the carbon-fiber CRM-array. It includes the mechanical design of the device, a study of the multi-beam carbon-fiber cathode array, the design of the periodic waveguide and magnetic fields. In this part, the study of the multi-beam carbon-fiber cathode array is described intensively in the subsection 3.1.2. The fabrication of the carbon-fiber cathode is described first. Then, the experimental design and setup of the multi-beam carbon-fiber cathode array is presented. It includes the design of an electron-optic system of the multi-beam electron gun, a multi-channel pulsed power device, and an accelerating DC high voltage supply. The experimental results from the large area field emission “arrays” are given, and the general nature of voltage and current traces is presented. The effect of beam multiplication is discussed.

The operation of the carbon-fiber CRM experiment is described in Section 3.2. The experimental results and discussions are presented in Sections 3.3 and 3.4, respectively.

3.1. Experimental Design and Setup

A photograph of the carbon-fiber CRM-array experimental device is shown in Fig. 3.1. The oscillator tube consists of the electron gun with multi-beam carbon-fiber cathode array, a 2D periodic waveguide, a collector, a solenoid, and a kicker coil, which imparts initial transverse velocity to the electrons. The total length of the device is about 1.2 meter.

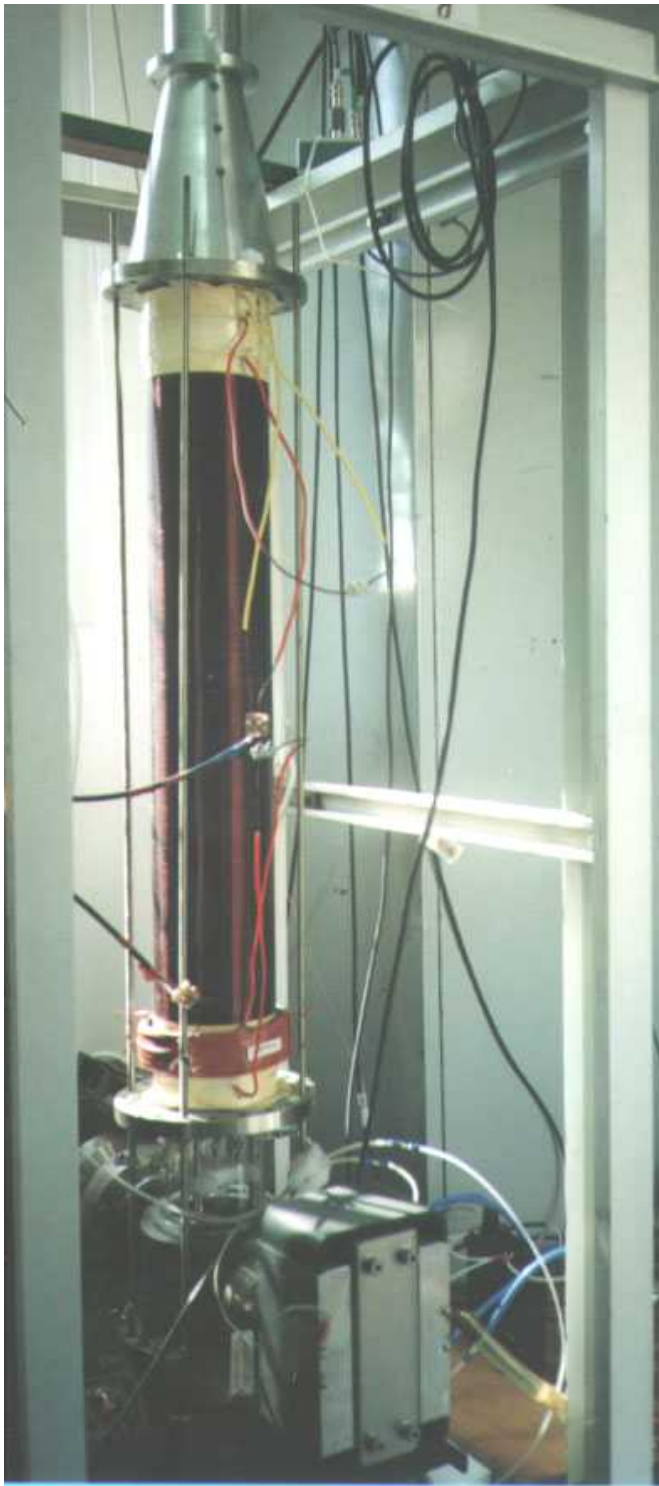


Fig. 3.1. Photograph of the carbon-fiber CRM-array experimental setup.

A schematic diagram of the carbon-fiber CRM-array experiment is shown in Fig. 3.2. The electron beams are emitted from the multi-beam carbon-fiber cathode array, which is driven by a multi-beam electron gun pulser. Then, the multiple electron beams, in energies of less than 10 keV, are spun up by the kicker, injected into the corresponding channels in the 2D periodic waveguide, and interact with the *em* wave. The *ignition* of each cathode causes an abrupt fall in its voltage, down to around 1 kV during emission. The solenoid field is compensated by Helmholtz coils and five blaster resistors act as current limiters. The accelerating voltage between the grid and the anode is provided by the DC high-voltage source. The beam currents are monitored by Rogowsky coils. The periodic waveguide is terminated by half-period reflecting sections at both ends.

The output signal is radiated from the exit plane of the waveguide to free-space, and is detected in the near-field by a horn antenna. The signal is attenuated and divided into two arms. In one arm, the signal is detected by a crystal detector (HP 424A) and recorded by a digital oscilloscope (Tektronix TDS 540). In the other arm, the signal passes a 4.7-5.3GHz bandpass filter (B.P.F.) in order to identify the frequency range of the RF signal. All data are collected by a computer using a HP VEE 3.0 (or Tektronix Wavestar) software. The experimental parameters are listed in Table 3.1.

Although the carbon-fiber cathode can work at pressure above 10^{-6} Torr, a better vacuum improves its operation. In this experiment, the tube is pumped down to a pressure around 10^{-6} Torr.

3.1.1. Mechanical Design

An overview of the apparatus of the carbon-fiber CRM-array experiment is shown in Fig. 3.3. A 1.4 m high frame is used to assemble the apparatus in vertical orientation. The main vacuum chamber consists of a stainless steel vessel and a glass tube. The vessel has a 6 inch diameter, one 4 inch hole at the top and two 4 inch flanges on the side. The side sections are attached to a Varian 20 litre/s triode pump (model 911-5030) and a Varian Turbo-V250 pump. The top hole is attached to the glass tube, which has 10 cm diameter and 1 m length. An O-ring is used between the two parts in order to protect the vacuum.

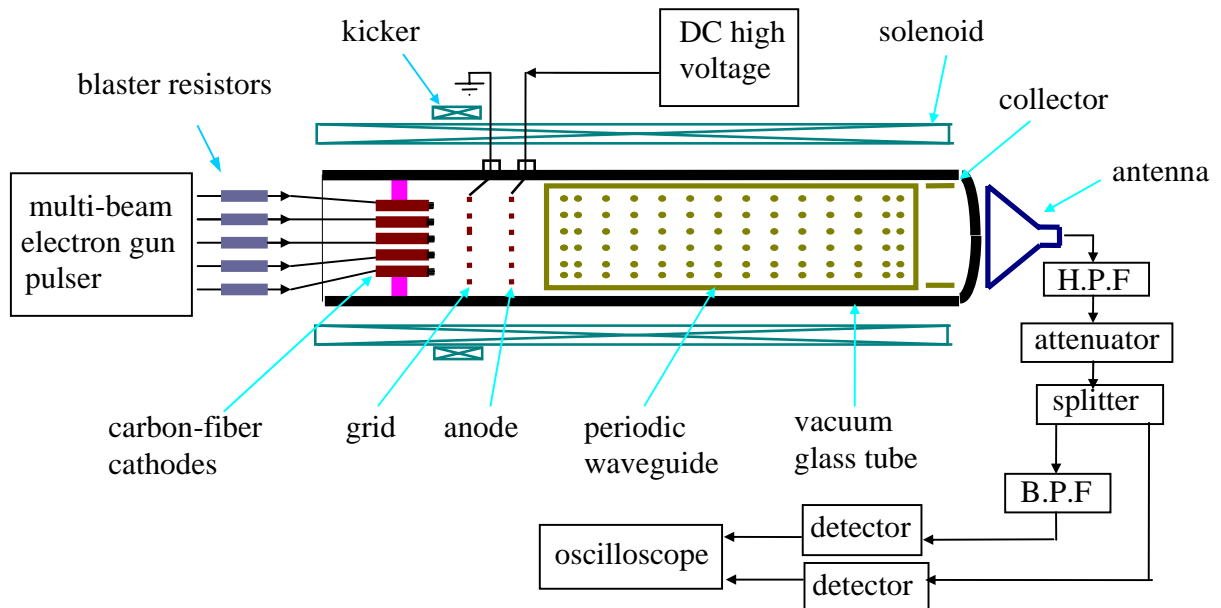


Fig. 3.2. Schematic of the carbon-fiber CRM-array experiment.

Table 3.1. Experimental parameters.

Electron beams:	
energy	~5 keV
current per beam	~ 0.1 A
pulse duration	0.4 ms
number of beams	3 or 5
Magnetic field:	
solenoid	~2.4 kG
kicker	~ 0.7 kA turns
Periodic waveguide:	
rectangular tube	$69 \times 22 \text{ mm}^2$
length	64 cm
post diameter	2 mm
post array	6×20
transverse periodicity	11.5 mm
axial periodicity	30 mm

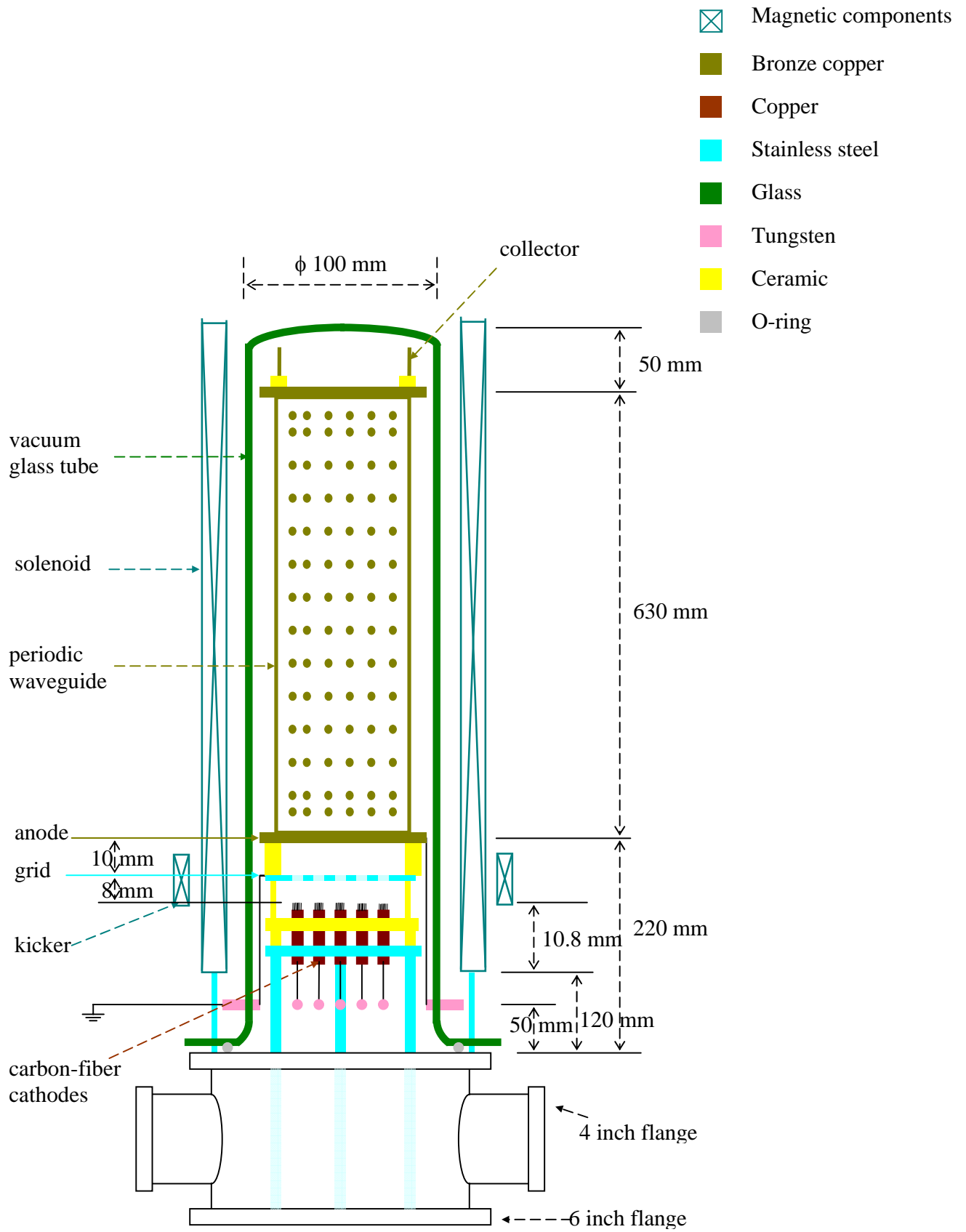


Fig. 3.3. Apparatus of the carbon-fiber CRM-array experiment.

The periodic waveguide is assembled inside the glass. A horn antenna outside the glass is coupled to the interaction region inside (note that unless the glass is $\lambda/2$ thick, or its mismatch can be matched at both surfaces, the near field antenna may distort the radiation pattern or lead to frequency sensitivity due to multiple internal reflections [113]). The stalk, supported the electron gun and the periodic waveguide, has a length of about 28 cm. It consists of several stainless steel posts and disks. Ceramic pieces are used for insulation. Eight Tungsten feedthroughs are hermetically sealed into the glass. The high voltages are connected through these feedthroughs. High voltage probes, Rogowsky coils, and pulsed power supplies are installed in an adjacent rack mount.

3.1.2. Multi-beam Carbon-fiber Cathode Arrays

Explosive electron emission cathodes for microwave applications offer the potential to provide high efficiency electron guns due to larger current densities and direct modulations of emitted beams. This research is motivated by the desire to develop efficient, reliable and cost-effective multi-beam cathode arrays for multi-beam vacuum electronic devices, such as multi-beam CRM-arrays and low voltage, long wavelength multi-beam FEL arrays. The primary objective for this stage is to make an effective five-beam carbon-fiber cathode array and explore the operation of multi-beam cold-cathode arrays in vacuum electronic devices.

3.1.2.1. Experimental Configuration

A schematic diagram of the multi-beam carbon-fiber cathode array experimental setup is shown in Fig. 3.4. The system consists of a multi-beam electron gun and a solenoid. The gun consists of two gaps. One gap is from five cathodes to a grid. This gap provides the electric field for the cathodes' emission. The other gap is from the grid to an anode. This gap provides an acceleration of the electrons in order to increase the energy of the electrons for CRM interaction. The construction of the first section is similar to the electron gun construction described in Section 2.1.1. The accelerating gap, which avoids the need for a high electric field in the first section, and delays the breakdown of the system, is powered with a DC high voltage supply. The five cathodes are made of bundles of carbon fibers. Each bundle contains hundreds of fibers in a copper pipe (~2

mm inner diameter). The diameter of each carbon fiber is less than 10 μm . The distance between two adjacent cathodes is 11.5 mm. The electrodes are placed inside a glass tube and are connected to the multi-channel electron gun pulser through the glass tube. The grid is located 8 mm ahead of the cathodes, and the distance between the grid and the anode is 10 mm. Both the grid and the anode are connected to Tungsten feedthroughs, which are hermetically sealed into the glass. The grid is connected to a ground potential outside and the anode is connected to a DC high voltage supply, which can provide up to 20 kV DC voltage.

The electron beams are emitted from the carbon-fiber cathodes, propagate in the two sections, and are collected by a metal plate. The collected current is measured by means of a 10 Ω resistor. The device is activated by a multi-channel electron gun pulser, a high voltage DC power supply, and a solenoid pulser. A Rogowsky coil (1:10 V/A) is used to monitor the output current from the electron gun pulser. Five blaster resistors, ~ 10 k Ω CuSO_4 water resistors, are connected to the five cathodes in series separately and act as current limiters. High resistivity enables more tips to emit, and the magnitude of the emission from each cathode is more uniform. The emitter voltage, which is the potential between the cathodes and the grid, and the DC high voltage are monitored by two high voltage probes (Tektronix P6015A, 1:1000). All data are recorded by several digital oscilloscopes (Tektronix TDS 210), and collected in a computer by a Tektronix Wavestar software through GPIB cables. All cathodes testing are carried out with a base pressure around 10^{-6} Torr, with and without an external magnetic field.

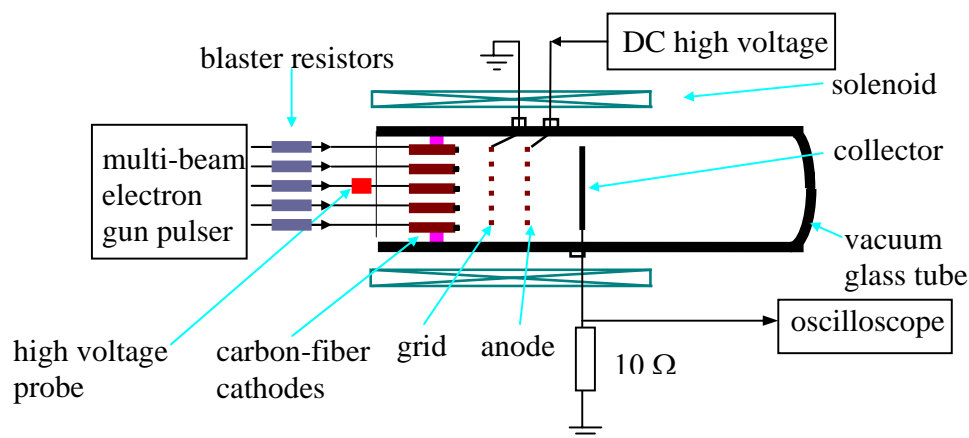


Fig. 3.4. Schematic of the multi-beam carbon-fiber cathode array experiment.

3.1.2.2. Cathode Fabrications

The schematic of the carbon-fiber cathode is shown in Fig. 3.5. In Fig. 3.5a, the cathode consists of 10 μm bunches of fibers and a copper tube. During fabrication, a bundle of carbon fibers, contained hundreds of fibers, was trimmed (but not etched) and inserted by hands in the copper tube. The tube was mechanically pressed at the end in order to tighten the fiber bundle and to provide a proper electrical contact. An advanced scheme is shown in Fig. 3.5b. Comparing to the scheme in Fig. 3.5a, the cathode adds an electrical field shield around the tips of the carbon fibers. It improves the electrical field distribution for the cathodes' emission. When a voltage is applied to the tube, the electric field created at the tips is magnified due to the extreme sharpness of the tips, which causes electron emissions. In many cases an electric field as low as 3 kV/cm is sufficient to produce plasma formation for electron emissions. A photograph of the cathodes is shown in Fig. 3.6.

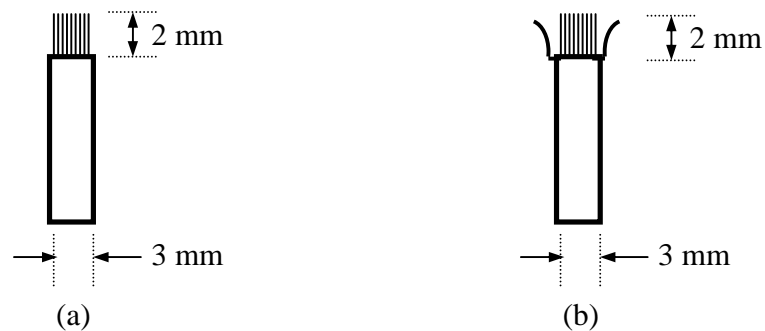


Fig. 3.5. Schematic of a bunched carbon-fiber cathode (a) and an advanced scheme (b).



Fig. 3.6. Examples of the end brush cathodes.

3.1.2.3. Electron Trajectories

The electron optics design of the multi-beam electron gun is performed with the EGUN code with a few assumptions. As in Section 2.1.1, we assumed that each beam has a perfect local symmetry around its own axis and the gap between cathode and grid (or grid and anode) is much smaller than the distance between two holes of the grid plate (or the anode plate). So simulating the center electron flow and simplifying the boundary, the code output for a 3mm carbon-fiber cathode with 8 mm cathode-grid gap and 10 mm accelerating section is shown in Fig. 3.7. Fig. 3.7a shows electron gun geometry and beam trajectory. It includes three regions: a cathode-grid region, a grid-anode region, and a beam tunnel. Fig. 3.7b and Fig. 3.7c present electron density versus radius and the angle of the electron motion measured from the z -axis, respectively. A magnetic field is used for the beam focusing.

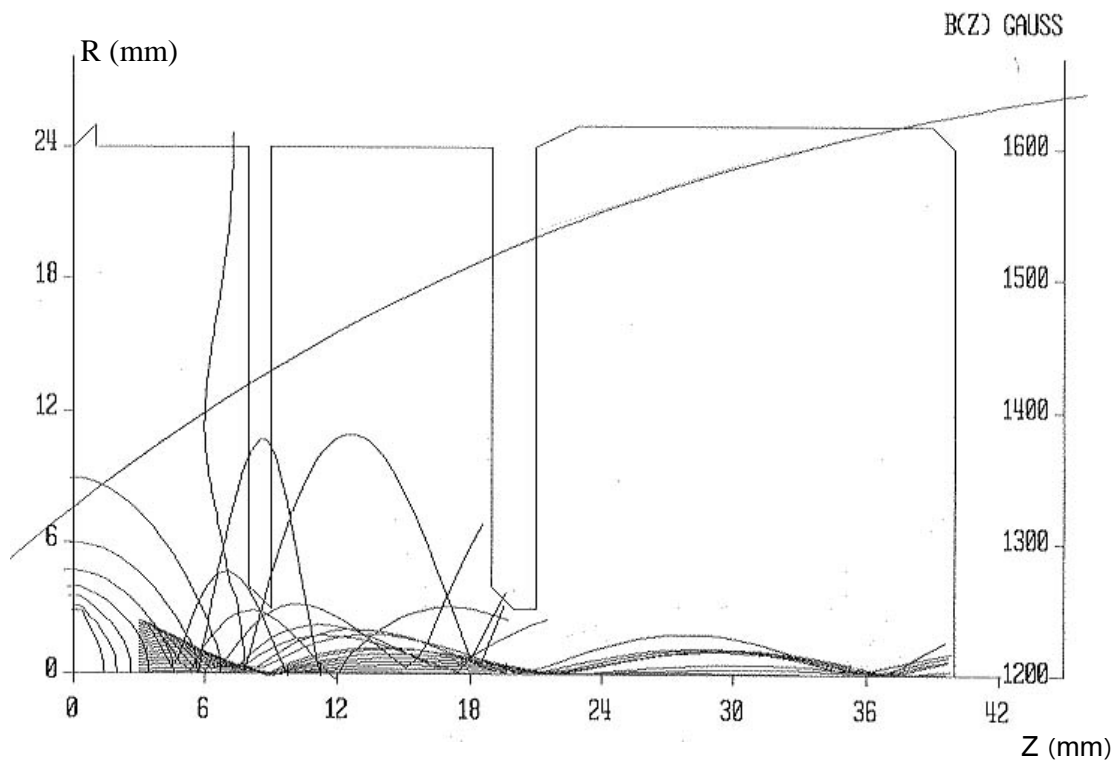


Fig. 3.7. The EGUN code output for a 3mm carbon-fiber cathode, (a) the beam trajectory (radius (R) vs. axial length (Z)).

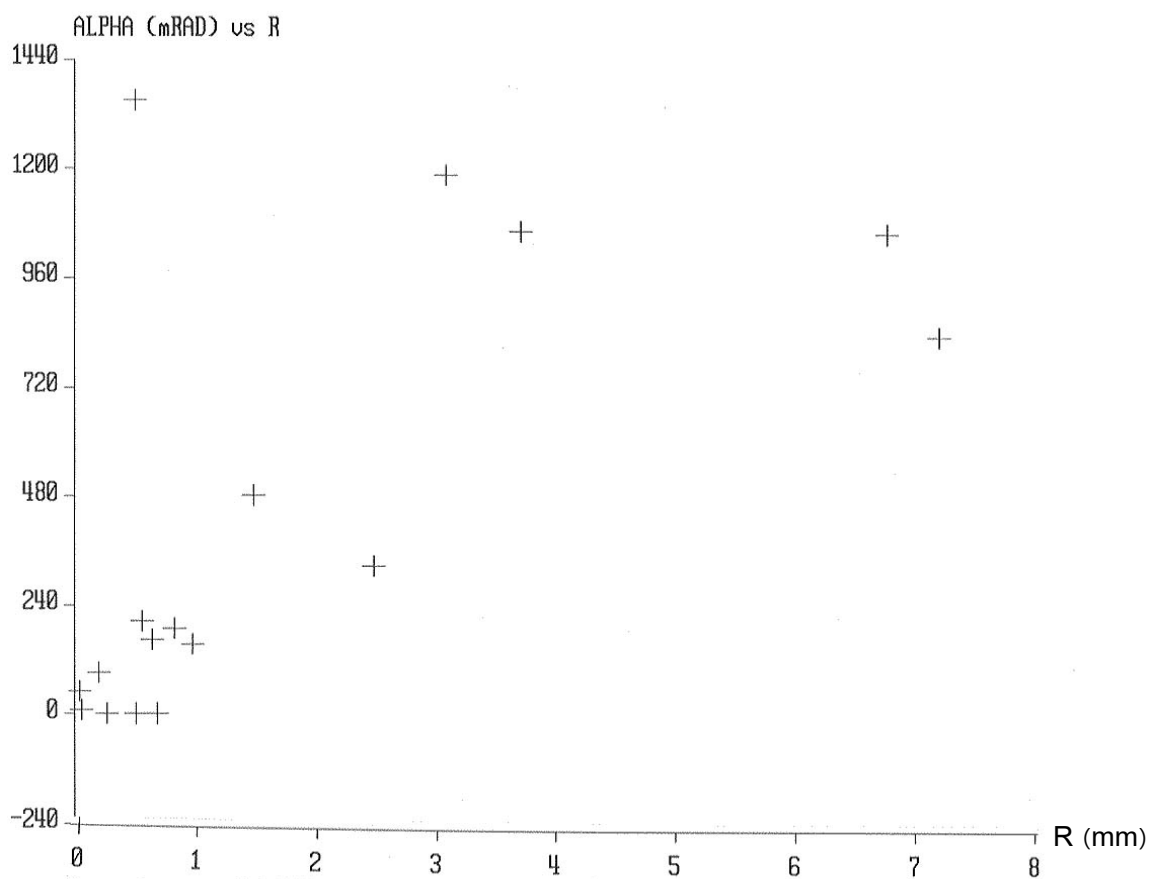
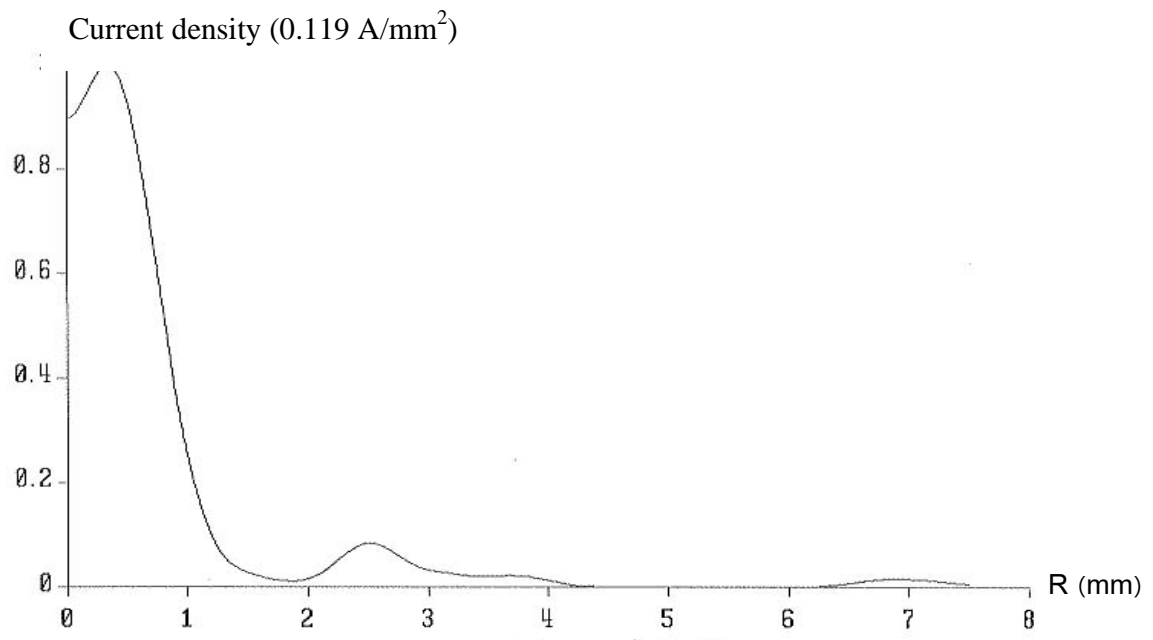


Fig. 3.7. (Cont.) The EGUN code output for a 3mm carbon-fiber cathode, (b) electron density vs. radius, (c) the angle of the electron motion measured from the z axis.

3.1.2.4. Power Supplies

Three incorporating high voltage supplies for the multi-beam electron gun, accelerating section, and solenoid were used in the experiment of the carbon-fiber cathode array. The solenoid pulser is the same as described in Section 2.1.3. However, the multi channel electron gun pulser was redesigned in order to ensure the uniform current density of the multi-cathode array. Meanwhile, the DC high voltage was used for the accelerating gap. The design details are described in the section below.

The multi-channel pulsed power system produces five separating pulses with fairly high voltages and output currents. The circuit is shown in Appendix B3. The pulser is fed by 220 V AC through a variable voltage transformer and a 10 A fuse. Then, this AC voltage is connected to a 220/460 V up-shift transformer. The output of the transformer is fed to five-channel charging circuits. Each channel consists of a low-voltage capacitor bank (C), a diode IN5408 that prevents a reverse recharging of the capacitor, and a transformer (car ignition coil). The charging voltage is monitored by a TY-43 digital panel meter. An SCR control circuit is used as a common gate. The five capacitors, about 10 μ F each, are charged with a rectified main voltage (600V), and then are discharged in an instant through the SCR and the ignition coils. The SCR is triggered by a function generator.

The DC high voltage supply for the acceleration section was done in two schemes. Both of them used a modified Model 615 Pulserad power supply. The original Model 615 Pulserad and our modifications are described in Appendix C. The circuits for both schemes are shown in Fig. 3.8 and Fig. 3.9, respectively. In Scheme 1, a long pulse is used to supply the accelerating stage. Compared to the electron gun voltage pulse, the duration of the pulse is much longer and it acts as a DC high voltage. A timing diagram in scheme 1 is shown in Fig. 3.10. In Scheme 2, the DC high voltage is coming directly from a charged capacitor bank in the modified Model 615 Pulserad. For safety, the capacitors are discharged after the shot of the electron gun. A corresponding timing diagram is shown in Fig. 3.11.

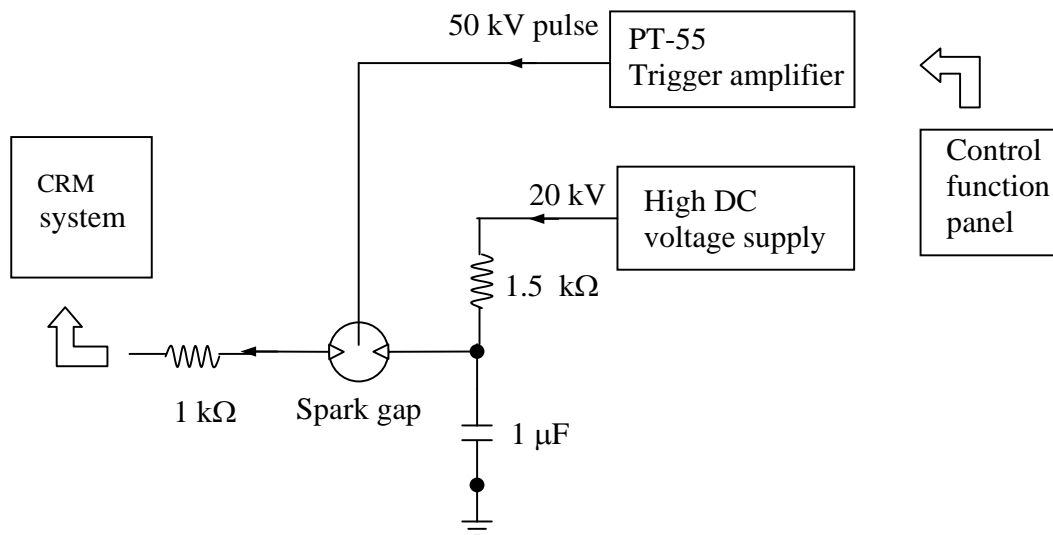


Fig. 3.8. Circuit of an accelerating voltage source.

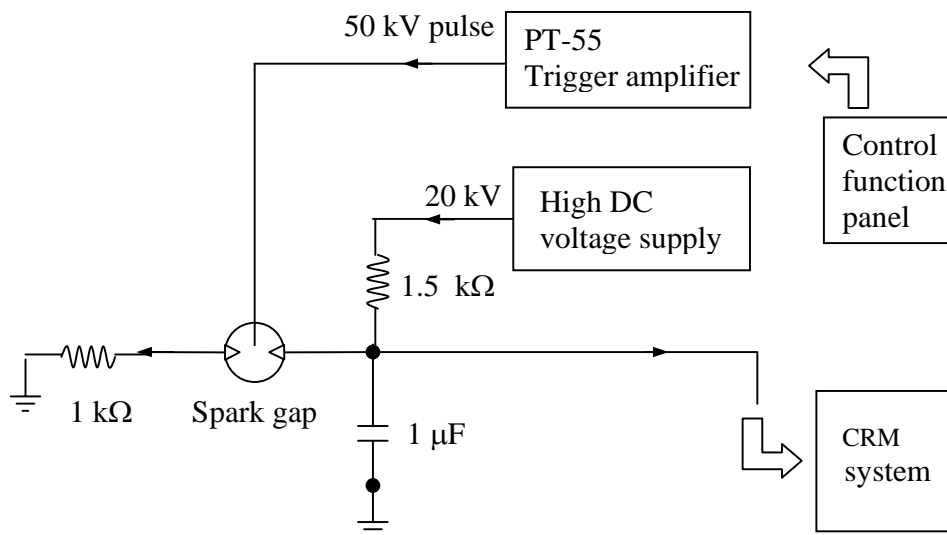


Fig. 3.9. Circuit of a DC high voltage source.

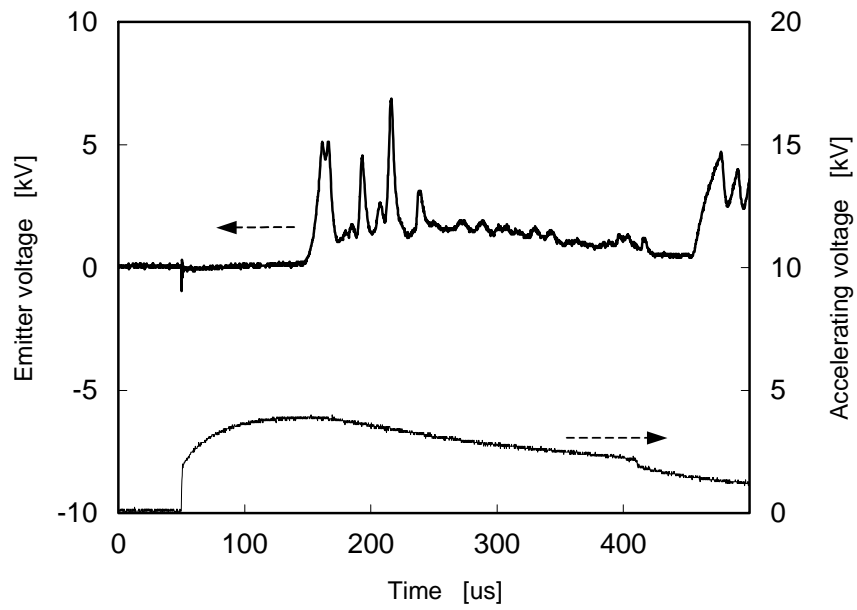


Fig. 3.10. A timing diagram in Scheme 1.

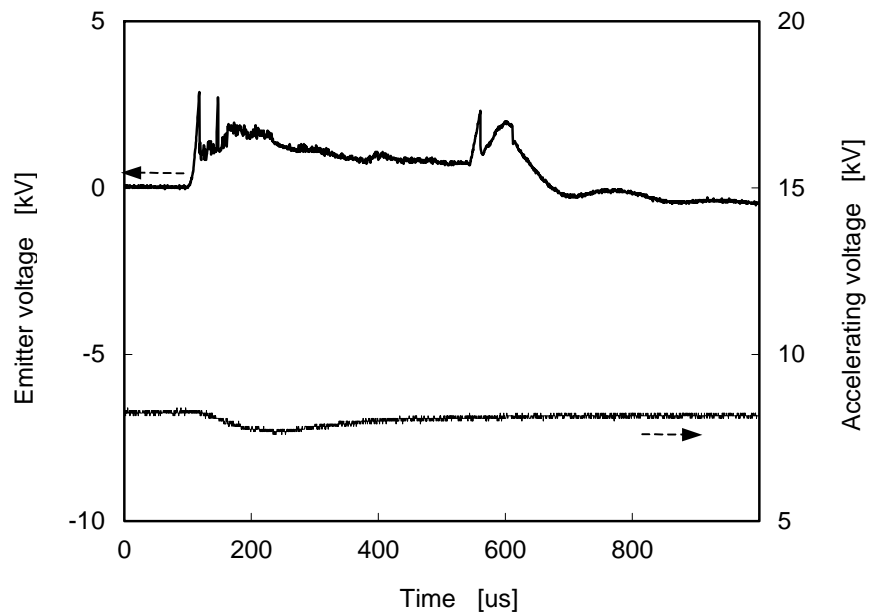


Fig. 3.11. A timing diagram in Scheme 2.

3.1.2.5. Electrical Performance

The electron gun, which has one carbon-fiber cathode, was tested initially at a diode voltage of more than 4 kV (without accelerating voltage) with an 8 mm gap between the cathode and the grid. A ~100 mA diode current was observed. Then, increasing the number of the cathodes to three and five, the electron gun was tested in the same condition. Typical emitter voltage (or diode voltage) and current traces for a shot with the electron gun, which has five carbon-fiber cathodes, are illustrated in Fig. 3.12 (without an additional accelerating voltage). In this shot, the multi-channel gun pulser was adjusted to provide a more than 3 kV/cm electric field for each cathode. In Fig. 3.12, the emitter voltage rises rapidly (~2kV) during the first few microseconds. Then, the voltage drops sharply to ~500 V due to the impedance changing as the current turns on. After about 450 μ s there is a breakdown between the cathodes and the grid. This attributes to the property of explosive field-emission cathodes. Then the closure speed is about 1.8 cm/ms. The collector current was measured by a 10 Ω resistor placed between the collector and ground. A ~0.5 A current (total) was measured at the collector, that is about 0.1 A for each channel. The current density is around 1.4 A/cm² (7 A/cm² in the cathode-grid gap since we monitored the ~0.5 A input current for each cathode). Therefore, a long duration pulse dictates a low current density. The relative long rise time of the high voltage pulse caused the carbon fibers flare on a critical voltage. This may explain the long duration pulse with a low current density, relative to other one-beam cold-cathode researches. Adding an accelerating voltage, typical emitter voltage and current traces for a shot with five carbon-fiber cathodes are illustrated in Fig. 3.13. The pulse duration of the emitter voltage for a one channel is not significantly changed. So it seems that the accelerating voltage did not change the closure speed in the cathode-grid gap.

Several shots were made with the modified Marx generator. In these experiments, the modified Marx generator connected directly with the five carbon-fiber cathodes. However, the emission was ceased in a very short time. Besides this limitation, the five cathodes could not be fired at the same time using the modified Marx generator, due to the non-uniformity of the cathode array. Therefore a special multi-beam pulse generator was built for the multi-beam carbon-fiber CRM array.

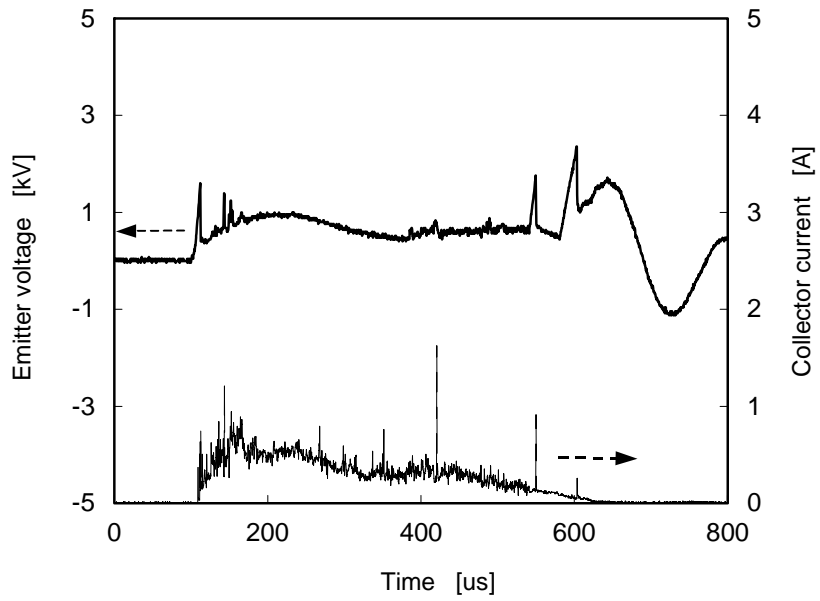


Fig. 3.12. A typical cathode voltage and current traces without an accelerating voltage.

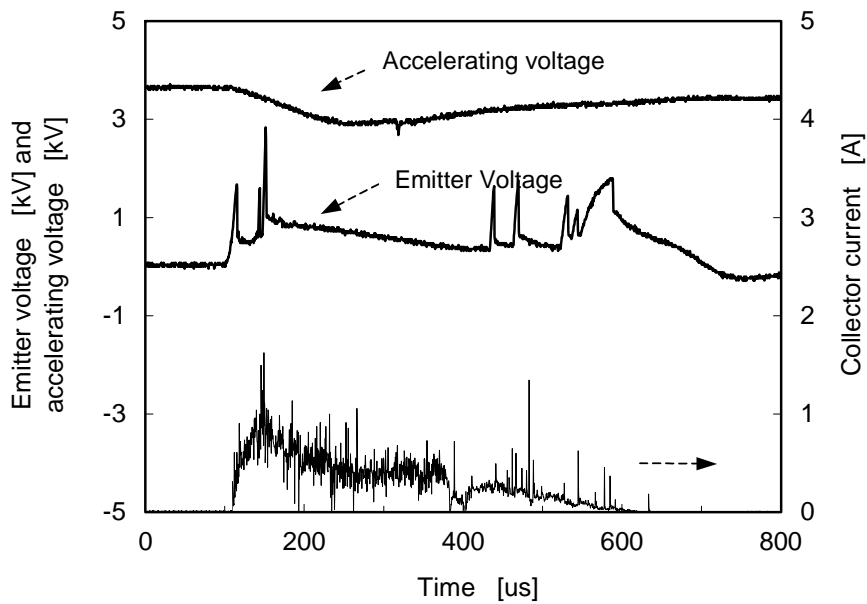


Fig. 3.13. A typical cathode voltage and current traces with an accelerating voltage.

A series of measurements were made with the different number of the cathodes in similar condition. The influence of the number of beams on the breakdown of the system was checked. A typical experimental result of the electron gun with a single cathode is shown in Fig. 3.14. Figs. 3.14 a, b, c, and d represent the emitter voltage for a one channel, the accelerating voltage, the current at the collector, and the current at the accelerating gap, respectively. The corresponding experimental measurement of the electron gun with the five-beam cathode array is shown in Fig. 3.15. In this case, the appearance of a breakdown at the accelerating stage depends on the array density. The diode voltage for each channel in the experiment of the five-beam cathode array is similar to the voltage in the experiment of the one-beam cathode array. In a similar diode voltage for each cathode, when the number of cathodes increases, the effective accelerating voltage, which does not cause the breakdown of the system, becomes lower (~ 7 kV in Fig. 3.14b and ~ 3 kV in Fig. 3.15b, i.e. ~ 4 kV difference). Decreasing the input energy for each cathode, Fig. 3.16 and Fig. 3.17 show the observed results for the electron gun with one-beam and three-beam cathode array, respectively. Again, when the number of cathodes increases, the effective accelerating voltage becomes lower (~ 11 kV in Fig. 3.16b and Fig. 3.17b without and with breakdown, respectively). But here the difference is much smaller, perhaps because the distance between two cathodes in the three-beam array is two times wider than the distance in the five-beam array. Comparing Fig. 3.14 and Fig. 3.16, we also found that the effective accelerating voltage decreases when the diode-input energy increases in the same number of beams (7 kV in Fig. 3.14b and 11 kV in Fig. 3.16b). Therefore, the effective accelerating voltage is inversely proportional to the current density. In our configuration, the effective accelerating voltage for the electron gun with the three-cathode array is more than 7 kV; whereas, for the electron gun with the five-cathode array, the effective accelerating voltage is much smaller, around 3 kV. These tests are important because this is the first exploration of electron guns with multi-beam cold cathodes. It demonstrates that the ~ 400 μs multi-pulse with ~ 0.1 A for each channel can be produced with this configuration. We found that in similar diode voltage for each cathode, when the number of cathodes is increased, a lower effective accelerating voltage can be achieved, and the achieved effective accelerating voltage is decreased when the diode-input energy is increased in the same number of the beams.

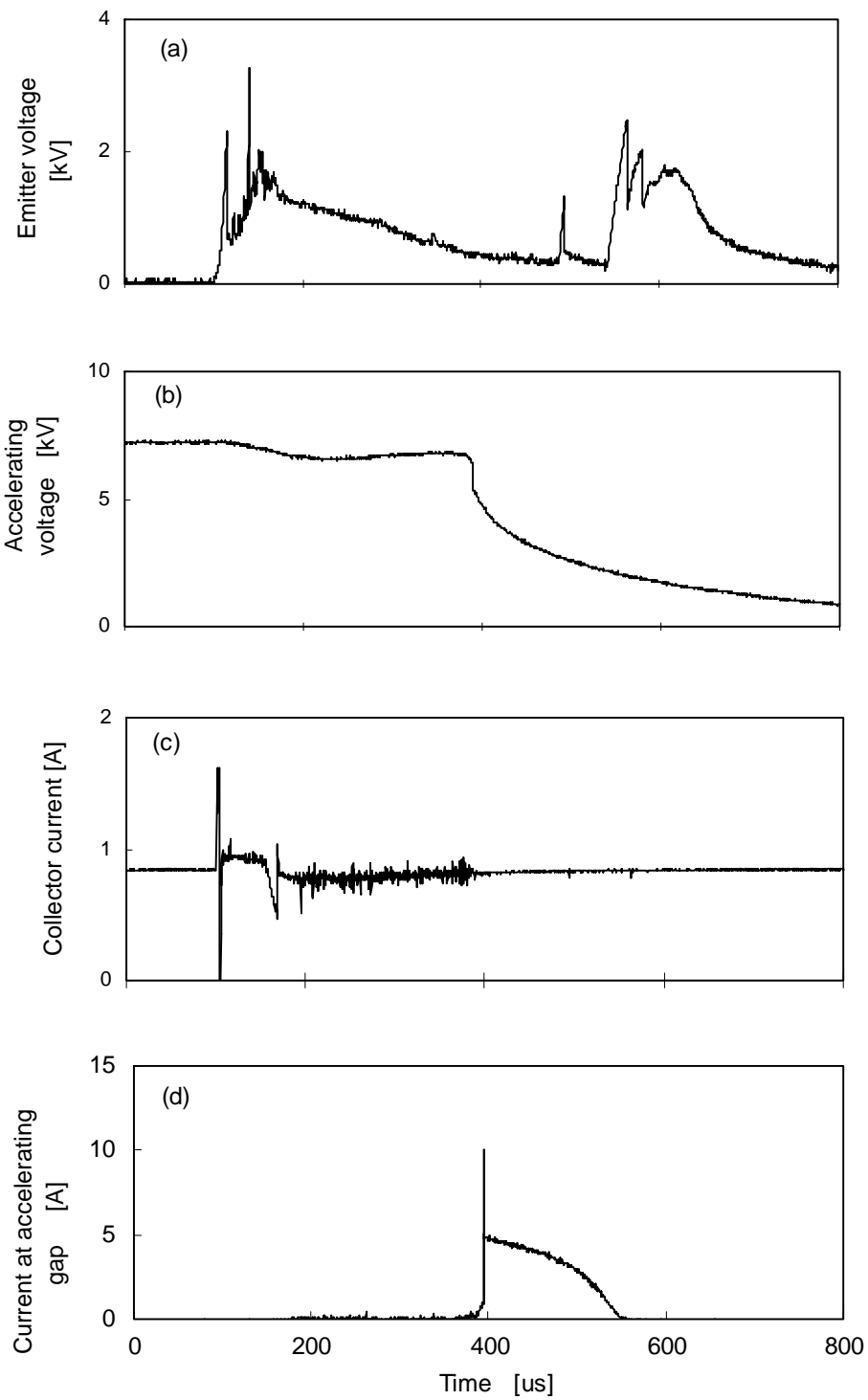


Fig. 3.14. An experimental measurements for a single cathode gun:
(a) the emitter voltage, (b) the accelerating voltage,
(c) the collector current, and (d) the current at the accelerating stage.

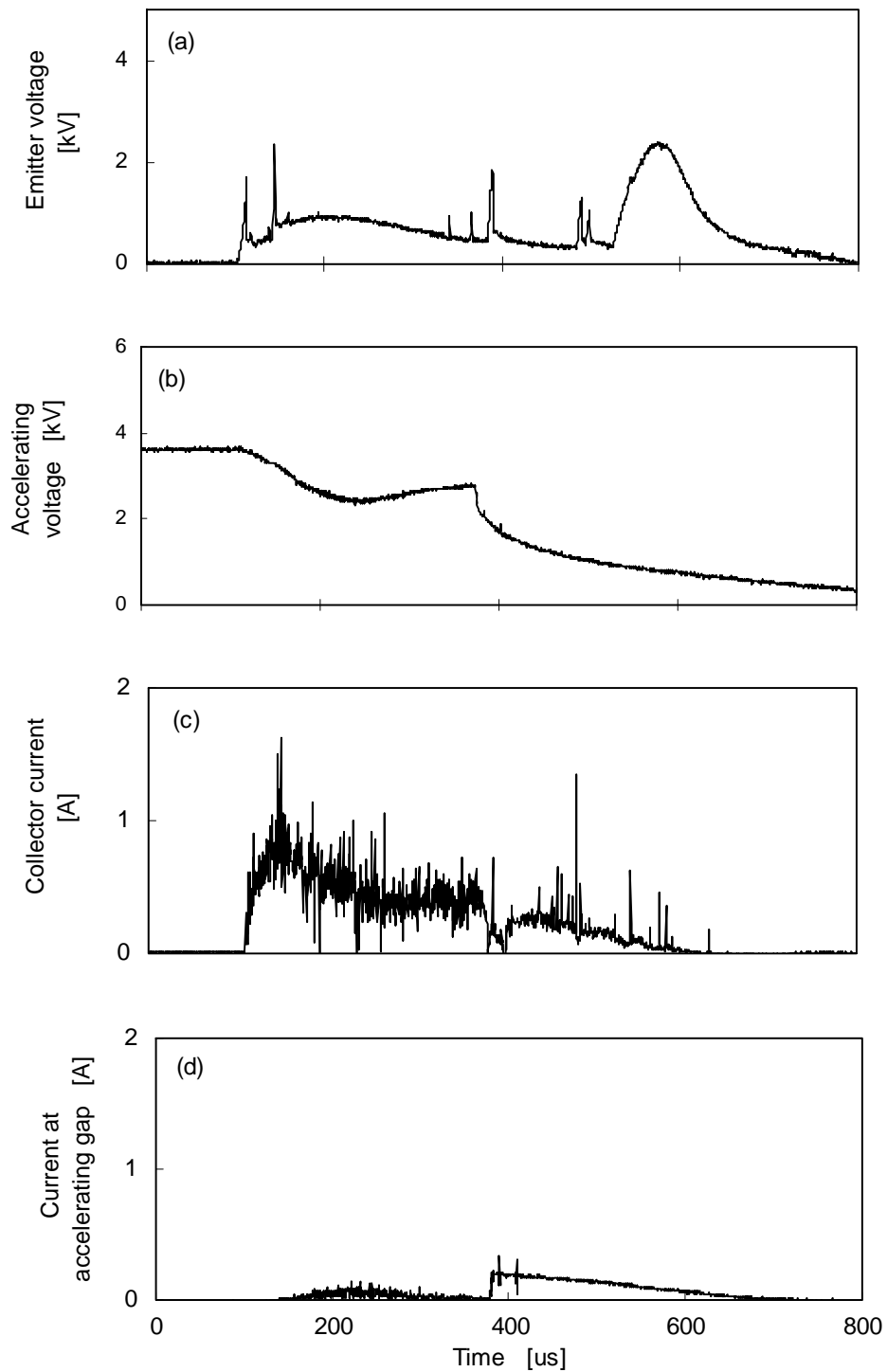


Fig. 3.15. An experimental measurements for a five-cathode gun:
 (a) the emitter voltage, (b) the accelerating voltage,
 (c) the collector current, and (d) the current at the accelerating stage.

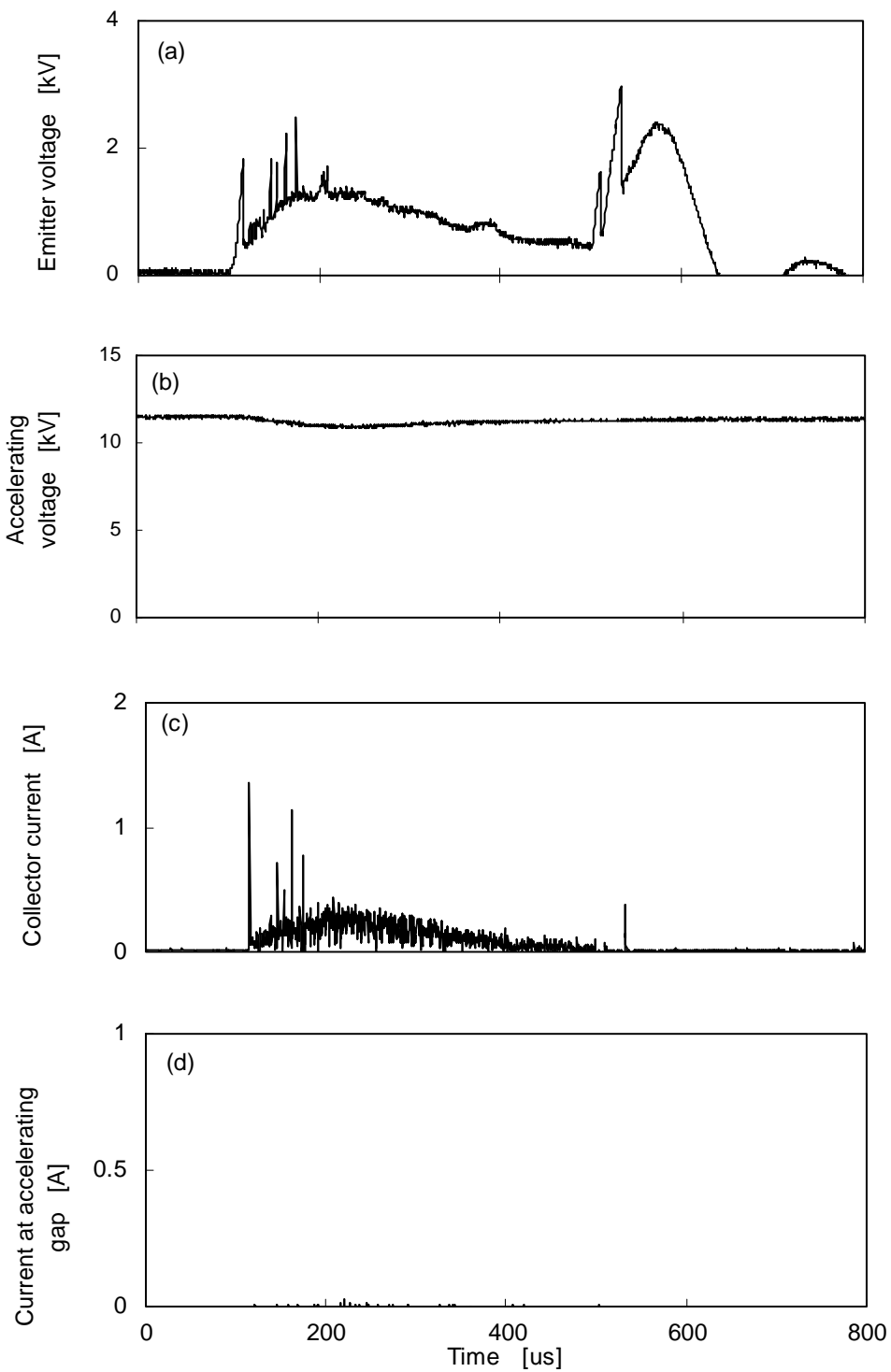


Fig. 3.16. An experimental measurements for a single cathode gun with a decreased input voltage:
 (a) the emitter voltage, (b) the accelerating voltage,
 (c) the collector current, and (d) the current at the accelerating stage.

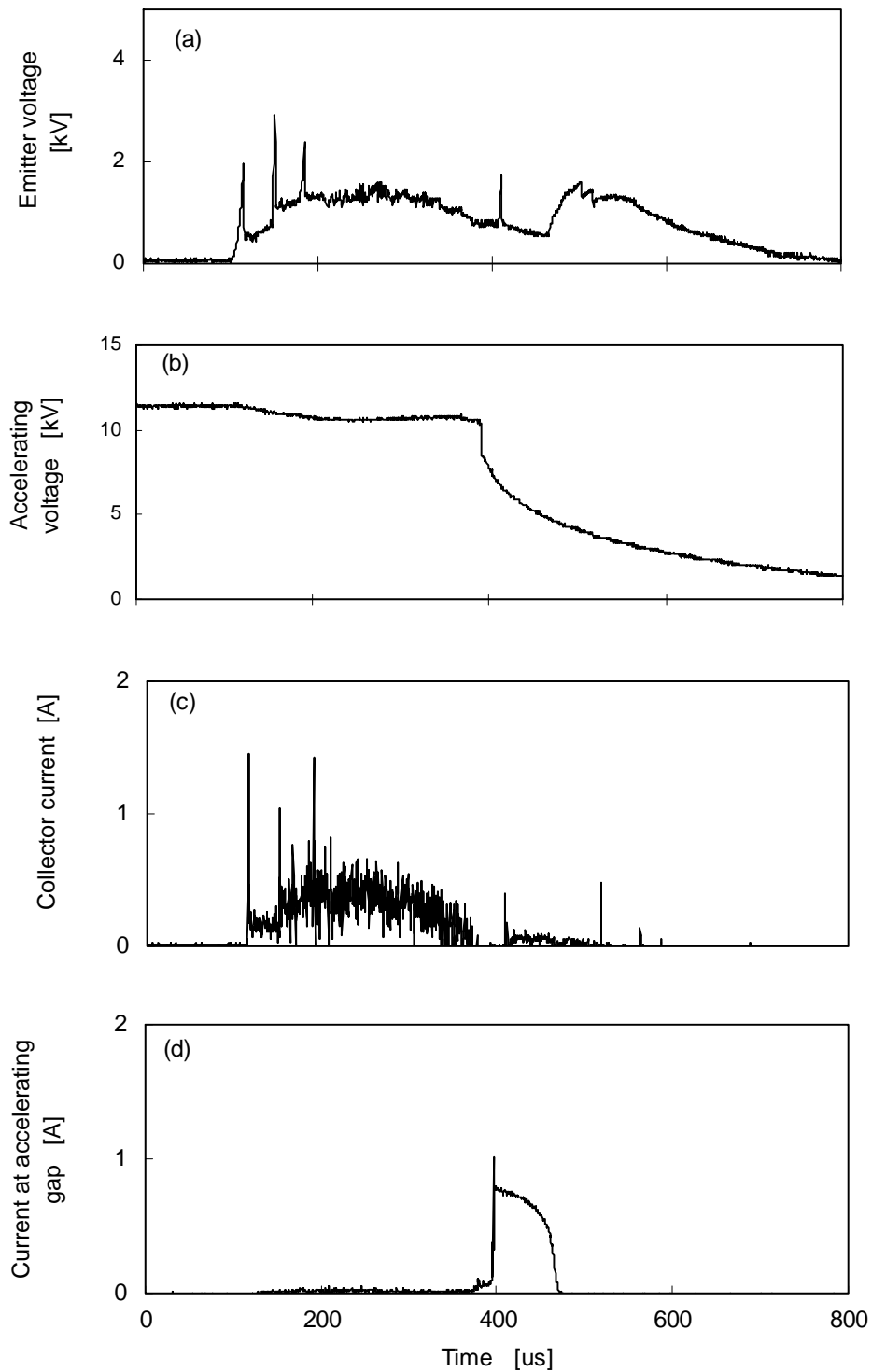


Fig. 3.17. An experimental measurements for a three-cathode gun:
(a) the emitter voltage, (b) the accelerating voltage,
(c) the collector current, and (d) the current at the accelerating stage.

3.1.3. Magnetic Fields

One of the major concerns about the multi-beam carbon-fiber CRM-array is the non-uniformity of the transverse contributions of the focusing magnetic field. A careful design of the solenoid was made to incorporate one main coil and two side coils. In this solenoid, the side coils were used to improve the uniformity near the edge of the magnetic field. Fig. 3.18 shows the cross section of the solenoid. The main coil was made out of a 2 mm diameter copper wire with 9.8 turns/cm. The two side coils were made out of a 2 mm diameter copper wire with 5 turns/cm. A large diameter kicker was designed in order to spin up the electrons. It was made out of a 1 mm diameter copper wire with 32 loops/cm. The final design of the kicker can be made in two ways. One method is to insert an array of thin, trim coils in the vacuum chamber, in order to produce the uniformity of transverse fields for each beam. The second method concerns the electrostatic effect. That means using the electrode structure to change the electrostatic field around cathodes. In the final off-axis design it may have a small difference in the electric field on the two sides of the electron beams. This could be designed by purposely inserting an asymmetric metal piece.

The axial magnetic field at any point of the solenoid is calculated by Eq. 2.1. The result of the computer simulation is given in Fig. 3.19. In Fig. 3.19, the magnetic field of the main coil is shown by the dash-dot curve, the magnetic fields of the side coils are shown by the two small dashed curves, and the magnetic field of the solenoid is shown by the solid curve. The star sign represents the front position of the cathodes. In principle, the off-axis magnetic field of the solenoid can be calculated using the formulas or special software. In the experiment, a Gauss meter was used to check the magnetic field uniformity near the edge of the solenoid [114]. The parameters of the solenoid and the kicker are shown in Table 3.2.

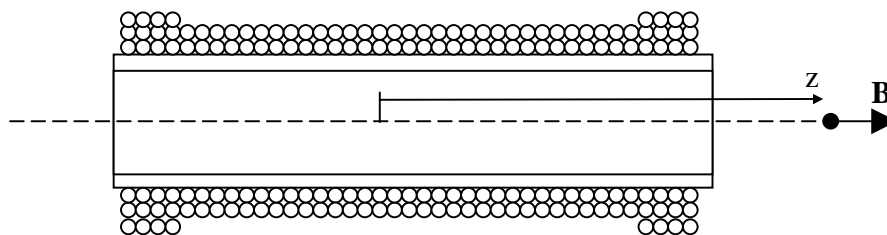


Fig. 3.18. Solenoid in cross section.

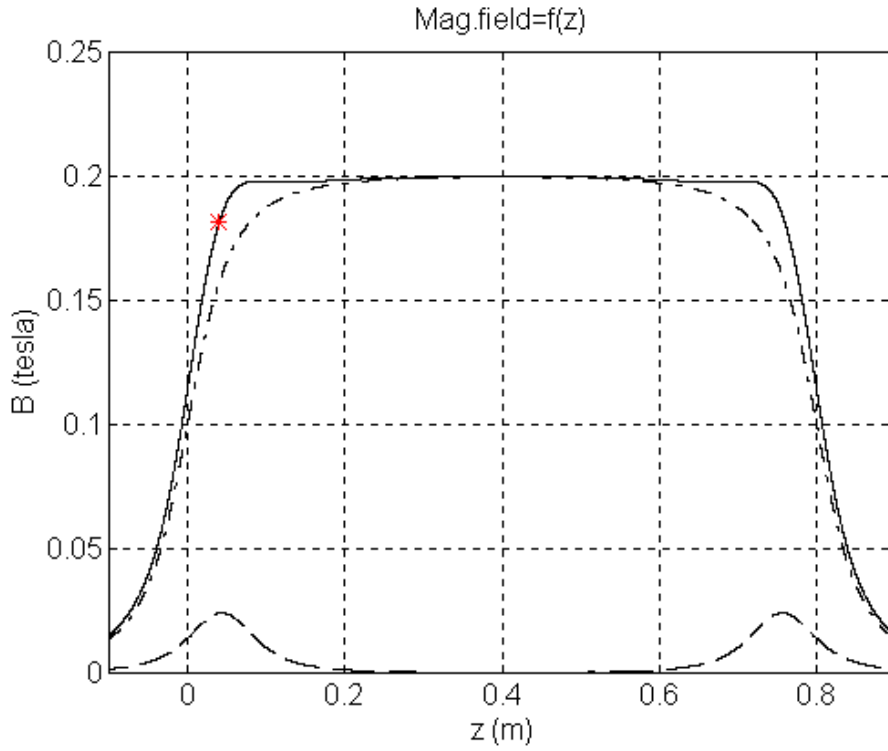


Fig. 3.19. The magnetic field of the solenoid.

Table 3.2. The parameters of the solenoid and the kicker.

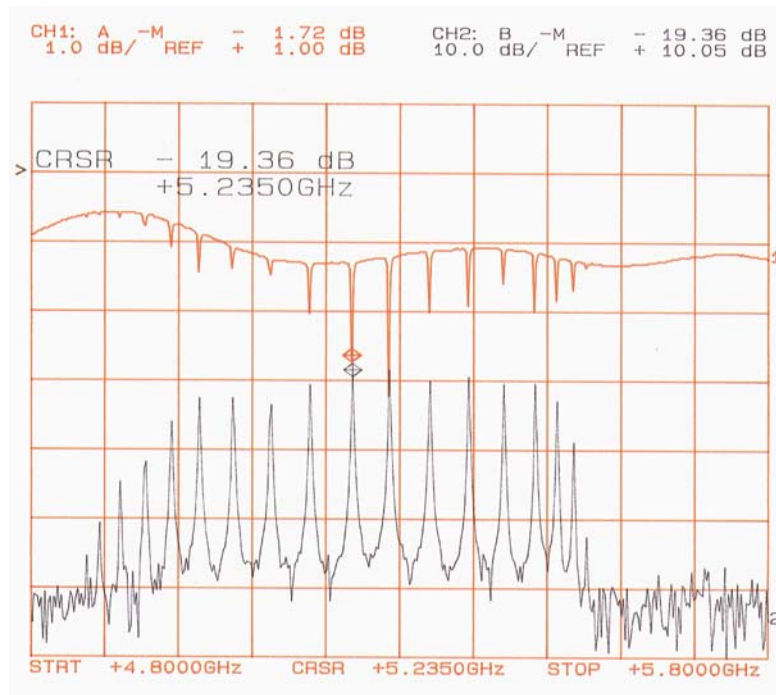
Parameter	Main coil	Side coil	Kicker
Turns	780	15	98
Current [A]	100-200	100-200	20-140
Inner radius [cm]	5.7	6.1	7
Outer radius [cm]	6.1	6.3	7.4
Length [cm]	80	3	3.5

3.1.4. The Periodic Waveguide

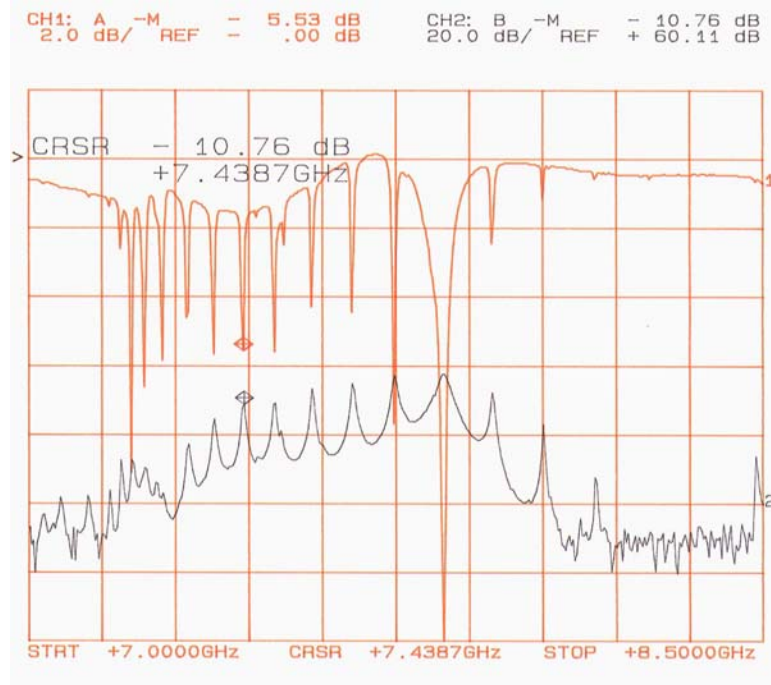
A photograph of the periodic waveguide is shown in Fig. 3.20. The waveguide consists of a metal-post array with 6x20 elements and is terminated by half-period reflecting sections in both ends. Figs. 3.21a and b show the measured resonant absorption and transmission peaks corresponding to the axial modes of the cavity at the first and second passbands, respectively. The resonances were measured by looking at the reflection coefficient (upper traces in Fig. 3.21 a, b) of the slow wave structure over the appropriate frequency range, as described in Section 2.1.4. The waveguide dispersion is shown in a Brillouin diagram in Fig. 3.22, as results from the measurements of the waveguide reflection and transmission coefficients. These intersections are shown by the dots in Fig. 3.22. The electron beam line is added to Fig. 3.22 in order to demonstrate CRM interaction in the first passband. The point a, which is the intersection of the electron beam line and the waveguide dispersion curves, indicates a possible CRM interaction with backward wave. Forward and backward wave interactions ($\beta_n > 0$ and $\beta_n < 0$, respectively) differ by the tendency of the latter to act as absolute instabilities, and to oscillate (as observed in this experiment). The backward wave interaction could be the desired mode for a CRM-array oscillator. In amplifier schemes, however, parasite backward-wave interactions can be eliminated by a proper tuning to a tangential (grazing) point in Fig. 3.22.



Fig. 3.20. Photograph of the periodic waveguide.



(a)



(b)

Fig. 3.21. The measured reflection and transmission curves at the first passband (a) and the second passband (b).

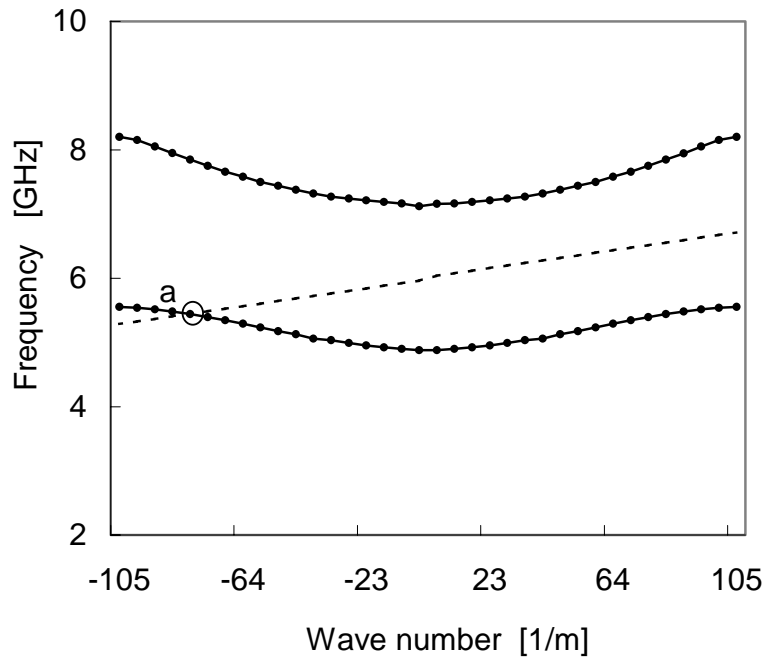


Fig. 3.22. The measured Brillouin diagram of the 2D periodic waveguide. The dashed line represents Eq. 1.1 in a cyclotron frequency at 6 GHz.

3.2. Experimental Operation

Each experiment began with a pre-running period to activate the cathodes. We found the following break-in procedure is useful. First, the cathode is under vacuum for several hours before firing them. Then, the operation is begun at the minimum voltage required to initiate the emission. After few tens of shots, the change of the gas pressure caused by the cathode emissions should be reduced, compared with the first shots. Meanwhile, the accelerating voltage is increased in gradual until the desired voltage is achieved. In order to reduce the surface contamination, to stabilize the pressure and field emission currents, it is necessary to wait enough time between two shots.

A control trigger system was used with function generators. The system connection is shown in Fig. 3.23. The main trigger comes from the solenoid pulser. Then it is sent to three function generators. After some delay, three trigger signals come out from the function generators and are sent to the gun pulser, kicker pulser and the 615 MR Pulserad control panel.

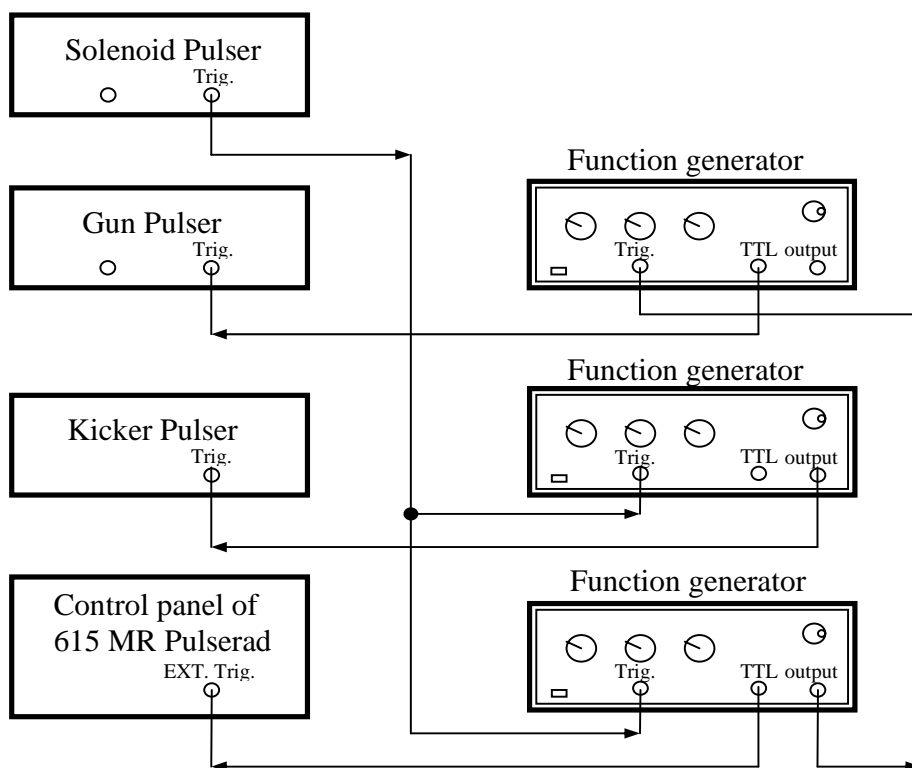


Fig. 3.23. The trigger system.

3.3. Experimental Results

A typical experimental result of the three-beam carbon-fiber CRM-array is shown in Fig. 3.24. The emitter voltage of the center carbon-fiber cathode is shown in Fig. 3.24a. The accelerating voltage is shown in Fig. 3.24b. The cathode input current, measured by a Rogowsky coil, is shown in Fig. 3.24c. The microwave radiation output, detected through a 4.7-5.3 GHz bandpass filter, is shown in Fig. 3.24d. The axial magnetic field in this run is 2.4 kG, which corresponds to a cyclotron frequency of 6.8 GHz, hence the device operates in the backward-wave regime.

Another radiation burst, observed with a similar magnetic field in the three-beam carbon-fiber CRM-array, is shown in Fig. 3.25. The emitter voltage of the center channel carbon-fiber cathode is shown in Fig. 3.25a. The accelerating voltage and the detector output are shown in Fig. 3.25b and Fig. 3.25c, respectively. A slightly higher electron energy ($\sim 8\text{kV}$ accelerating voltage) results in a *three-peak* shape of the detector output, as shown in Fig. 3.26c. The burst in center did not pass a 4.7-5.3 GHz bandpass filter and it may be caused by noises. However, the two side peaks of the signal passed through the 4.7-5.3 GHz bandpass filter.

Fig. 3.27 shows a typical case observed in the experiment. After the radiation burst is detected, a breakdown occurs at the accelerating stage. Fig. 3.27d shows the breakdown current. A series of measurements were made in similar conditions with three electron beams. The output power in the receiving antenna attains $\sim 5\text{ W}$.

The multi-beam cold-cathode CRM-array was also operated with five carbon-fiber cathodes. Bursts were observed as shown in Fig. 3.28 and Fig 3.29. However, these bursts could not pass the 4.7-5.3 GHz band pass filter. Meanwhile, we observed the breakdown current, which started at the same time with the bursts at the accelerating stage. Therefore, these bursts may be caused by the breakdown and they are not the same as those in Fig. 3.27.

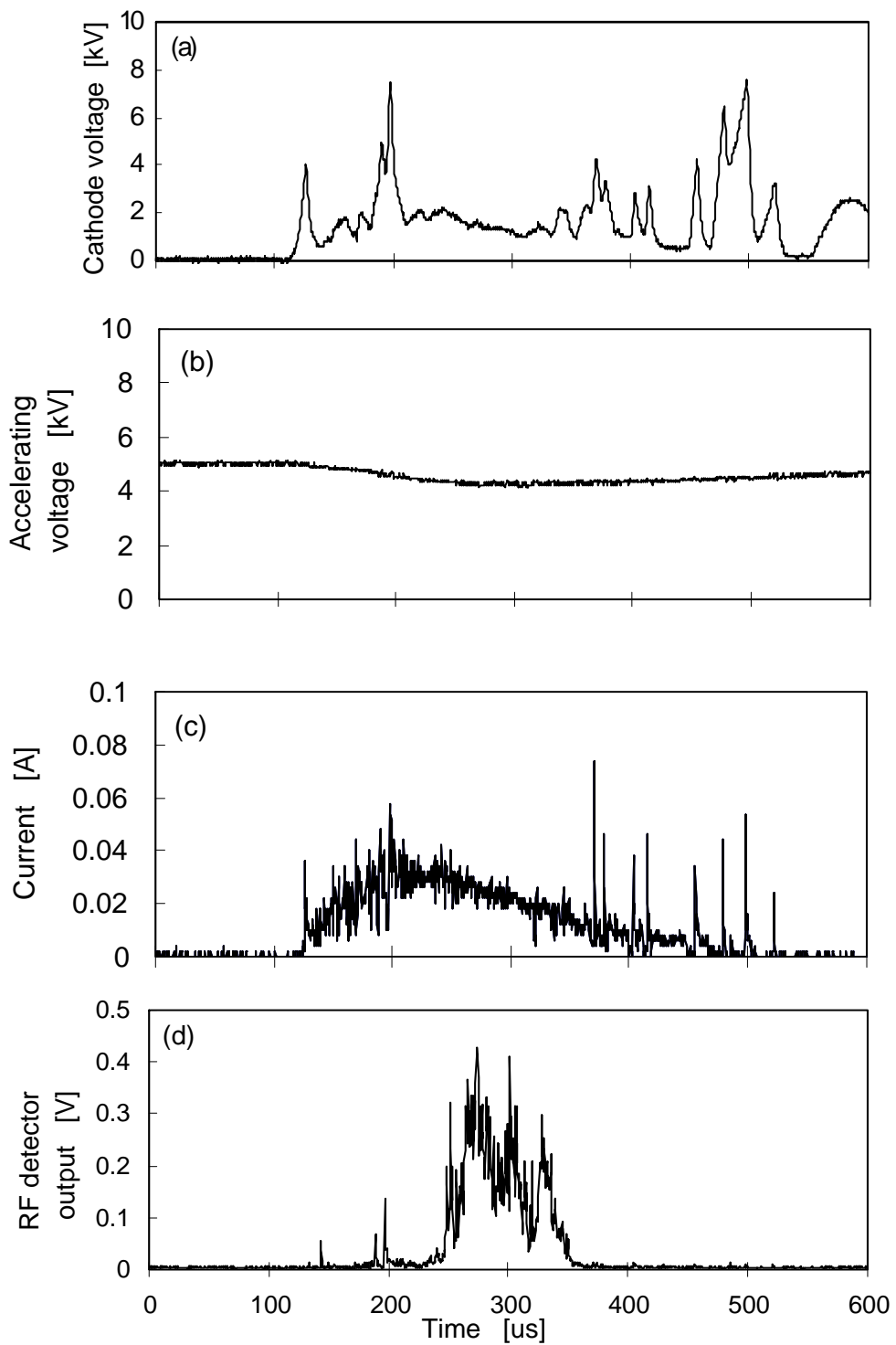


Fig. 3.24. Typical experimental measurements for a three-beam CRM at 2.4 kG: (a) the carbon-fiber cathode voltage, (b) the accelerating voltage, (c) the cathode input current, (d) the RF detector output.

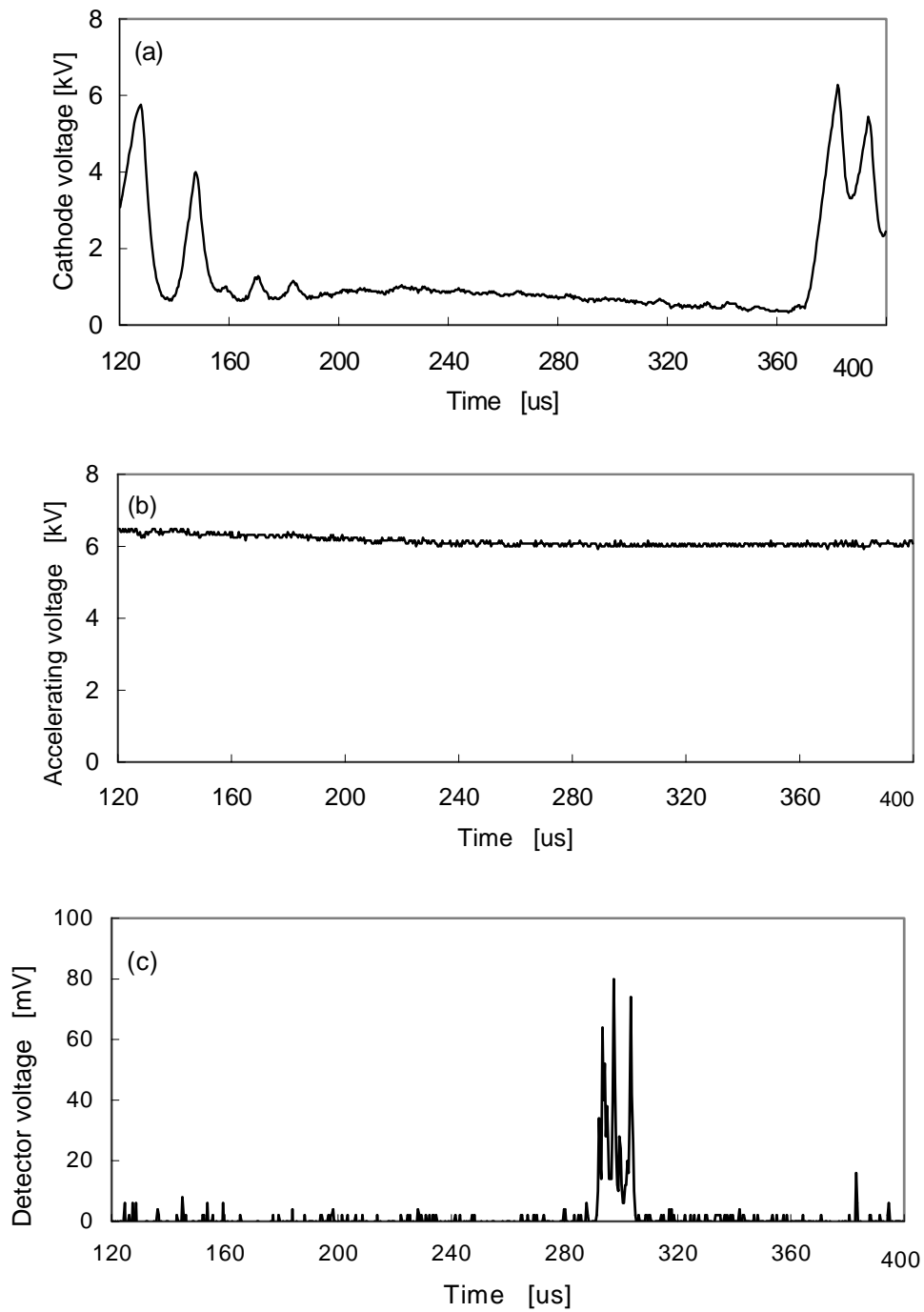


Fig. 3.25. An experimental measurements for a three-beam CRM:
(a) the carbon-fiber cathode voltage, (b) the accelerating voltage,
(c) the RF detector output.

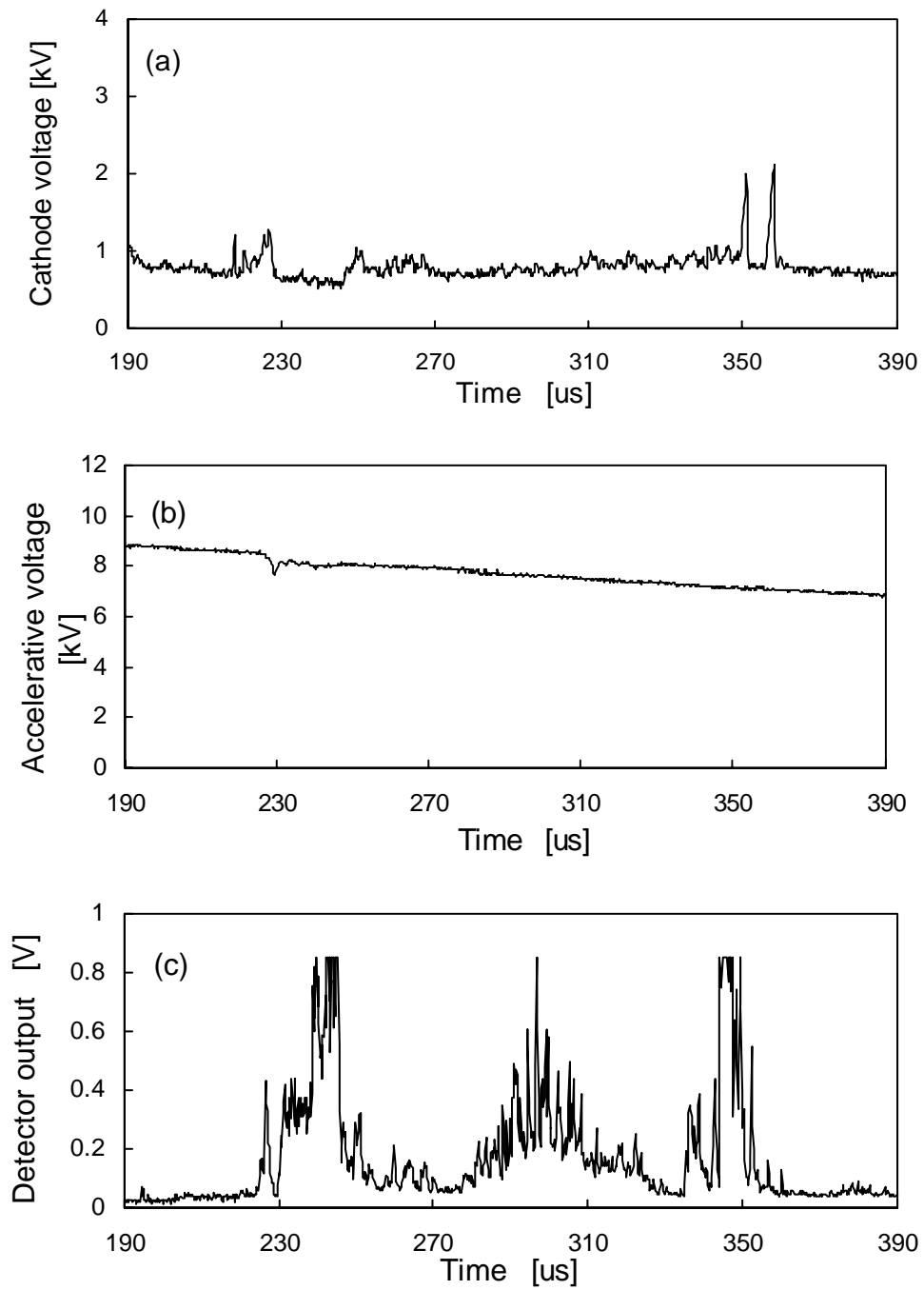


Fig. 3.26. An experimental measurements for a three-beam CRM:

(a) the carbon-fiber cathode voltage, (b) the accelerating voltage,

(c) the RF detector output.

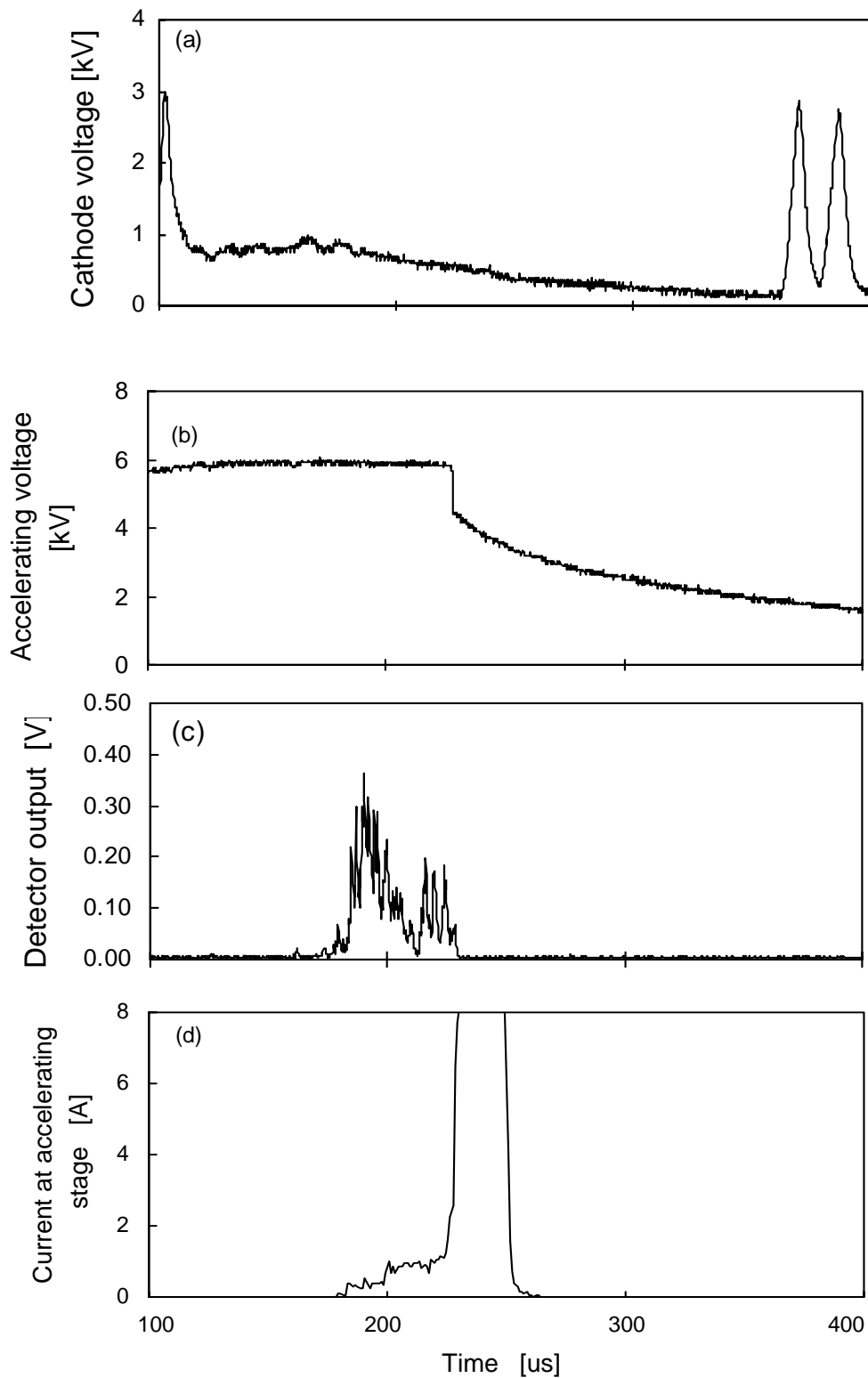


Fig. 3.27. An experimental measurements for a three-beam CRM:
 (a) the carbon-fiber cathode voltage, (b) the accelerating voltage,
 (c) the RF detector output, (d) the current breakdown at accelerating stage.

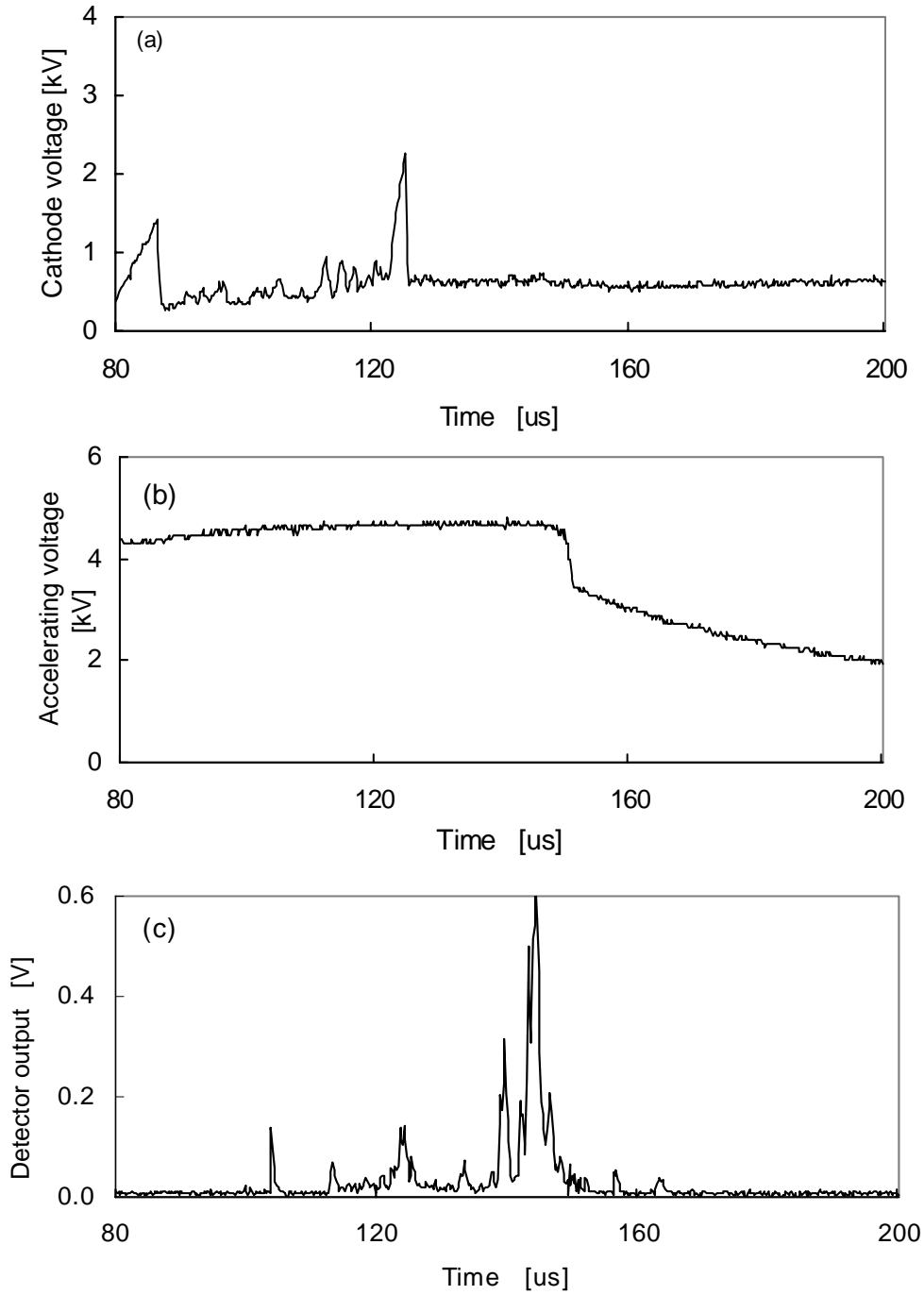


Fig. 3.28. An experimental measurements for a five-beam CRM at 2.1 kG:
(a) the carbon-fiber cathode voltage, (b) the accelerating voltage,
(c) the RF detector output.

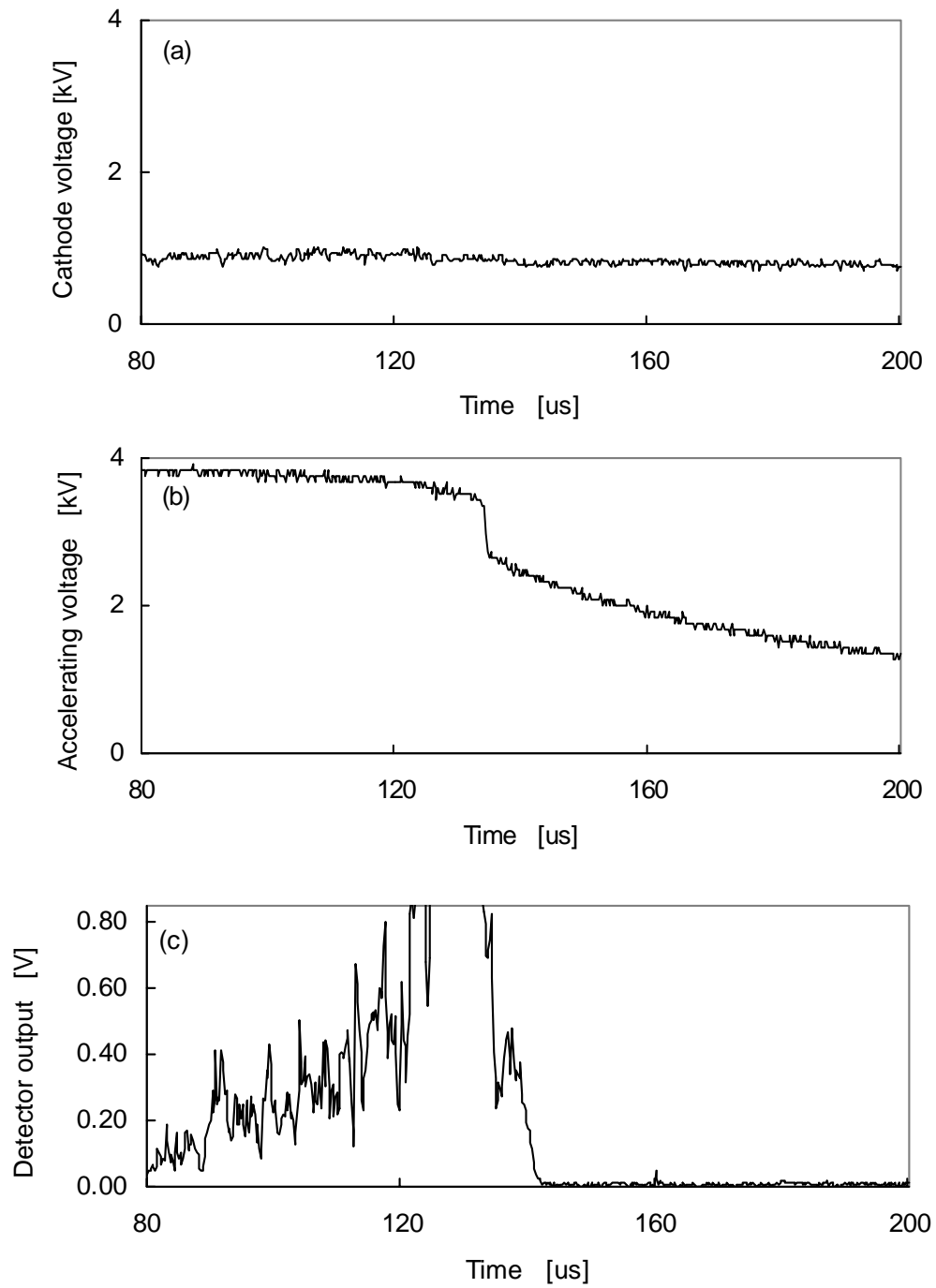


Fig. 3.29. An experimental measurements for a five-beam CRM at 2.1 kG:
 (a) the carbon-fiber cathode voltage, (b) the accelerating voltage,
 (c) the RF detector output.

3.4. Discussions

Considerable progress has been made during this experiment. However, there were some difficulties with the multi-beam cold-cathode CRM-array. Beside the similar difficulties with the thermionic cathode CRM arrays we discussed in Chapter 2, the uniformity of the emission current was a major issue to deal with in the experiments. Since the field-emitted current is extremely sensitive to the value of the field at the emitter tip, and small changes in the anode-cathode separation could lead to large difference in emitted current for each cathode. In the beginning, we used single channel pulse generator to drive the multi-beam carbon-fiber cathode array. Although we tried to maintain parallelism between the anode and the separate cathodes, it was hard to get a uniform emission current since poor accuracy by this manufacture method. No matter how many times we changed the grid voltage, anode voltage, and adjusted the high resistive blaster resistor for each channel, we could not get five emission electron beams simultaneously for the most of shoots. Finally we built a five-channel pulse generator which has five separate output high voltage channels but with the same trigger system. By using this generator the uniformity was improved successfully.

Another issue was the vacuum breakdown. As described in Section 3.1.2.4, the relative long rise time of the high voltage pulse caused the carbon fibers flare on a critical voltage. Since the high voltage ($> 3\text{kV}$) is necessary for CRM interactions, we need a high accelerating voltage between the grid and the anode. However, there was always breakdown when we add a large accelerating voltage at the beginning. During these CRM experiments, we used the break-in operating process for the multi-beam cold-cathode array. The process of operation consists of the following steps. First the accelerating voltage should be increased in gradual, then waiting enough time at each shot in order to reduce the surface contamination, to stabilize the pressure and field emission currents. This time is longer when the number of beams is increased in these experiments. Complying with this process, we have reached 7 kV accelerating voltage in the three-beam carbon-fiber CRM experiment.

The theoretical tuning condition of the CRM interaction (Eq. 1.1) and the Brillouin dispersion diagram of Fig. 3.22 were applied to analyze the three-beam carbon-fiber CRM experimental results. The CRM tuning condition indicates clearly that these interactions occurred with backward waves.

Although we have successfully explored the multi-beam cold-cathode array in the experiment, some improvements need to be done in future. First, the cathodes for this research are fabricated in a very simply way. It will improve the performance if a Spindt type cathode would be used (a possible vendor offering this semiconductor process technology is NEC Corporation in Japan or MCNC in US [115]). Second, it is necessary to use relatively short pulse generators in order to prevent the breakdown, improve the flatness of the emitted current and increase the repetition rate. Third, some improvement in material, such as coating with Cesium iodide (CsI), may also helpful [103,104].

The experiments of the carbon-fiber CRM arrays have clearly demonstrated the principle of the multi-beam CRM scheme with the cold-cathode array, and explored the use of a multi-beam cold-cathode array in vacuum electronic devices. The multi-beam cold-cathode array which is based on commercial carbon fibers was used as an electron source and produced a multi-channel $\sim 400 \mu\text{s}$ long pulse. In the carbon-fiber CRM-array experiments, the three-beam CRM-array operated at low voltages, around 5kV, with a ~ 0.4 ms pulse duration. Clear bursts of RF oscillations were observed around 5 GHz in this experiment. These experimental results show that it could be possible to use cold-cathode arrays in multi-beam CRM devices in the near future.

Chapter 4

Conclusions

The major objective of this study was to demonstrate, for the first time, a multi-beam CRM-array operation, and to study its features experimentally. The significance of the research is the experimental verification of the CRM-array conceptual feasibility, as a stage toward larger multi-beam CRM arrays. In addition, a secondary objective of this research was to explore the multi-beam CRM device using cold-cathode arrays and to develop an efficient, reliable and cost-effective multi-beam electron source.

4.1. Experimental Results

In the experimental study with thermionic cathodes, CRM oscillators were operated in a 2D scheme with one and two low-energy electron-beams (<11 keV, 0.1 A each). Microwave output signals were observed at frequencies around 7 GHz in an axial magnetic field of ~ 3 kG. Spectral measurements of the CRM outputs revealed frequency sweeps, due to electron energy variations during the RF pulses. The cyclotron resonance condition was satisfied with backward spatial harmonics. Both, fast- and slow-wave CRM interactions were observed in this experiment. The results of the two-beam CRM experiment show the feasibility of splitting the electron current to separate beams in the array.

In the carbon-fiber CRM-array experiment, the principle of the multi-beam CRM scheme with cold-cathode array has clearly demonstrated. Using commercial carbon-fiber products, a carbon-fiber cathode array gun was built. The gun consists of two accelerating stages to produce a long-pulse electron-beam array. It demonstrates ~ 400 μ s pulses of ~ 0.1 A in each channel with this configuration. The effective electron energy for each beam in the three-beam carbon-fiber cathode CRM-array can attain more than 7 keV, which is sufficient for CRM interaction. By using this gun, the three-beam carbon-fiber CRM-array operated at low voltages, around 5kV, with a ~ 0.4 ms pulse duration.

Clear bursts of RF oscillations are observed around 5 GHz in the experiment. The experimental results show that it is might possible to use cold-cathode arrays in multi-beam CRM devices in the near future.

4.2 Suggestions for Future Work

These experiments provided a preliminary investigation of the multi-beam CRM-array, and a good starting point for future experimental studies of large-scale multi-beam CRM arrays, and multi-beam cold-cathode arrays. The next challenge is probably to improve the RF output power of the multi-beam CRM devices. The implementation of this goal requires a careful design of the electron guns, and of the microwave components (preferably by advanced 3D codes). A full numerical simulation of the CRM array is essential, not only for a proper design but also for the analysis and optimization of the experimental results.

Further experiments on larger arrays with a repetitive pulsed operation would be useful. The immediate repetitive operation for 2D CRM-array with thermionic cathodes can be designed and constructed. However, future improvement of RF power and operation with carbon-fiber CRM arrays will need relatively short pulse generators in order to prevent the breakdown, improve the flatness of emission current and increase repetitive rate. A potential limitation on the repetition rate with a carbon-fiber cathode array is the time required for the plasma to clear out of the gap. This time seems to be longer in these experiments when the number of beams is increased. It will improve the performance if Spindt type cathodes were used. A good processing for the carbon fibers will be also helpful since the material coating can reduce the closure speed. In order to decrease the closure speed, some improvement in material, such as coating with Cesium iodide (CsI), may be helpful.

A consequent 3D CRM-array experiment that employs a 3×3 thermionic cathode array is under construction and operation in our research group by other researchers, and studies of direct radiation from CRM arrays, active phased-array antenna features, and radiation steering will be carried out in foreseeable future.

Appendix A

Computer Programs and Simulations Documentation

A1. The EGUN Code Simulation for the 2D CRM-array Experiment

The electron gun design was performed with the EGUN code [108] in the 2D CRM-array experiment. The boundary used to model the electron gun which has a 5mm diameter cathode and 6 mm gap is shown in Table A1 and Fig. A1. The potential 1 represents the cathode and the potential 2 represents the anode.

Table A1. The data of the geometry.

Potential	1	1	0	0	3	3	0	0	2	2	2	2	0	1
X	0	2.5	2.5	25	25	25	25	25	25	3	3	0	0	0
Y	0	0	0	0	0	1	1	6	6	6	40	40	40	0

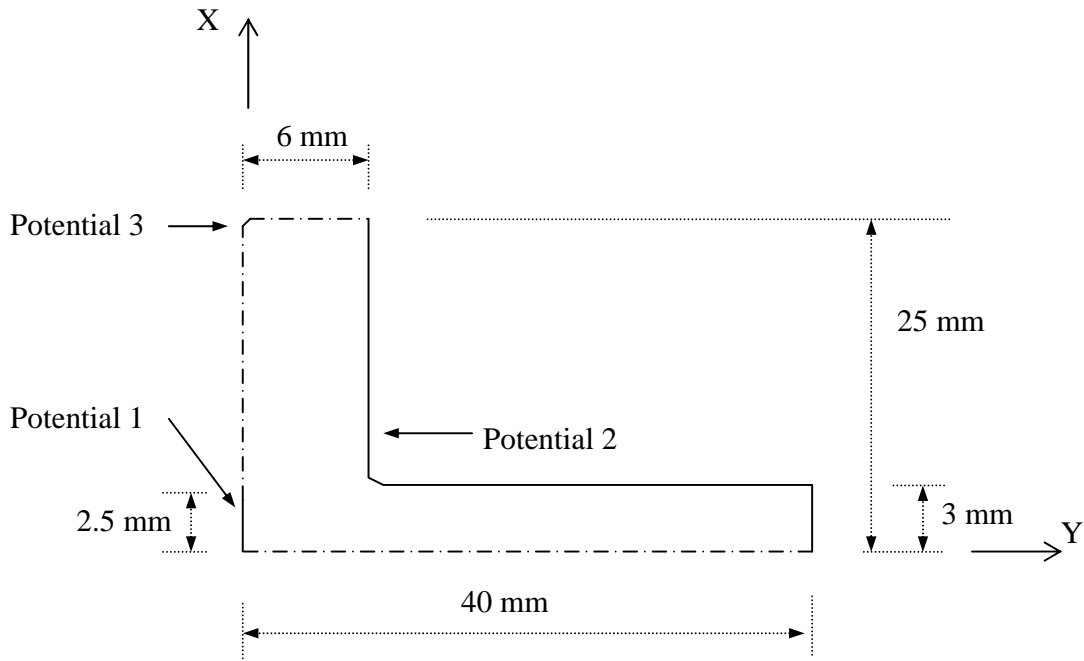


Fig. A1. The geometry used to model the e-gun in the 2D CRM-array experiment with a 5mm diameter cathode.

The Data of File

The EGUN code output for a 5mm cathode and 6mm gap (B~2.2 kG) in Fig. 2.4.

```
&INPUT1 RLIM = 25, ZLIM = 40, NBND = 320, POTN = 3,  
POT( 1) = 1.0000E-01,  
POT( 2) = 7.0000E+03,  
POT( 3) = 1.0000E-01,  
MAGSEG = 0, IAX = 0, AQUAD = 0.0, CSYS = 1,  
MI = 3, SX = 7.50, SY = 4.69, SCALE = ' ',  
PASS = 2, XR = 0.9950, ERROR = 0.1000E-02, TYME = 300.0,  
LSTPOT = 3, LSTMAG = 1, LSTBND = 1, INTPA = 0, POIS = 0, &END  
1 0 1 0.0000000 -0.9990000  
1 1 1 2.0000000 -0.9990000  
1 2 1 2.0000000 -0.9990000  
1 3 0 -0.4980896 0.0000000  
0 4 0 2.0000000 0.0000000  
0 22 0 2.0000000 0.0000000  
0 23 0 2.0000000 0.0000000  
3 24 0 0.9990000 0.0000000  
3 24 1 0.9990000 2.0000000  
3 24 2 0.0000000 -0.9990000  
0 24 3 0.0000000 2.0000000  
0 24 4 0.0000000 2.0000000  
0 24 5 0.0000000 2.0000000  
2 24 6 0.0000000 0.0010000  
2 23 6 2.0000000 0.0010000  
2 5 6 2.0000000 0.0010000  
2 4 6 2.0000000 0.0010000  
2 3 7 0.0010000 2.0000000  
2 3 38 0.0010000 2.0000000  
2 3 39 0.0010000 2.0000000
```

```
2 3 40 0.0010000 0.0052147
2 2 40 2.0000000 0.0052490
2 1 40 2.0000000 0.0052795
2 0 40 0.0000000 0.0053139
0 0 39 0.0000000 2.0000000
0 0 4 0.0000000 2.0000000
0 0 3 0.0000000 2.0000000
0 0 2 0.0000000 2.0000000
```

888

```
&INPUT5 START ='SPHERE', RMAX = 2.500, RAD = 0.2500E+05, MAXRAY =
20,
```

```
LSTRH = 1,UNIT =0.1000E-02
```

```
NMAG=20,
```

```
CR=35,35,35,35,35,35,35,35,35,35,35,35,35,35,35,35,
```

```
CZ=0,10,20,30,40,50,60,70,80,90,100,110,120,130,140,150,160,170,180,190,
```

```
CM=3000,3000,3000,3000,3000,3000,3000,3000,3000,3000,3000,3000,3000,3000,3000,3000,3000,3000,3000,3000,3000,3000,
```

```
&END
```

A2. The Magnetic Fields Calculation for the 2D CRM-array Experiment

The magnetic field at the 2D CRM-array experiment is calculated by Eq.2.1 [109].

The Matlab program follows:

```

%                               Fig2-6mag.m
%   Magnetic field calculation for solenoid and kicker in the 2D multi-beam array
experiment
z=-0.2:5e-5:.8;                %step
u=4*pi*1e-7;                    %constant
N1=120;N2=225*4;                %turns
Ik1=20*3.2;Ik2=20*7.16;        %current
r2=.065;r4=0.103/2;            %Solenoid & Kicker parameters (inner diameter)
r1=.055;r3=0.126/2;            %Solenoid & Kicker parameters (outner diameter)
l1=0.023;l2=.6;                 %length

z2=-0.07/2+0.01-0.3;           %shift
z1=-0.09;

%MAGNETIC FIELD (Kicker)

Bk1=u*N1*Ik1/2/(r2-r1)/l1*((z+z1+l1/2).*log((r2+sqrt(r2^2+(z+z1+l1/2).^2))./ .....
(r1+sqrt(r1^2+(z+z1+l1/2).^2)))-(z+z1-l1/2).*log((r2+sqrt(r2^2+(z+z1-l1/2).^2))./ ....
(r1+sqrt(r1^2+(z+z1-l1/2).^2))));

%MAGNETIC FIELD (Solenoid)

Bs=u*N2*Ik2/2/(r4-r3)/l2*(((z+z2)+l2/2).*log .....
((r4+sqrt(r4^2+((z+z2)+l2/2).^2))./ .....
(r3+sqrt(r3^2+((z+z2)+l2/2).^2)))-((z+z2)-l2/2).*log .....
((r4+sqrt(r4^2+((z+z2)-l2/2).^2))./ ....
(r3+sqrt(r3^2+((z+z2)-l2/2).^2))));

```

```
hold on
plot(z,Bs,'b')
hold on
plot(z,Bk1,'r--')
hold on

title('Magnetic field=f(z)')
xlabel('z (m)'),ylabel('B (tesla)')
grid
```

A3. The EGUN Code Simulation for the Carbon-fiber CRM-array Experiment

The electron gun design was performed with the EGUN code [108] in the carbon-fiber CRM-array experiment. The boundary used to model the electron gun which has a 3mm diameter is shown in Table A2 and Fig. A2. The potential 1 represents the cathode, the potential 2 represents the grid, and the potential 4 represents the anode.

Table A2. The Data of the Geometry.

Potential	1	1	0	0	3	3	0	0	2	2	2	2	0	0	4	4	4	4	4	4	0	1
X	0	1.5	1.5	25	25	25	25	25	25	3	3	25	25	25	25	3	3	25	25	0	0	0
Y	0	0	0	0	0	1	1	8	8	8	9	9	9	19	19	19	21	21	40	40	40	0

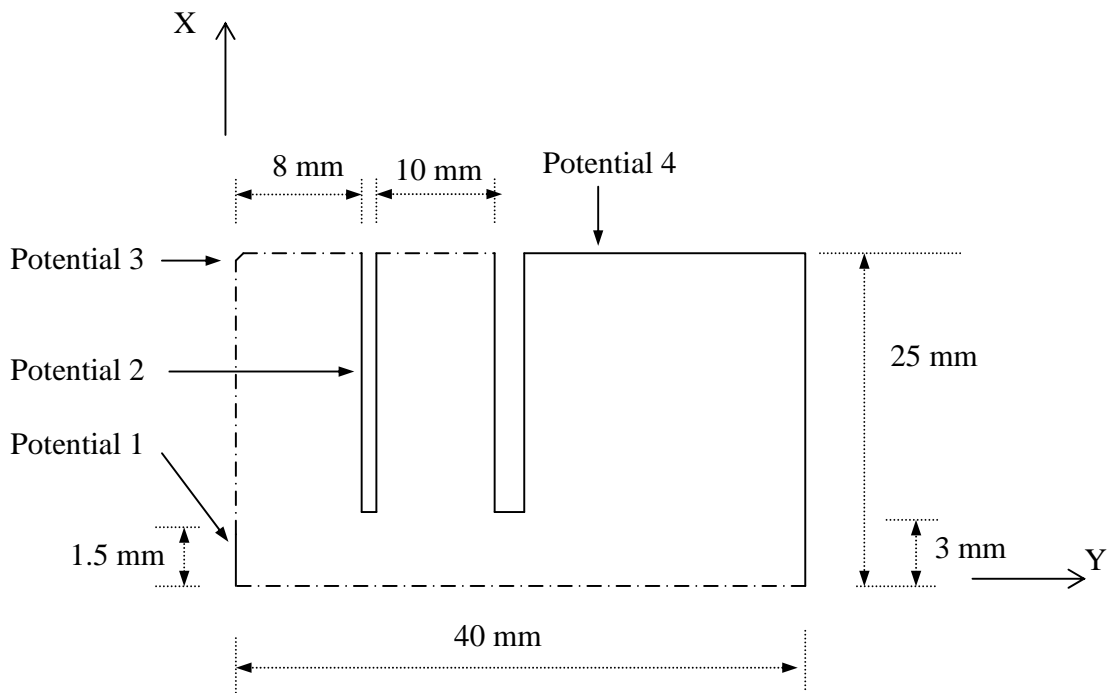


Fig. A2. The geometry used to model the e-gun in the carbon-fiber CRM-array experiment with a 3mm diameter cathode.

The Data of File

The Hermansfedt code output for a 3 mm carbon-fiber cathode in Fig. 3.7.

```
&INPUT1 RLIM = 25, ZLIM = 40, NBND = 320, POTN = 4,  
POT( 1) = 1.0000E-01,  
POT( 2) = 4.0000E+03,  
POT( 3) = 1.0000E-01,  
POT( 4) = 12.0000E+03,  
MAGSEG = 0, IAX = 0, AQUAD = 0.0, CSYS = 1,  
MI = 3, SX = 7.50, SY = 4.69, SCALE = ' ',  
PASS = 2, XR = 0.9950, ERROR = 0.1000E-02, TYME = 300.0,  
LSTPOT = 3, LSTMAG = 1, LSTBND = 1, INTPA = 0, POIS = 0, &END  
1 0 1 0.0000000 -0.9990000  
1 1 1 2.0000000 -0.9990000  
1 2 1 2.0000000 -0.9990000  
1 3 0 -0.9990000 0.0000000  
0 4 0 2.0000000 0.0000000  
0 22 0 2.0000000 0.0000000  
0 23 0 2.0000000 0.0000000  
3 24 0 0.9990000 0.0000000  
3 24 1 0.9990000 2.0000000  
3 24 2 0.0000000 -0.9990000  
0 24 3 0.0000000 2.0000000  
0 24 6 0.0000000 2.0000000  
0 24 7 0.0000000 2.0000000  
2 24 8 0.0000000 0.0010529  
2 23 8 2.0000000 0.0010529  
2 5 8 2.0000000 0.0010529  
2 4 8 2.0000000 0.0010529  
2 3 9 0.0010000 2.0000000  
2 4 10 2.0000000 -0.9990000
```

2	22	10	2.0000000	-0.9990000
2	23	10	2.0000000	-0.9990000
2	24	10	0.0000000	-0.9990000
0	24	11	0.0000000	2.0000000
0	24	17	0.0000000	2.0000000
0	24	18	0.0000000	2.0000000
4	24	19	0.0000000	0.0024853
4	23	19	2.0000000	0.0024853
4	5	19	2.0000000	0.0024853
4	4	19	2.0000000	0.0024853
4	3	20	0.0010000	2.0000000
4	3	21	0.0010000	2.0000000
4	4	22	2.0000000	-0.9990000
4	22	22	2.0000000	-0.9990000
4	23	22	2.0000000	-0.9990000
4	24	22	0.9990000	-0.9990000
4	24	23	0.9990000	2.0000000
4	24	38	0.9990000	2.0000000
4	24	39	0.9990000	2.0000000
4	24	40	0.9990000	0.0052185
4	23	40	2.0000000	0.0052223
4	22	40	2.0000000	0.0052261
4	21	40	2.0000000	0.0052299
4	20	40	2.0000000	0.0052338
4	19	40	2.0000000	0.0052376
4	18	40	2.0000000	0.0052414
4	17	40	2.0000000	0.0052452
4	16	40	2.0000000	0.0052490
4	15	40	2.0000000	0.0052528
4	14	40	2.0000000	0.0052567
4	13	40	2.0000000	0.0052605


```

4 12 40 2.0000000 0.0052681
4 11 40 2.0000000 0.0052719
4 10 40 2.0000000 0.0052757
4 9 40 2.0000000 0.0052795
4 8 40 2.0000000 0.0052834
4 7 40 2.0000000 0.0052872
4 6 40 2.0000000 0.0052910
4 5 40 2.0000000 0.0052948
4 4 40 2.0000000 0.0052986
4 3 40 2.0000000 0.0053024
4 2 40 2.0000000 0.0053062
4 1 40 2.0000000 0.0053101
4 0 40 0.0000000 0.0053139
0 0 39 0.0000000 2.0000000
0 0 4 0.0000000 2.0000000
0 0 3 0.0000000 2.0000000
0 0 2 0.0000000 2.0000000

```

888

&INPUT5 START ='SPHERE', RMAX = 2.000, RAD = 0.2000E+05, MAXRAY =
-20,

LSTRH = 1,UNIT =0.1000E-02

NMAG=20,

CR=50,50,50,50,50,50,50,50,50,50,50,50,50,50,50,50,50,

CZ=-20,-10,0,10,20,30,40,50,60,70,80,90,100,110,120,130,140,150,160,170,

CM=1500,1500,1500,1500,1500,1500,1500,1500,1500,1500,1500,1500,1500,1500,1500,
00,1500,1500,1500,1500,1500,

&END

A4. The Magnetic Fields Calculation for the Carbon-fiber CRM-array

Experiment

The magnetic field at the Carbon-fiber CRM-array experiment is calculated by Eq.2.1 [109]. It is a little different with Section A2, since the solenoid consists of three coils. The Matlab program is as follows:

```
whitebg
clc
clear
hold off
% Magnetic field of 5-beam CRM-array
z=-0.1:5e-5:.9;
u=4*pi*1e-7;    % air permability
%Solenoid & Kicker parameters
N1=15;N2=390*2;N3=15;           %turns
Ik1=20*8.24;Ik2=20*8.24;Ik3=20*8.24; %currents
r2=.1265/2;r4=0.1225/2;r6=0.1265/2; %external radius
r1=.1225/2;r3=0.1143/2;r5=0.1225/2; %inner radius
l1=0.03;l2=.8;l3=0.03;         %length
z1=-(0.028+0.015);             %center of sidecoil1
z2=-0.4;                       %center of solenoid
z3=-(0.8-0.028-0.015);        %center of sidecoil2

%MAGNETIC FIELD (side coil1)
Bk1=u*N1*Ik1/2/(r2-r1)/l1*((z+z1+l1/2).*log((r2+sqrt(r2^2+(z+z1+l1/2).^2))./ .....
(r1+sqrt(r1^2+(z+z1+l1/2).^2)))-(z+z1-l1/2).*log((r2+sqrt(r2^2+(z+z1-l1/2).^2))./ ....
(r1+sqrt(r1^2+(z+z1-l1/2).^2))));
%MAGNETIC FIELD (side coil2)
Bk3=u*N3*Ik3/2/(r6-r5)/l3*((z+z3+l3/2).*log((r6+sqrt(r6^2+(z+z3+l3/2).^2))./ .....
(r5+sqrt(r5^2+(z+z3+l3/2).^2)))-(z+z3-l3/2).*log((r6+sqrt(r6^2+(z+z3-l3/2).^2))./ ....
(r5+sqrt(r5^2+(z+z3-l3/2).^2))));
```

```

                                %MAGNETIC FIELD (Solenoid)
Bs=u*N2*I $k_2/2/(r_4-r_3)/12*((z+z_2)+1/2).$ *log(( $r_4+\sqrt{r_4^2+((z+z_2)+1/2)^2}$ ))./ .....
    ( $r_3+\sqrt{r_3^2+((z+z_2)+1/2)^2}$ ))-(( $z+z_2$ )-1/2).*log(( $r_4+\sqrt{r_4^2+((z+z_2)-$ 
12/2).^2))./ ....
    ( $r_3+\sqrt{r_3^2+((z+z_2)-1/2)^2}$ )));

B=Bk1+B $s$ +Bk3;
plot(z,B,'k')
hold on
plot(z,B $s$ ,'k-')
hold on
plot(z,Bk1,'k--')
hold on
plot(z,Bk3,'k--')
hold on
title('Mag.field=f(z)')
xlabel('z (m)'),ylabel('B (tesla)')
grid

z=0.04;
%MAGNETIC FIELD (side coil1)
Bk1=u*N1*I $k_1/2/(r_2-r_1)/11*((z+z_1+1/2).$ *log(( $r_2+\sqrt{r_2^2+(z+z_1+1/2)^2}$ ))./ .....
    ( $r_1+\sqrt{r_1^2+(z+z_1+1/2)^2}$ ))-(( $z+z_1$ -1/2).*log(( $r_2+\sqrt{r_2^2+(z+z_1-1/2)^2}$ ))./ ....
    ( $r_1+\sqrt{r_1^2+(z+z_1-1/2)^2}$ )));

                                %MAGNETIC FIELD (side coil2)
Bk3=u*N3*I $k_3/2/(r_6-r_5)/13*((z+z_3+1/2).$ *log(( $r_6+\sqrt{r_6^2+(z+z_3+1/2)^2}$ ))./ .....
    ( $r_5+\sqrt{r_5^2+(z+z_3+1/2)^2}$ ))-(( $z+z_3$ -1/2).*log(( $r_6+\sqrt{r_6^2+(z+z_3-1/2)^2}$ ))./ ....
    ( $r_5+\sqrt{r_5^2+(z+z_3-1/2)^2}$ )));

%MAGNETIC FIELD (Solenoid) `shifted .25`
Bs=u*N2*I $k_2/2/(r_4-r_3)/12*((z+z_2)+1/2).$ *log .....
    (( $r_4+\sqrt{r_4^2+((z+z_2)+1/2)^2}$ ))./ .....

```

```

(r3+sqrt(r3^2+((z+z2)+12/2).^2))-((z+z2)-12/2).*log .....
((r4+sqrt(r4^2+((z+z2)-12/2).^2))./ ....
(r3+sqrt(r3^2+((z+z2)-12/2).^2)));

```

```
bb=Bk1+Bs+Bk3 ;
```

```
plot(z,bb,'r*') %
```

```
set(gca,'XLim',[-0.1 0.9])%
```

```
set(gca,'yLim',[0 0.25])%
```

Circuits of the Pulsed Power Devices

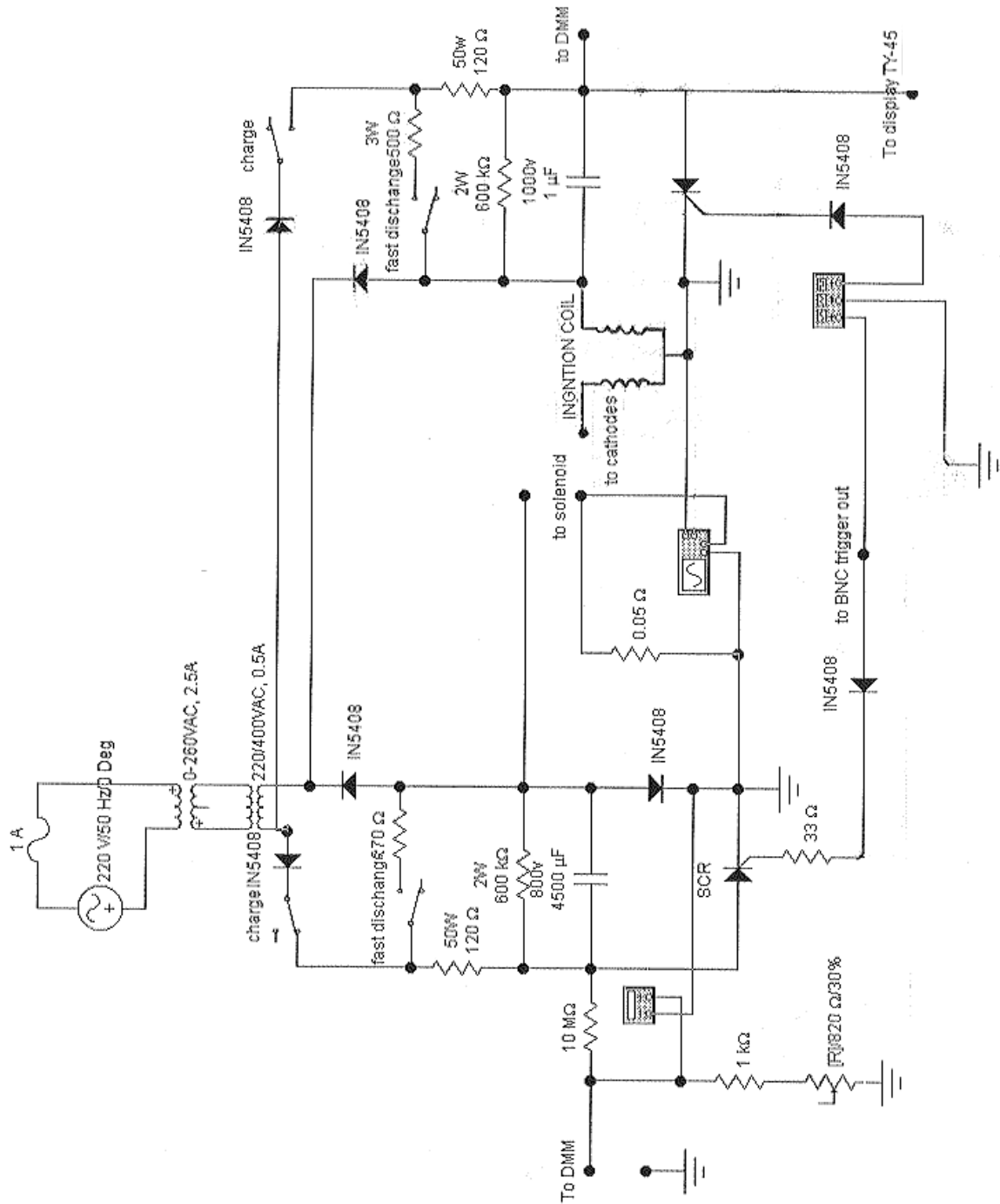


Fig. B1. Circuit of the gun-solenoid pulser.

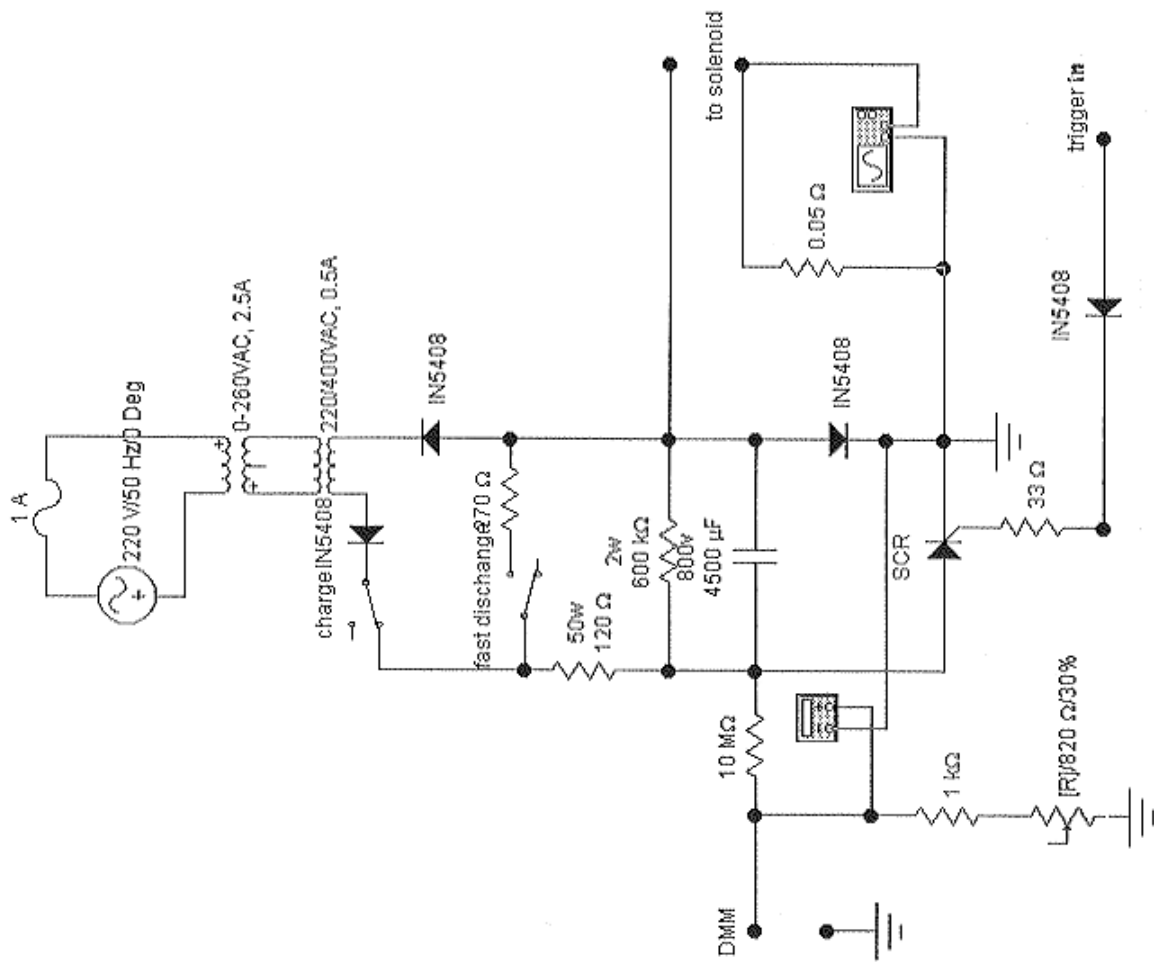


Fig. B2. Circuit of the kicker pulser.

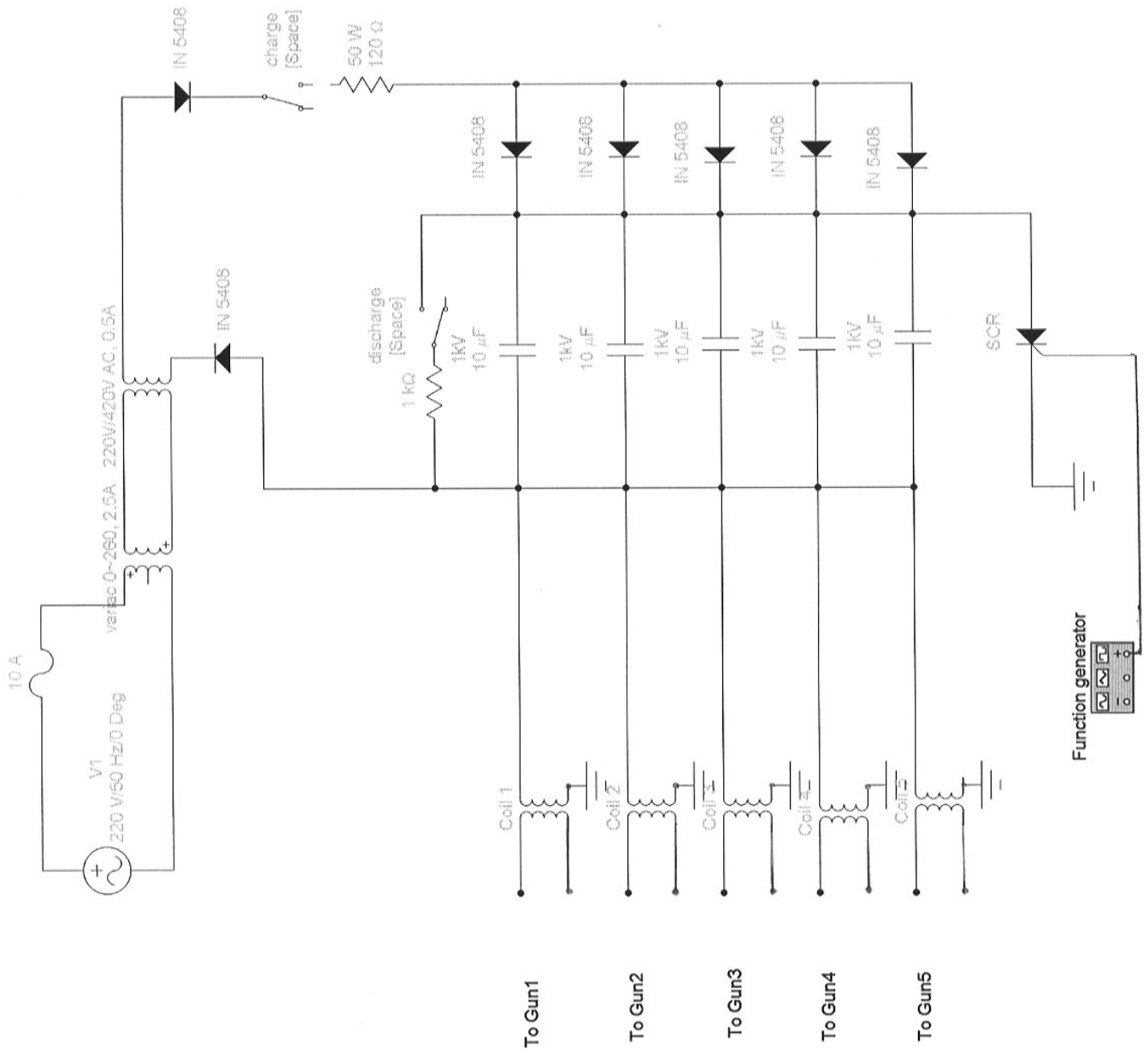


Fig. B3. Circuit of the multi-channel gun pulser.

Appendix C

The Modified Marx Generator

C1. Model 615 MR Pulserad

The Model 615 MR Pulserad is an electron-accelerator system designed specifically for high-power magnetron experiments by Physics International Company. It consists of five subassemblies: (1) a DC power supply and controls, (2) trigger amplifiers, (3) a Marx generator, (4) a pulse clipping switch (crowbar), and (5) a high-voltage vacuum bushing (diode) [116].

Two trigger amplifiers mounted outside the pulser tank provide the high-level signals required to trigger the Marx generator and the crowbar switch. The trigger systems are comprised of a PT-70 control panel and a PT-55 trigger amplifier.

Two inputs are required for these trigger operations: (1) a 7 kV DC bias and (2) a positive 300 V trigger. These inputs are supplied at the control console. The output of the trigger amplifier is a positive 50 kV pulse with a risetime of ≤ 10 ns and a duration of about 50 ns.

External synchronization can be applied to the control function panel but must meet the following requirements: (1) $\geq +10$ V, (2) ≤ 10 ns risetime, and (3) a pulse width of 50 to 100 ns.

The Pulserad 615 MR Marx generator consists of 6 energy storage "stages". In addition to a 0.5 μ F high voltage capacitor, each stage also consists of some resistors and a spark gap which is pressurized with SF₆. All the capacitors in the circuit are charged in parallel by the high voltage DC power supply. When the capacitors have been charged to the desired voltage level, the first stage is triggered by PT-55 trigger amplifier. This trigger pulse, which must exceed the breakdown strength (as low as 3 kV/mm) of the

Marx gas in use (typically Nitrogen), causes the dielectric gas in the first stage to breakdown and become ionized (and thereby conducting). This effect causes the potential across the second stage gap to be twice the charging voltage. When all the spark gaps breakdown, the capacitors become connected in series across the load. Each capacitor is shunted by isolation resistors. Ignoring the losses in the isolation resistors and series resistive drops, the output voltage of the generator is six times of the DC charging voltage. A 12.5Ω series-damping resistor is placed between the Marx and the diode to minimize reversal when the crowbar switch is fired.

C2. The Modified Model 615 Pulserad

The modified Pulserad 615 MR Marx generator is composed of capacitors, spark gaps, and resistors electrically arranged as shown in Fig. C1. Since we need a moderate voltage ($< 20 \text{ kV}$) and long duration pulse in the experiment, we use the capacitor bank to supply the high voltage without the energy storage "stages". A spark gap is used as a fast speed switch. A $1 \text{ k}\Omega$ series resistor is placed between the spark gap and output in order to protect the capacitors.

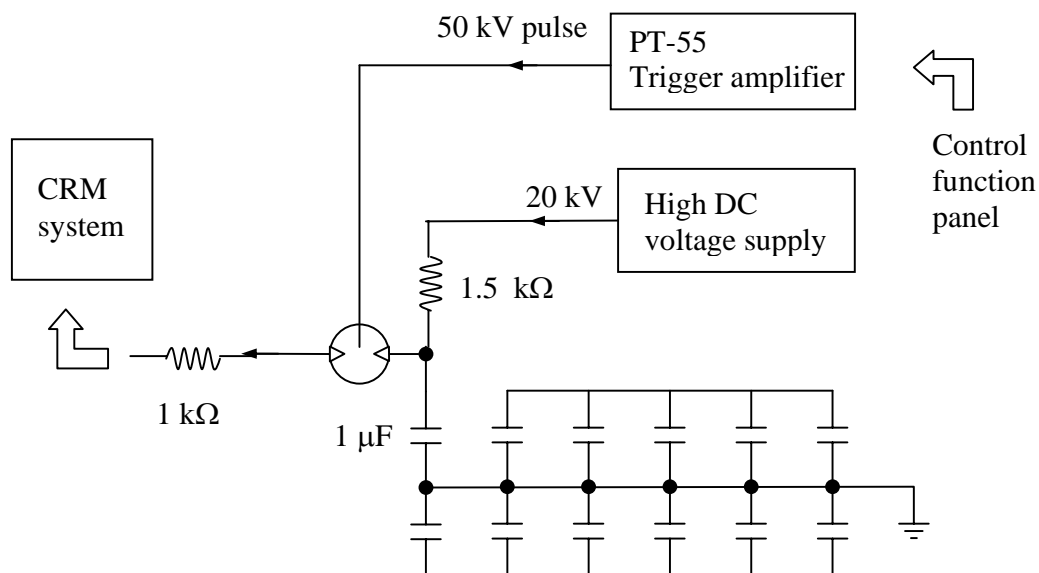


Fig. C1. The modified circuit in Model 615 MR Pulserad.

References

1. J. L. Hirshfield and J. M. Wachtel, "Electron cyclotron maser," *Phys. Rev. Lett.* **12**, 533-536 (1964).
2. K. R. Chu, J. L. Hirshfield, "Comparative study of the axial and azimuthal bunching mechanisms in electromagnetic cyclotron instabilities," *Phys. Fluids* **21**, 461-466 (1978), and references therein.
3. R. Q. Twiss, "Radiation transfer and the possibility of negative absorption in radio astronomy," *Australian J. Phys.* **11**, 564-579 (1958).
4. J. Schneider, "Stimulated emission of radiation by relativistic electrons in a magnetic field," *Phys. Rev. Lett.* **2**, 504-505 (1959).
5. A. V. Gaponov, "Interaction between electron fluxes and electromagnetic waves in waveguides," *Izv. VUZ., Radiofizika* **2**, 450-462 (1959).
6. J. L. Hirshfield and V. L. Granatstein, "The electron cyclotron maser - an historical survey," *IEEE Trans. MTT-25*, 522-527 (1977), and references therein.
7. A. V. Gaponov, M. I. Petelin, and V. K. Yulpatov, "The induced radiation of excited classical oscillators and its use in high-frequency electronics," *Radio Physics and Quantum Electronics* **10**, 794-813 (1967).
8. V. L. Granatstein, R. K. Parker, and C. M. Armstrong, "Scanning the technology vacuum electronics at the dawn of the twenty – first century," *Proceedings of the IEEE*, **87**, 702-716 (1999).
9. G. S. Nusinovich, M. Korol, and E. Jerby, "Theory of the anomalous Doppler cyclotron-resonance-maser amplifier with tapered parameters," *Phys. Rev. E* **59**, 2311-2321 (1999).
10. M. Einat and E. Jerby, "Normal and anomalous Doppler effects in a dielectric loaded stripline cyclotron-resonance maser oscillator," *Phys. Rev. E* **56**, 5996-6001 (1997).
11. S. Yu. Galuzo, V. I. Kanavets, A. I. Slepko, V. A. Pletyushkin, "Relativistic cyclotron accelerator exploiting the anomalous Doppler effect," *Sov. Phys. Tech. Phys.* **27**, 1030-1032 (1982).

12. A. N. Didenko, A. R. Borisov, G. P. Fomenko, A. S. Shlapakovskii, Y. G. Shtein, "Cyclotron maser using the anomalous Doppler effect," *Sov. Phys. Tech. Lett.* **9**, 572-573 (1983).
13. K. Ogura, M. R. Amin, K. Minami, X. D. Zheng, Y. Suzuki, W. S. Kim, T. Watanabe, Y. Carmel, and V. L. Granatstein, "Experimental demonstration of a high-power slow-wave electron cyclotron maser based on a combined resonance of Cherenkov and anomalous Doppler interactions," *Phys. Rev. E* **53**, 2726-2729 (1996).
14. V. L. Granatstein and I. Alexeff, Edited, *High-power microwave sources*, Artech House, Boston •London, 1987.
15. V. A. Flyagin, A. V. Gaponov, M. I. Petelin, and V. K. Yulpatov, "The Gyrotron," *IEEE Trans. MTT-25*, 514-521 (1977), and references therein.
16. A. V. Gaponov-Grekhov and V. L. Granatstein, edited, *Applications of High-power microwaves*, Artech House, Boston, 1994.
17. K. L. Felch, B. G. Danly, H. R. Jory, K. E. Kreischer, W. Lawson, B. Levush, and R. J. Temkin, "Characteristics and applications of fast-wave gyrodevices," *Proceedings of the IEEE*, **87**, 752-781 (1999).
18. S. H. Gold and G. S. Nusinovich, "Review of high-power microwave source research," *Rev. Sci. Instrum.* **68**, 3945-3974 (1997).
19. V. L. Granatstein, M. Herndon, P. Sprangle, Y. Carmel, and J. A. Nation, "Gigawatt microwave emission from an intense relativistic electron beam," *Plasma Physics* **17**, 23-28 (1975).
20. J. Benford and J. Swegle, *High-power microwave*, Artech House, Boston •London, 1992.
21. K. R. Chu, "Theory of electron cyclotron maser interaction in a cavity at the harmonic frequencies," *Phys. Fluids* **21**, 2354-2364 (1978).
22. T. Idehara, T. Tatsukawa, I. Ogawa, H. Tanabe, T. Mori, S. Wada, and T. Kanemaki, "Development of a second cyclotron harmonic gyrotron operating at 0.8 mm wavelength," *Appl. Phys. Lett.* **56**, 1743-1745 (1990).

23. T. Idehara, T. Tatsukawa, I. Ogawa, H. Tanabe, T. Mori, S. Wada, G. F. Brand and M. H. Brennan, "Development of a second cyclotron harmonic gyrotron operating at submillimeter wavelengths," *Phys. Fluids B* **4**, 267-273 (1992).
24. T. Idehara, T. Tatsukawa, I. Ogawa, S. Wada, K. Yoshizue, F. Inoue and G. F. Brand, "Single-mode operation of a submillimeter wave gyrotron at the third-harmonic resonance," *Phys. Fluids B* **4**, 769-770 (1992).
25. T. Idehara, Y. Shimizu, K. Ichikawa, S. Makino, K. Shibutani, K. Kurahashi, T. Tatsukawa, I. Ogawa, Y. Okazaki, T. Okamoto, "Development of a medium power, submillimeter wave gyrotron using a 17 T superconducting magnet," *Phys. Plasmas* **2**, 3246-3248 (1995).
26. G. F. Brand, P. W. Fekete, K. Hong, K. J. Moore, T. Idehara, "Operation of a tunable gyrotron at the second harmonic of the electron cyclotron frequency," *Int. J. Electronics* **68**, 1099-1111 (1990).
27. K. D. Hong and G. F. Brand, "A150-600 GHz step-tunable gyrotron," *J. Appl. Phys.* **74**, 5250-5258 (1993).
28. T. Idehara, I. Ogawa, M. Pereyaslavets, N. Nishida, K. Yoshida, "Development of frequency-tunable, medium power gyrotrons (Gyrotron FU series) as submillimeter wave radiation sources," Scientific Program and Abstracts of the International Research Workshop on CRMs and Gyrotrons, Kibbutz Ma'ale Hachamisha, Israel, May 18-21, 1998, pp. 24.
29. M. I. Petelin, "On the theory of ultrarelativistic cyclotron self-resonance maser," *Izv. VUZ., Radiofizika* **17**, 902-908 (1974).
30. V. L. Bratman, N. S. Ginzburg, G. S. Nusinovich, M. I. Petelin and P. S. Strelkov, "Relativistic gyrotrons and cyclotron autoresonance masers," *Int. J. Electronics* **51**, 541-567 (1981).
31. I. E. Botvinnik, V. L. Bratman, A. B. Volkov, C. G. Denisov, B. D. Kol'chugin, and M. M. Ofitserov, "Cyclotron-autoresonance maser with a wavelength of 24 mm," *Pis'ma Zh. Tekh. Fiz.* **8**, 1386-1389 (1982).
32. I. E. Botvinnik, V. L. Bratman, A. B. Volkov, N. S. Ginzburg, G. G. Denisov, B. D. Kol'chugin, M. M. Ofitserov, and M. I. Petelin, "Free-electron masers with Bragg resonators," *Pis'ma Zh. Eksp. Teor. Fiz.* **35**, 418-420 (1982).

33. V. L. Bratman, G. G. Denisov, N. S. Ginzburg, and M. I. Petelin, "FEL's with Bragg reflection resonators: cyclotron autoresonance masers versus ubitrons," *IEEE J. Quant. Electron.* **19**, 282-296 (1983).
34. A. C. DiRienzo, G. Bekefi, C. Chen, and J. S. Wurtele, "Experimental and theoretical studies of a 35 GHz cyclotron autoresonance maser amplifier," *Phys. Fluids B* **3**, 1755-1765 (1991).
35. S. Alberti, B. G. Danly, G. Gulotta, E. Giguët, T. Kimura, W. L. Menninger, J. L. Rullier, and R. J. Temkin, "Experimental studies of a 28 GHz high-power long-pulse cyclotron autoresonance maser oscillator," *Phys. Rev. Lett.* **71**, 2018-2021 (1993).
36. V. L. Bratman, G. G. Denisov, B. D. Kol'chugin, S. V. Samsonov, and A. B. Volkov, "Experimental demonstration of high-efficiency cyclotron autoresonance maser operation," *Phys. Rev. Lett.* **75**, 3102-3105 (1995).
37. V. L. Bratman, Yu. K. Kalynov, M. M. Ofitserov, S. V. Samsonov, and A. V. Saviolov, "CARMs and relativistic gyrotrons as effective sources of millimeter and submillimeter waves," *Digest of the 22nd International Conference on Infrared and Millimeter Waves*, Wintergreen, Virginia, USA, July 20-25, 1997, pp. 58-60.
38. C. Chen and J. S. Wurtele, "Linear and nonlinear theory of cyclotron autoresonance masers with multiple waveguide modes," *Phys. Fluids B* **3**, 2133-2148 (1991).
39. R. B. McCowan, A. W. Fliflet, S. H. Gold, W. M. Black, A. K. Kinkead, V. L. Granatstein, and M. S. Sucey, "The design of a 100-GHz CARM oscillator experiment," *IEEE Trans. Electron Devices* **36**, 1968-1975 (1989).
40. T. H. Kho and A. T. Lin, "Slow-wave electron cyclotron maser," *Phys. Rev. A* **38**, 2883-2888 (1988).
41. K. R. Chu, A. K. Ganguly, V. L. Granatstein, J. L. Hirshfield, S. Y. Park, and J. M. Baird, "Theory of a slow wave cyclotron amplifier," *Int. J. Electronics* **51**, 493-502 (1981).
42. A. K. Ganguly and S. Ahn, "Nonlinear theory of the slow-wave cyclotron amplifier," *Phys. Rev. A* **42**, 3544-3554 (1990).
43. K. R. Chu, P. Sprangle, and V. L. Granatstein, "Theory of a dielectric loaded cyclotron traveling wave amplifier," *Bull. Am. Phys. Soc.* **23**, 748 (1978).

44. H. Guo, L. Chen, H. Keren, and J. L. Hirshfield, "Measurements of gain for slow cyclotron waves on an annular electron beam," *Phys. Rev. Lett.* **49**, 730-733 (1982).
45. K. C. Leou, D. B. McDermott, and N. C. Luhmann Jr., "Dielectric-loaded wideband gyro-TWT," *IEEE Trans. Plasma Science* **20**, 188-196 (1992).
46. E. Jerby, G. Bekefi, "Cyclotron-maser experiments in a periodic waveguide," *Phys. Rev. E* **48**, 4637-4641 (1993).
47. E. Jerby, A. Shahadi, V. Grinberg, V. Dichtiar, M. Sheinin, E. Agmon, H. Golombek, V. Trebich, M. Bensal, and G. Bekefi, "Cyclotron maser oscillator experiments in a periodically loaded waveguide," *IEEE J. Quant. Electron.* **31**, 970-978 (1995).
48. E. Jerby, "Linear analysis of periodic-waveguide cyclotron maser interaction," *Phys. Rev. E* **49**, 4487-4496 (1994).
49. M. Korol and E. Jerby, "Quasi-anomalous Doppler effect in a periodic-waveguide cyclotron maser," *Nucl. Instrum. and Meth. A* **375**, 222-225 (1996).
50. M. Thumm, "State of the art of high power gyro-devices and free-electron masers update 1997," Forschungszentrum Karlsruhe, Institut für Technische Physik, Int. Rep., Feb. 1998.
51. E. Ott and W. M. Manheimer, "Theory of microwave emission by velocity-space instabilities of an intense relativistic electron beam," *IEEE Trans. Plasma Science* **3**, 1-5 (1975).
52. P. Sprangle and W. M. Manheimer, "Coherent nonlinear theory of a cyclotron instability," *Phys. Fluids* **18**, 224-230 (1975).
53. P. Sprangle and A. T. Drobot, "The linear and self consistent nonlinear theory of the electron cyclotron maser instability," *IEEE Trans.* **MTT-25**, 528-544 (1977).
54. K. R. Chu, A. T. Drobot, H. H. Szu and P. Sprangle, "Theory and simulation of the gyrotron traveling wave amplifier operating at cyclotron harmonics," *IEEE Trans.* **MTT-28**, 313-317 (1980).
55. Y. Y. Lau, "Simple macroscopic theory of cyclotron maser instabilities," *IEEE Trans. Electron Devices* **29**, 320-335 (1982).

56. A. W. Fliflet, "Linear and non-linear theory of the Doppler-shifted cyclotron resonance maser based on TE and TM waveguide modes," *Int. J. Electronics* **61**, 1049-1080 (1986).
57. G. S. Nusinovich, P. E. Latham, and O. Dumbrajs, "Theory of relativistic cyclotron masers," *Phys. Rev. E* **52**, 998-1012 (1995).
58. E. Jerby, "Multi-beam cyclotron-resonance maser in periodic-waveguide arrays," Grant proposal # 724/94-2, Israeli Academy of Science (1994).
59. E. Jerby, M. Korol, L. Lei, V. Dikhtiar, R. Milo, and I. Mastovsky, "Cyclotron-resonance maser array-concept, theory, and experiments," Digest of the 22nd International Conference on Infrared and Millimeter Waves, Wintergreen, Virginia, USA, July 20-25, 1997, pp. 65-66.
60. E. Jerby, A. Kesar, M. Korol, L. Lei, and V. Dikhtyar, "Cyclotron-resonance-maser arrays," *IEEE Trans. Plasma Science* **27**, 445-455 (1999), and references therein.
61. M. Korol and E. Jerby, "Linear analysis of a multi-beam cyclotron resonance maser array," *Phys. Rev. E* **55**, 5934-5947 (1997), and references therein.
62. M. Korol and E. Jerby, "Multimode linear theory of a multi-beam cyclotron resonance maser array," to be published.
63. A. Kesar and E. Jerby, "Power beam steering by a CRM array," *Phys. Rev. E* **59**, 2464-2466 (1999).
64. J. Bernier, Patent No.992-853, Sept. 15, 1944 (France).
65. Y. Besov, "Multiple beam klystrons," Proceedings of the International Workshop on Pulsed RF Power Sources for Linear Colliders (RF 98): High Energy Density Microwaves, 4th, Pajaro Dunes, CA, Oct. 5-9, 1998, pp. 91-106.
66. E. A. Gelvich, L. M. Borisov, Y. V. Zhary, A. D. Zakurdayev, A. S. Pobedonostsev, and V. I. Poognin, "The new generation of high-power multiple-beam klystrons," *IEEE Trans. MTT-41*, 15-19 (1993), and references therein.
67. Datasheets of the ISTOK's products: IKS-9007-6 Cavity, 36 Beam Klystron (<http://www.istok.com/IKS-9007.html>), IKS-9009-6 Cavity, 36 Beam Klystron (<http://www.istok.com/IKS-9009.html>).

68. A. S. Gilmour, "RF tubes for space-based accelerators," *IEEE Trans. Electron. Dev.* **38**, 2190-2204 (1991).
69. C. Bearzatto, A. Beunas, G. Faillon, "Long pulse and large bandwidth multibeam klystron," *Proceedings of the International Workshop on Pulsed RF Power Sources for Linear Colliders (RF 98): High Energy Density Microwaves, 4th*, Pajaro Dunes, CA, Oct. 5-9, 1998, pp. 107-116.
70. Ding Yaogen, Peng Jun, Zhu Yunsu, Shi Shaoming, "Theoretical and experimental research on multi-beam klystron," *Proceedings of the International Workshop on Pulsed RF Power Sources for Linear Colliders (RF 98): High Energy Density Microwaves, 4th*, Pajaro Dunes, CA, Oct. 5-9, 1998, pp. 126-135.
71. G. Caryotakis, E. Jongewaard, R. L. Kustom, N. C. Luhmann, Jr, M. I. Petelin, G. Scheitrum, A. Vlieks, "W-band micro-fabricated modular klystrons," *Proceedings of SPIE* **3158**, 129-136 (1997).
72. G. S. Nusinovich, B. Levush, and B. G. Danly, "Theory of multi-beam stagger-tuned gyroklystrons," *IEEE Tran. Plasma Science* **26**, 475-481 (1998).
73. G. Bekefi, "Double-stream cyclotron maser," *J. Appl. Phys.* **71**, 4129-4131 (1992).
74. C. Chen, G. Bekefi, and W. Hu, "Linear and nonlinear analysis of the cyclotron two-stream instability," *Phys. Fluids B.* **5**, 4490-4494 (1993).
75. C. Chen, P. Catravas, and G. Bekefi, "Growth and saturation of stimulated beam modulation in a two-stream relativistic klystron amplifier," *Appl. Phys. Lett.* **62**, 1579-1581 (1993).
76. C. Chen, "Development of a high-power X-band relativistic two-stream amplifier," *Proceedings of SPIE*, **3158**, 171-174 (1997).
77. A. S. Gilmour, Jr., *Microwave tubes*, Artech House, Inc., 1986.
78. S. Schiller, U. Heisig and S. Panzer, *Electron beam technology*, Verlag Technik GmbH, Berlin 1995.
79. R. J. Hill edited, *Physical vapor deposition*, The BOC Group, Inc., 1986.
80. R. Levi, "New dispenser type thermionic cathode," *J. Appl. Phys.* **24**, 233 (1953).
81. R. Levi, "Improved impregnated cathode," *J. Appl. Phys.* **26**, 639 (1955).

82. R. Forman, "Auger studies comparing the surface concentration of Barium on Tungsten impregnated and M-cathodes," *Applied Surface Science* **24**, 587-598 (1985).
83. B. C. Lamartine, K. G. Eyink, J. V. Czarnecki, W. V. Lampert and T. W. Haas, "A model of dispenser cathode activity," *Applied Surface Science* **24**, 575-586 (1985).
84. "Program area overview-high energy physics," the Department of Energy of United States, Report, 1999(<http://sttr.er.doe.gov/sbir/cycle18/phase1/sol/hep.htm>).
85. R. H. Fowler and L. W. Nordheim, "Electron emission in intense field," *Proceedings of the Royal Society A* **119**, 173-181 (1928).
86. W. P. Dyke and W. W. Dolan, in *Advances in Electronics and Electron Physics*, Vol. VIII, p89-185, Academic, New York, 1956.
87. V. A. Spindt, "A thin film field-emission cathode," *J. Appl. Phys.*, **39**, 3504-3505 (1968).
88. J. A. Nation, L. Schächter, F. M. Mako, L. K. Len, W. Peter, C. M. Tang, and T. Srinivasan-rao, "Advances in cold cathode physics and technology," *Proceedings of the IEEE*, **87**, 865-889 (1999).
89. S. P. Bugaev and G. A. Mesyats, "Investigation of the pulsed breakdown mechanism at the surface of a dielectric in vacuum-1 uniform field," *Sov. Phys.-Tech. Phys.*, **12**, 1358-1363 (1968).
90. G. A. Mesyats, "Explosive processes on the cathode in a vacuum discharge," *IEEE Trans. Elect. Insul.* **18**, 218-225 (1983).
91. R. K Parker, R. E. Anderson, and C. V. Duncan, "Plasma-induced field emission and the characteristics of high-current relativistic electron flow," *J. Appl. Phys.* **45**, 2463-2479 (1974).
92. D. Hinshelwood, "Explosive emission cathode plasma in intense relativistic electron beam diodes," Naval Research Laboratory, Washington, DC, NRL Memo. Rep. 5492, Jan. 1985.
93. P. J. Turchi and R. E. Peterkin, Jr., "Modeling of impedance collapse in high-voltage diodes," *IEEE Trans. Plasma Science* **26**, 1485-1491 (1998).

94. H. Makishima, H. Imura, M. Takahashi, H. Fukui, and A. Okamoto, "Remarkable improvements of microwave electron tubes through the development of the cathode materials," Tech. Digest of the 10th IVMC, Kyongju, Korea, 1997, pp. 194-199.
95. H. Imura, S. Tsuida, M. Takahashi, A. Okamoto, H. Makishima, and S. Miyano, "Electron gun design for traveling wave tubes (TWT's) using a field emitter array (FEA) cathode," in Tech. Dig. IEDM, *Int. Electron Devices Meeting*, Washington, DC, Dec. 7-10, 1997, pp. 721-724.
96. H. Takemura, Y. Tomihari, N. Furutake, F. Matsuno, M. Yoshiki, N. Takada, A. Okamoto, and S. Miyano, "A novel vertical current limiter fabricated with a deep trench forming technology for high reliable field emitter arrays," in Tech. Dig. IEDM, *Int. Electron Devices Meeting*, Washington, DC, Dec. 7-10, 1997, pp. 709-712.
97. C. Lea, "Field emission from carbon fibres," *J. Phys. D: Appl. Phys. (UK)* **6**, 1105-1114 (1973).
98. F. S. Baber, A. R. Osborn and J. Williams, "The carbon-fibre field emitter," *J. Phys. D: Appl. Phys. (UK)* **7**, 2105-2115 (1974).
99. M. Faubel, W. M. Holber, and J. P. Toennies, "Low background cold cathode ion source for molecular beam detection," *Rev. Sci. Instrum.* **49**, 449-451 (1978).
100. R. Prohaska and A. Fisher, "Field emission cathodes using commercial carbon fibers," *Rev. Sci. Instrum.* **53**, 1092-1093 (1982).
101. R. J. Adler, G. F. Fiuttu, B. E. Simpkins, D. J. Sullivan, and D. E. Voss, "Improved electron emission by use of a cloth fiber cathode," *Rev. Sci. Instrum.* **56**, 766-767 (1985).
102. E. Garate, R. D. Mcwilliams, D. E. Voss, A. L. Lovesee, K. J. Hendricks, T. A. Spencer, M. C. Clark, and A. Fisher, "Novel cathode for field-emission applications," *Rev. Sci. Instrum.* **66**, 2528-2532 (1995).
103. J. Benford, D. Price and W. DeHope, "Lowered plasma velocity with cesium Iodide/carbon fiber cathodes at high electric field," private communication.
104. A. Fisher and E. Garate, "Long pulse electron beams produced from carbon fiber cathodes," private communication. Also, A. Fisher and E. Garate, "Electron beams produced from long pulse, carbon fiber cathodes," Abstracts of the 12th

- International Conference on High-power Particle Beams: Beams'98, Haifa, Israel, June 7-12, 1998.
105. M. Korol, E. Jerby, S. Eckhouse, M. Bensal, A Shahadi, "Carbon fiber electron injector for free-electron maser experiments," Nucl. Instrum. and Meth. A **358**, 54-55 (1995).
 106. A. Shahadi, E. Jerby, L. Lei and R. Drori, "Carbon-fiber emitter in a cyclotron-resonance maser experiment," Nucl. Instrum. and Meth. A **375**, 140-142 (1996).
 107. R. B. Miller, "Repetitive pulse operation of reltron tubes," Proceedings of SPIE **3158**, 2-12 (1997).
 108. W. B. Herrmannsfeldt, "Egun-an electron optics and gun design program," SLAC-331, UC-28 (A), Prepared for the Department of Energy under contract number DE-AC03ST00515, Oct.1988.
 109. G. A. Nagy and M. Szilgyi, *Introduction to the theory of space-charge optic*, Halsted Press, John Wiley, New York, 1974.
 110. V. Grinberg, E. Jerby, and A. Shahadi, "Low-cost electron-gun pulser for table-top maser experiments," Nucl. Instrum. and Meth. A **358**, 327-330 (1995).
 111. V. Dichtiar and E. Jerby, "Scattering parameter analysis of finite passive periodic structures," (unpublished).
 112. H. Guo, Y. Carmel, W. R. Lou, L. Chen, J. Rodgers, D. K. Abe, A. Bromaborsky, W. Destler, and V. L. Granatstein, "A novel highly accurate synthetic technique for determination of the dispersive characteristics in periodic slow wave circuits," IEEE Trans. **MTT-40**, 2086-2093 (1992).
 113. M. A. Heald and C. B. Wharton, *Plasma diagnostics with microwaves*, Robert E. Krieger Publishing Company, Huntington, New York, 1978.
 114. A. Kesar, "Multi-beam project: solenoid design," High Power Microwave Lab., Tel Aviv University, Report, July 1997.
 115. MCNC, <http://www.mcnc.org>.
 116. "Model 615 MR Pulserad: Operation & maintenance Manual," Physics International Company.